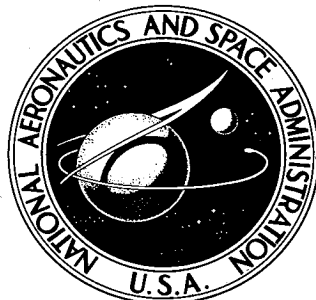


NASA CONTRACTOR  
REPORT



N73-22085  
NASA CR-2232

CASE COPY FILE

NASA CR-2232

THEORETICAL AND EXPERIMENTAL  
STUDIES OF REENTRY PLASMAS

by Michael G. Dunn and Sang-Wook Kang

Prepared by

CORNELL AERONAUTICAL LABORATORY, INC.

Buffalo, N.Y. 14221

for Langley Research Center

NATIONAL AERONAUTICS AND SPACE ADMINISTRATION • WASHINGTON, D. C. • APRIL 1973

1. Report No. NASA CR-2232	2. Government Accession No.	3. Recipient's Catalog No.	
4. Title and Subtitle  THEORETICAL AND EXPERIMENTAL STUDIES OF REENTRY PLASMAS		5. Report Date April 1973	
		6. Performing Organization Code	
7. Author(s) M. G. Dunn and Sang-Wook Kang		8. Performing Organization Report No. CAL No. AF-3093-A-2	
9. Performing Organization Name and Address Cornell Aeronautical Laboratory, Inc. 4455 Genesee Street Buffalo, New York 14221		10. Work Unit No. 502-33-83-01	
12. Sponsoring Agency Name and Address National Aeronautics and Space Administration Washington, D.C. 20546		11. Contract or Grant No. NAS 1-10674	
		13. Type of Report and Period Covered Contractor Report	
		14. Sponsoring Agency Code	
15. Supplementary Notes			
16. Abstract A viscous shock-layer analysis was developed and used to calculate nonequilibrium-flow species distributions in the plasma layer of the RAM vehicle. The theoretical electron-density results obtained are in good agreement with those measured in flight.  A circular-aperture flush-mounted antenna was used to obtain a comparison between theoretical and experimental antenna admittance in the presence of ionized boundary layers of low collision frequency. The electron-temperature and electron-density distributions in the boundary layer were independently measured. The antenna admittance was measured using a four-probe microwave reflectometer and these measured values were found to be in good agreement with those predicted. Measurements were also performed with another type of circular-aperture antenna and good agreement was obtained between the calculations and the experimental results.  Voltage-swept thin-wire electrostatic probes were used to obtain electron-density from the ion-and electron-current portions of probe characteristics while the electron temperature was determined from the electron-retarding region. The electron density determined from these two portions of the probe characteristic were in good agreement with each other and with independent microwave measurements.  A theoretical analysis has been completed which permits calculation of the nonequilibrium, viscous shock-layer flow field for a sphere-cone body. Results are presented for two different bodies at several different altitudes illustrating the influences of bluntness and chemical non-equilibrium on several gasdynamic parameters of interest. Plane-wave transmission coefficients were calculated for an approximate space-shuttle body using a typical trajectory.			
17. Key Words (Suggested by Author(s)) Reentry Plasmas Electrostatic Probe Measurements Viscous Shock-Layer Calculations		18. Distribution Statement	
19. Security Classif. (of this report) Unclassified	20. Security Classif. (of this page) Unclassified	21. No. of Pages 113	22. Price* \$3.00



## TABLE OF CONTENTS

<u>Section</u>		<u>Page</u>
	SUMMARY	1
1.	INTRODUCTION	3
2.	THEORETICAL AND MEASURED ELECTRON-DENSITY DISTRIBUTIONS FOR THE RAM VEHICLE AT HIGH ALTITUDES	3
	2.1    Introduction	3
	2.2    Theoretical Analysis	4
	2.3    Chemical Model Used in Analysis	9
	2.4    Description of Experiment and Diagnostics	10
	2.5    Comparison of Theoretical and Measured Electron Densities	11
	2.6    Conclusions	15
3.	ANTENNA IMPEDANCE DETERMINATION OF ELECTRON DENSITY	16
	3.1    Introduction	16
	3.2    The Input-Admittance Method of Plasma Diagnostics	16
	3.3    Experimental Apparatus and Technique	18
	3.4    Electron-Density and Electron-Temperature Measurements	20
	3.5    Admittance Measurements	21
	3.6    Conclusions	23
4.	USE OF POSITIVELY BIASED ELECTROSTATIC PROBES TO OBTAIN ELECTRON DENSITY IN COLLISIONLESS FLOWS	24
	4.1    Introduction	24
	4.2    Experimental Apparatus and Technique	25
	4.3    Discussion of Results	25
	4.4    Conclusions	28
5.	HYPersonic, VISCOUS SHOCK LAYER WITH CHEMICAL NONEQUILIBRIUM FOR SPHERICALLY BLUNTED CONES	29
	5.1    Introduction	29
	5.2    Analysis	29
	5.3    Results and Discussion	31
	5.4    Estimated Plane-Wave Transmission Coefficients for an Approximate Space-Shuttle Flow Field	32
	5.5    Conclusions	34

6.	POST-RETRACTION ELECTROSTATIC-PROBE RESULTS	35
7.	THREE-DIMENSIONAL, VISCOUS SHOCK LAYER FOR SPACE SHUTTLE-TYPE BODY	37
	APPENDIX A	42
	REFERENCES	44
	TABLES	
	FIGURES	

# THEORETICAL AND EXPERIMENTAL STUDIES OF REENTRY PLASMAS

By Michael G. Dunn and Sang-Wook Kang  
Cornell Aeronautical Laboratory, Inc.

## SUMMARY

A viscous shock-layer analysis has been developed and applied to the calculation of nonequilibrium-flow species distributions in the plasma layer of the RAM vehicle at high altitudes. The theoretical electron-density results obtained are in good agreement with those measured in flight. The flight measurements were obtained using electrostatic probes that protruded well into the shock layer. In addition, the theoretically obtained heavy-particle translational temperatures appear to agree fairly well with the electron temperatures that were measured in the flight experiments using voltage-swept thin-wire electrostatic probes. The influence of the reaction rate coefficients on the calculated electron densities has been assessed and shown to be within the uncertainty in the flight data. The theoretical results demonstrate the importance of including in the chemical model the positive ions  $N_2^+$ ,  $O_2^+$ ,  $N^+$ , and  $O^+$ , in addition to  $NO^+$ , for the high altitudes and velocities considered here.

A circular-aperture flush-mounted antenna, for which a theoretical description of the antenna-plasma interaction has been developed, was used to obtain a comparison between theoretical and experimental antenna admittance in the presence of ionized boundary layers of low collision frequency. The antenna was located in a flat-plate model which was in turn located in the expanding-flow environment of a reflected-shock tunnel. The electron-temperature and electron-density distributions in the plate boundary layer at the antenna location were independently measured using voltage-swept thin-wire Langmuir probes for one of the test conditions. The antenna admittance was measured using a four-probe microwave reflectometer and these measured values were found to be in good agreement with those predicted from the theory. The response of this antenna was found to be very sensitive to changes in the profile and magnitude of electron density for  $0.1 < n_e/n_{e,cr} < 1.2$ . Beyond  $n_e/n_{e,cr}$  of 1.2 the phase rotation continued to provide a measurement of electron density. Measurements were also performed with another type of circular-aperture antenna which did not satisfy all of the constraints of the theoretical model, yet good agreement was obtained between the calculations and the experimental results.

Voltage-swept thin-wire electrostatic probes have been used to obtain the electron density in the free-stream flow of a reflected-shock tunnel and in the boundary layer over a flat plate located in this expanding-flow environment. The voltage sweep was sufficient to permit electron-density determination from both the ion- and electron-current portions of the probe characteristic while the electron temperature was determined from the electron-retarding region. The electron density determined from these two portions of the probe characteristic were in good agreement with each other and with independent microwave measurements for the free-stream experiments. Laframboise's free-molecular flow theory was used to deduce the number-density results presented here.

A theoretical analysis has been completed which permits the calculation of the nonequilibrium, viscous shock-layer flow field for a sphere-cone body

at high altitudes. Results are presented for two different bodies at several different altitudes illustrating the influences of bluntness and chemical non-equilibrium on several gasdynamic parameters of interest. Plane-wave transmission coefficients were calculated for an approximate space-shuttle body using a typical trajectory. These approximate results suggest that for frequencies less than 2200 MHz, transmission difficulties will probably be encountered between 200 and 300 kft on the basis of pure air ionization only. The additional influence of ablation product ionization was not assessed.

Some of the thin-wire electrostatic probe data obtained after the probes were retracted into the base region were analyzed and electron temperatures and electron densities were deduced over an altitude range of approximately 190,000 to 180,000 feet. The results appear to be reasonable on the basis of electron densities and heavy-particle translational temperatures computed at the vehicle shoulder just prior to base-region expansion.

## 1. INTRODUCTION

This document is the final report for Contract NAS 1-10674 which was initiated in April 1971. The work requirement of this contract consisted of five distinct problem areas each of which is sufficiently self contained that the results obtained can be reported separately.

In the remainder of this report, the comparison between the theoretical and measured electron-density distributions for the RAM vehicle at high altitudes will be presented in Section 2. In Section 3, the experimental and theoretical studies performed using the RAM S-band antennas to determine electron density are described. The results of an experimental program using positively biased electrostatic probes to obtain electron density in collisionless flows are discussed in Section 4. A theoretical analysis which permits the calculation of the nonequilibrium, viscous shock-layer flow field for a sphere-cone body at high altitudes is presented in Section 5. This discussion includes calculated plane-wave transmission coefficients for an approximate space-shuttle body for frequencies from 10,000 to 100 mhz. In Section 6 the results of the post-retraction electrostatic-probe results are presented. The report concludes with Section 7 in which our suggestions for obtaining a description of the high altitude, three-dimensional space-shuttle flow field using the relatively simple integral method are presented. It was not within the scope of this contract to complete this particular study. The purpose was only to formulate the problem which was completed.

## 2. THEORETICAL AND MEASURED ELECTRON-DENSITY DISTRIBUTIONS FOR THE RAM VEHICLE AT HIGH ALTITUDES

### 2.1 Introduction

For hypersonic flight vehicles at high altitudes, the flow field surrounding the body, i.e., the shock layer, is fully viscous, with the result that the conventional separation of the inviscid layer and the thin boundary layer is not warranted. For example, for a vehicle with a 12-inch nose diameter, the thin boundary-layer assumption breaks down at altitudes above 200,000 feet and a separate analysis is needed which accounts for the thickened shock-transition zone and the fully viscous fluid within the shock layer along with the effects of chemical nonequilibrium. Analyses are available for the nose region of a blunt vehicle (Refs. 1-4). It is the purpose of this paper 1) to analyze theoretically the chemical nonequilibrium, ionized flow field surrounding a blunt-nosed entry vehicle at high altitudes, and 2) to compare the theoretical results with available in-flight measurements of electron-density distributions in the plasma layer.

The present analysis represents an extension of the basic treatment developed in Ref. 2 to the case of a body composed of a spherical nose region and a conical afterbody section for which the radius of curvature is infinite. For quantitative results, the extended theory has been applied to a NASA-developed RAM-C vehicle (hemisphere - 9° cone) for which large amounts of actual flight data are readily available (Refs. 5-12). For low altitudes, these measurements compared well with the theory developed (Refs. 13, 14) from a boundary-layer point of view. At high altitudes, the viscous-layer theory developed in the present paper will be shown to compare favorably with the flight data in terms of the electron-density profiles across the viscous shock layer at the base of the sphere-cone vehicle.

The flight data reported here were obtained as part of the Langley Research Center's Project RAM (Radio Attenuation Measurements) which has for several years conducted in-flight measurements in order to improve understanding of the causes and methods of predicting (Refs. 13-14) or preventing (Refs. 5-6) the radio-signal degradation during earth entry of a space vehicle. Electrostatic probes projecting from the spacecraft into the plasma layer have been flown in an attempt to measure in-flight electron-density distributions (Refs. 7, 11). On-board diagnostic antennas (Ref. 8), reflectometers (Ref. 9), and VHF antennas (Ref. 10) have also been used to obtain information about the surrounding plasma.

The theoretical analysis will be discussed in Section 2 and followed in Section 3 by a discussion of the chemical model and associated reaction rate coefficients. The experiment and diagnostic techniques are discussed briefly in Section 4. In Section 5, the theoretical results are compared with the flight data and the influences of uncertainties in the chemical model and reaction rate coefficients are assessed.

## 2.2 Theoretical Analysis

In order to present the analysis in a self-contained and coherent manner, the major aspects involved in the development of the theoretical analysis will be included here. More complete details may be found in Ref. 2.

The assumptions made in the theoretical analysis are 1) a thin shock layer, 2) two-layer model of Cheng (Ref. 15), 3) constant Prandtl and Schmidt numbers, 4) binary diffusion due to concentration gradient only, 5) negligible changes in the flow properties due to the chemical reactions in the flow field, 6) ambipolar diffusion for the electrons and ions. These assumptions have been made wholly or in part in the previous analyses and the justification for these assumptions can be found in Refs. 15-19.

### A. Basic Equations

Based on the above assumptions the governing equations for the viscous, ionized shock layer in the merged-layer regime become (Refs. 2, 15)

$$\frac{\partial}{\partial x} (\rho u r^t) + \frac{\partial}{\partial y} (\rho v r^t) = 0 \quad (1)$$

$$\rho u \frac{\partial u}{\partial x} + \rho v \frac{\partial u}{\partial y} = - \frac{\partial}{\partial y} (\mu \frac{\partial u}{\partial y}) \quad (2)$$

$$\rho \frac{u^2}{R_c} = \frac{\partial p}{\partial y} \quad (3)$$

$$\begin{aligned} \rho u \frac{\partial H}{\partial x} + \rho v \frac{\partial H}{\partial y} &= \frac{\partial}{\partial y} \left\{ \frac{\mu}{P_r} \frac{\partial}{\partial y} \left[ H + (P_r - 1) \frac{u^2}{2} \right] \right\} \\ &+ \frac{\partial}{\partial y} \left\{ \frac{\mu}{P_r} (L_{e_i} - 1) \sum_i k_i \frac{\partial C_i}{\partial y} \right\} \end{aligned} \quad (4)$$

$$\rho u \frac{\partial C_i}{\partial x} + \rho v \frac{\partial C_i}{\partial y} = \dot{w}_i + \frac{\partial}{\partial y} (\rho D_i \frac{\partial C_i}{\partial y}) \quad (5)$$

$$p = \rho R T \sum_i (C_i / m_i) \quad (6)$$

These equations express the conservation of mass, momentum, energy, and chemical species, respectively, along with an equation of state. (See Fig. 1 for a description of the flow field.) The eleven chemical species considered are:  $O_2$ ,  $N_2$ ,  $O$ ,  $N$ ,  $NO$ ,  $NO^+$ ,  $O^+$ ,  $N^+$ ,  $O_2^+$ ,  $N_2^+$ , and  $e^-$ . With the two-layer model of Cheng (Ref. 15), these equations are applied to the viscous shock layer allowing for the diffusion of the species into the shock-transition zone by using the modified Rankine-Hugoniot conditions. Analysis of the entire flow field performed in Ref. 17 reinforces the applicability of the two-layer model, and only the viscous shock layer will be considered here.

The boundary conditions for a fully catalytic solid wall are (Refs. 2, 15): at  $y = 0$ ;  $u = 0 = v$ ,  $H = H_b(x)$ ,  $p = p_b(x)$

$$C_i = C_i(\infty) \quad (O_2, N_2) \quad (7)$$

$$C_i = 0 \quad (\text{all other species})$$

at  $y = \Delta(x)$  ;

$$u = U_\infty \cos \beta - (\mu / \rho_\infty U_\infty \sin \beta) \frac{\partial u}{\partial y},$$

$$p \cong \rho_\infty U_\infty^2 \sin^2 \beta,$$

$$H = H_\infty - (\mu / P_r \rho_\infty U_\infty \sin \beta) \frac{\partial}{\partial y} [H + (P_r - 1) u^2 / 2], \quad (8)$$

$$C_i = -(\mu / S_{ci} \rho_\infty U_\infty \sin \beta) \frac{\partial C_i}{\partial y}.$$

The molecular concentrations are expressed in terms of the other species by locally conserving the elemental composition. In the case of pure air of present interest, this yields

$$\begin{aligned} C_{O_2}(y) &= C_{O_2}(\infty) - C_O(y) - \frac{m_o}{m_{NO}} C_{NO}(y) - \frac{m_o}{m_{NO^+}} C_{NO^+}(y) - C_{O^+}(y) - C_{O_2^+}(y), \\ C_{N_2}(y) &= C_{N_2}(\infty) - C_N(y) - \frac{m_N}{m_{NO}} C_{NO}(y) - \frac{m_N}{m_{NO^+}} C_{NO^+}(y) - C_{N^+}(y) - C_{N_2^+}(y), \end{aligned} \quad (9)$$

where  $C_{N_2}(\infty)$  is taken to be 0.767 and  $C_{O_2}(\infty) = 0.233$ .

## B. Chemical-Reaction Model

The chemical reactions used simultaneously for dissociation and ionization are given and discussed in detail along with a table in Section 3. It may be mentioned here that eleven reactions are used involving only neutral species and fifteen reactions for charged species.

## C. Method of Analysis

In analyzing the Eqs. (1-6) with the boundary conditions and the chemical reactions, the physical coordinates are transformed as follows :

$$\xi \equiv \frac{x}{R_N}; F \equiv \frac{1}{G} \int_0^y \frac{\rho}{\rho_\infty} \frac{dy}{R_N}; G \equiv \int_0^{\Delta(x)} \frac{\rho}{\rho_\infty} \frac{dy}{R_N} \quad (10)$$

In addition, a stream function  $\psi$  is introduced such that  $\partial \psi / \partial x = -(1+j)(\pi r)^{1/2} Q v$ , and  $\partial \psi / \partial y = (1+j)(\pi r)^{1/2} \rho u$ , which satisfies the continuity equation (1).

A dimensionless stream function  $f(\xi, F)$  is now obtained by putting

$\psi = (1+j) \rho_\infty U_\infty r (\pi r)^{1/2} f$ , which yields the relationship  $\partial f / \partial F = U G \cos \beta / z$ , where  $U \equiv u / (U_\infty \cos \beta)$ .

Transformation of Eqs. (2-5) yields, after some rearrangement:

### Streamwise Momentum

$$K^2 G \left[ G \frac{\partial f}{\partial F} \frac{\partial}{\partial \xi} \left( \frac{z}{G} \frac{\partial f}{\partial F} \right) - (1 + j) \frac{dz}{d\xi} f \frac{\partial^2 f}{\partial F^2} - z \frac{\partial f}{\partial \xi} \frac{\partial^2 f}{\partial F^2} \right] = \frac{\partial^3 f}{\partial F^3} \quad (11)$$

### Normal Momentum

$$\frac{\partial p}{\partial F} = \frac{\rho_\infty U_\infty^2 z^2 R_N}{G R_c} \left( \frac{\partial f}{\partial F} \right)^2 \quad (12)$$

### Energy

$$\begin{aligned} & z \left( \frac{\partial f}{\partial F} \frac{\partial \theta}{\partial \xi} - \frac{\partial f}{\partial \xi} \frac{\partial \theta}{\partial F} \right) + \frac{z}{1-t_b} \frac{dt_b}{d\xi} \frac{\partial f}{\partial F} (1-\theta) - (1+j) \frac{dz}{d\xi} f \frac{\partial \theta}{\partial F} \\ &= \frac{1}{P_r K^2 G} \frac{\partial^2 \theta}{\partial F^2} + \frac{P_r - 1}{P_r} \frac{2z^2}{(1-t_b) K^2 G^3} \frac{\partial}{\partial F} \left( \frac{\partial f}{\partial F} \frac{\partial^2 f}{\partial F^2} \right) \end{aligned} \quad (13)$$

### Species

$$z \left( \frac{\partial f}{\partial F} \frac{\partial C_i}{\partial \xi} - \frac{\partial f}{\partial \xi} \frac{\partial C_i}{\partial F} \right) - (1+j) \frac{dz}{d\xi} f \frac{\partial C_i}{\partial F} = \frac{1}{S_{C_i} K^2 G} \frac{\partial^2 C_i}{\partial F^2} + \frac{G R_N}{U_\infty} \frac{\dot{\omega}_i}{\rho}, \quad (14)$$

where  $S_{C_i} = \mu / (\rho D_i)$ ,  $t_b = H_b / H_\infty$ ,  $\theta = (H - H_b) / (H_\infty - H_b)$ ,

and  $K^2$  is the rarefaction parameter due to Cheng (Ref. 15). The term  $G$  is a measure of the thickness of the viscous shock layer in the transformed plane.

The Eqs. (11) - (14) should be considered simultaneously with appropriate boundary conditions. However, the previous results obtained, especially those by Chung, Holt and Liu, for the stagnation merged layer, indicate that the flow-field properties such as the pressure, normal velocity and enthalpy change very little despite the presence of chemical reactions in the flow. In the present study, the fluid dynamics equations, Eqs. (11) - (13), are decoupled from the species conservation equations, Eq. (14), in an effort to simplify the analysis. Thus the flow properties such as the streamwise velocity, the pressure and the total enthalpy will be first obtained from Eqs. (11) - (13), so that they may be used as inputs to the species conservation equations. The static temperature, on the other hand, is sensitive to the chemical reactions present in the viscous shock layer, and must be considered along with the species conservation equations.

Hence, the problem now is to solve simultaneously the species-conservation Eq. (14) for O, N, NO,  $\text{NO}^+$ ,  $\text{O}^+$ ,  $\text{N}^+$ ,  $\text{O}_2$  and  $\text{N}_2$ . The electron-number density level may be obtained from the relationship  $n_e = \sum_k n_k$  ( $k$  = ionized species), which gives in particles per c.c.:

$$\sigma_e = N_0 \rho \frac{C_e}{m_e} \quad (15)$$

where  $N_0$  is Avogadro's number.

In order to obtain solutions to the present problem, the Karman-Pohlhausen integral-method approach has been used because of the relative ease of application without unduly sacrificing the accuracy of the results (Refs. 2, 15, 17-20). In addition, the method has been shown to be applicable to the case of nonequilibrium flow (Ref. 21), and to the case of merged-layer flow (Refs. 2, 20). Thus, integrating the species conservation Eqs. (14) from  $F = 0$  to  $F = 1$ , we obtain after a series of rearrangements,

$$\frac{d\Omega_i}{d\xi} = \pm \left( \frac{GR_N}{U_\infty} \int_0^1 \frac{\dot{w}_i}{\rho} dF - \frac{E_i}{Sc_i K^2 G} \right) \quad (16)$$

where  $\Omega_i \equiv \pm \cos \beta G \int U C_i dF$ , and  $E_i \equiv (\partial C_i / \partial F)_b$ , and  $i = \text{O}, \text{N}, \text{NO}, \text{NO}^+, \text{O}^+, \text{N}^+, \text{O}_2$  and  $\text{N}_2$ .

The various species profiles  $C_i$  and the static temperature profile to be used in the above equations are, for a solid wall (see Ref. 2 for details of derivation):

$$C_i = E_i (F - N_i F^3) \quad (17)$$

and

$$\lambda = \lambda_b + \alpha_1 F + \alpha_2 F^2 + \alpha_3 F^3, \quad (18)$$

where

$$N_i = (1 + Q_i)/(3 + Q_i), \quad Q_i \equiv Sc_i K^2 G \sin \beta, \quad \lambda \equiv T/T_\infty, \quad \lambda_b = T_b/T_\infty,$$

$$\alpha_1 = (1 - \lambda_b + U_\infty^2 / 2 C_{p\infty} T_\infty) B - (\mathcal{R}/C_{p\infty} T_\infty) \sum_i \tau_{d_i}^* E_i / m_i,$$

$$\alpha_2 = - U_\infty^2 A^2 \cos^2 \beta / (2 C_{p\infty} T_\infty)$$

and

$$\alpha_3 = 1 - \lambda_b + (\sin^2 \beta) U_\infty^2 m_\infty (\gamma - 1) / [(\gamma + 1) \mathcal{R} T_\infty] - \alpha_1 - \alpha_2$$

By substitution of the Eqs. (17) and (18) in the definition of  $\Omega_i$  along with the other flow properties obtained from Eqs. (11) - (13), we obtain expressions for these quantities in terms of the unknown parameters  $E_i$ . Other terms such as  $K^2$ ,  $t_b$ ,  $G$ , etc., are specified as known input quantities. Since the species production term  $\dot{\omega}_i$  contains not only the temperature term but other species terms as well, it is necessary to solve Eqs. (16) simultaneously. Thus the problem is to determine from Eqs. (16) the unknown parameters  $E_i$  as functions of the streamwise distance  $\xi$ . The term  $E_i$  denotes the local concentration-gradient parameter in the transformed coordinate system. Solutions were obtained by integrating Eqs. (16) on a digital computer along the body from the stagnation region through the sphere-cone junction to the afterbody conical section by using the Adams-Molton predictor-corrector method. In order to simplify the analysis while accounting for the change in shock shapes along the body, the distribution of the shock angle was initially assumed and updated from the results. Based on the cases considered in the present analysis, two iterations were usually sufficient to obtain correct shock shape along the body. The solutions are obtained in terms of the flow variables such as the velocity and temperature, and in terms of the chemical species distributions in the shock layer and along the body surface.

In order to test the validity of the theory, the present analysis was applied to a RAM-C vehicle ( $9^\circ$  sphere-cone) because of the availability of the actual flight data on the vehicle, especially in terms of the electron-concentration distributions at high altitudes where the flow is in the viscous shock-layer regime. Solutions are obtained at several altitudes for comparison between theory and experiment. This will be discussed more fully in Section 5.

### 2.3 Chemical Model Used in Analysis

The initial chemical model used in this study was composed of 12 species and 64 chemical reactions. Subsequent calculations performed for the altitude and velocity regime of interest here made it possible to eliminate many of the unimportant reactions from the model. The reaction rate coefficients were perturbed by factors felt to be consistent with their uncertainty (10 to 100 for many of the ion-atom and ion-molecule reactions) prior to elimination of a particular reaction. The final chemical model used in the analysis is given in Table 1. The model included the neutral species  $N_2$ ,  $N$ ,  $O_2$ ,  $O$ , and  $NO$  and the charged species  $N_2^+$ ,  $N^+$ ,  $O_2^+$ ,  $O^+$ ,  $NO^+$ , and  $e^-$ . For the high altitude conditions of interest here (above 230,000 ft), calculations performed at NASA indicated that ablation-product ionization should not be a problem.

The reaction rate coefficients for the reactions involving only neutral species (reactions 1-6 and 22-26) were taken from Refs. 22 - 28. The rate coefficients for the deionization of  $NO^+$ ,  $O^+$ ,  $N^+$ ,  $O_2^+$  and  $N_2^+$  (reactions 7-10 and 13) were taken from the experimental results reported in Refs. 29 - 32.

Reaction rate coefficients for the charge-transfer and ion-molecule reactions (reactions 11, 12, 16-20) are not nearly as well known as those for the reactions discussed above. This lack of information is unfortunate because these reactions do play an important part in the nonequilibrium process and can have a significant influence on the relative species distributions. However, for the calculations reported here, the only reactions of this class that were important were reactions 11, 12, and 19. Of these, the rate coefficients for reactions 11 and 12 were used in the data correlation of Refs. 31 and 32 and are felt to be reasonably well known. Perturbation of the rate coefficient of reaction 19 by a factor of 10 will change the relative concentrations of  $O_2^+$  and  $NO^+$  somewhat but it will not influence the electron density significantly because of the fast two-body dissociative recombination of both  $NO^+$  and  $O_2^+$ . Therefore, even though there is a relatively large uncertainty associated with the reaction rate coefficient for the ion-atom and ion-molecule reactions, the electron-density levels and distributions for the particular case reported here are not significantly affected.

Reaction rate coefficients for reactions 14, 15 and 21 were taken from Ref. 34. These rates are not well known but, fortunately, these reactions do not have a significant influence on the results so that their uncertainty is unimportant compared with that of several other reactions in the model.

In these calculations, the vibrational and electronic degrees of freedom are assumed to remain in thermal equilibrium with translation while the chemical reactions proceed at finite rates. The free-electron temperature was assumed to be equal to the heavy-particle translational temperature. On the basis of the in-flight measured electron temperatures presented in Section 5 of this paper, this assumption appears to be a reasonable one for the calculations reported here.

#### 2.4 Description of Experiment and Diagnostics

The RAM C series of flights was designed to obtain data in the velocity regime of about 25,000 ft/sec where the importance of atomic particle ionization cannot be neglected. For the purposes of this paper, we are concerned with the second (RAM C-II) and final (RAM C-III) flights in this series. During this final flight, water and electrophilic liquid were periodically injected into the plasma layer to reduce the free-electron density level; however, only data obtained in the absence of injection are presented. Many different diagnostic techniques were used on these vehicles, but we will place major emphasis on the electrostatic probe results here because this is the only diagnostic providing a direct measurement of electron-density profiles in the plasma.

The reentry flight-path angle for these payloads was  $-15^\circ$  and both of them were spin stabilized at 3 rpm. The payload geometries were nearly identical and consisted of a 6-inch radius hemispherical nose followed by a  $9^\circ$  half-angle cone. The RAM C-II nose was covered by a beryllium-cap

heat sink during the portion of the entry trajectory of interest here. The RAM C-III had a nose covering of phenolic-graphite charring ablator for heat protection. For both payloads, the conical section was covered with a teflon heat shield (Ref. 7).

Figure 2 is a photograph of the RAM C-II payload showing the location of the electrostatic probe rake and a thermocouple rake. Eight wire probes were located on the leading edge of the rake so that the last probe extended to a maximum distance of approximately 7 cm. into the plasma layer as illustrated on Fig. 3. The collectors were placed so that their longitudinal axis was at 45° to the flow direction and they were biased at a constant negative voltage so as to collect ions. Detailed descriptions of the probe and rake construction, beyond that given in Fig. 3, and the data reduction procedure are given in References 7, 11 and 12 and therefore will not be repeated here.

Figure 4 is a photograph of the RAM C-III payload illustrating the relative location of two rakes of electrostatic probes for this flight. The rake of constant bias-voltage probes was modified (Refs. 2, 12) in that the number of collectors was increased to 16 and the distance that the final probe extended into the plasma layer was increased from 7 to 14 cm. Other modifications of wedge and sweep angle were also made and are discussed in Refs. 7, 12. The thermocouple rake was modified (Refs. 7, 12) to include four voltage-swept thin-wire probes located so that their longitudinal axis was approximately aligned with the flow direction. The outer wires extended to a maximum distance of 9.5 cm. from the body into the plasma layer. The voltage sweep range, sweep cycle, and data collection procedure are all discussed in detail in Ref. 12. The relative locations of the probes and sketches of the rake construction are given in Fig. 5 and 6 for the constant bias-voltage and swept-voltage probes, respectively.

## 2.5 Comparison of Theoretical and Measured Electron Densities

The electrostatic probes discussed in the previous section were used to collect current, from which the electron density could be calculated, from an altitude of approximately 290,000 ft. down to 200,000 ft. At this lower altitude, the probes were retracted into the base region but the probes continued to operate and the voltages were recorded. However, for the purposes of this paper, only the electron-density data deduced for the altitude range of 233,000 to 275,000 ft. will be compared with the theoretical results. To test the limitations of the theory, it was applied outside of what is considered the range of validity (due to the neglect of the  $\partial p / \partial x$  term as a higher-order term (Ref. 15) in the present analyses) to calculate profiles for 214,000 ft. altitude. Perhaps fortuitously, the calculated results compare favorably with the flight data at this lower altitude as will be shown at the end of this section.

For the altitude range of interest here, the calculated mean free paths were such that the probes were operating in a free-molecular flow environment. It was therefore possible to reduce the voltage-swept thin-wire probe data using the theory of Laframboise (Ref. 36) and the constant bias-voltage probe data using the theory of Smetana (Ref. 37). The accuracy of Laframboise's theoretical results is well known. References 38-40 have demonstrated similarly good results using Smetana's theory. It can be shown that the number densities obtained using the results of Ref. 37 are insensitive to the magnitude of the electron temperature which is important from the viewpoint of flight-data analysis. This observation is not generally true when obtaining electron densities from probes aligned with the flow.

Figure 7 illustrates the comparison of the calculated electron densities to those measured, on the C-II and C-III flight experiments, using the electrostatic probes previously described. Comparisons are made for altitudes of 233,000 ft., 250,000 ft., 265,000 ft., and 275,000 ft. At all of these altitudes, the vehicle velocity was approximately constant at a value of approximately 25,100 ft./sec. The trajectories flown by these vehicles and their payload configurations were sufficiently similar that it was not necessary to perform separate calculations for the individual flights. Therefore, both the constant bias-voltage probe data of C-II and C-III and the swept-voltage probe data of C-III are included for comparison purposes. The uncertainty in the flight data obtained with the constant-voltage probes is indicated by the crosshatching and the vertical bars. The data reported are the time-averaged electron densities averaged over one body revolution and the indicated uncertainty represents the peak-to-peak fluctuations mainly due to angle of attack. A similar uncertainty existed in the swept-voltage probe data, but is not illustrated in order to prevent confusion.

The results of the nonequilibrium flow, viscous shock-layer calculations are indicated on Fig. 7 by the solid lines. The shock-layer thickness is also illustrated and shown to decrease with altitude up to approximately 265,000 ft. above which it doesn't appear to change much. The agreement between the calculated electron densities and the flight data is reasonably good over that portion of the shock layer for which data were obtained. The theoretical results show that the electron number-density levels increase near the outer edge of the viscous shock layer. Physically, this seems to be due to the diffusion of the chemical species into the shock-transition zone, giving a finite, non-zero level at the shock-layer edge. In addition, low temperatures exist near the shock-layer outer edge as a result of small shock angle at the base of the vehicle. This means a high level of mass density there, and, coupled with the finite electron species level, the electron number density is thus seen to increase near the outer-edge of the viscous shock layer. However, calculations were performed (Ref. 41) for a much longer cone (see Section 5 of this report) of the same nose radius and half-angle. The results show that the peak electron-density levels are located in the plasma layer away from the shock edge, partly due to the thinner, weaker shock existing there.

On the C-III flight the voltage-swept probes were used to make measurements of the electron temperature between 1.5 and 9.5 cm. from the body surface. Since the translational temperature was used in the nonequilibrium calculations where, in fact, the electron temperature should have been used for evaluating many of the rate coefficient for reactions involving free electrons, these data are particularly important. The results of the electron temperature measurements are compared with the calculated heavy-particle translational temperature on Fig. 8. On the basis of this comparison, the electron temperature appears to be approximately equal to the translational temperature at the measuring station. With the available flight data, it is difficult to be definitive about the relative magnitudes of the heavy-particle temperature and the electron temperature at other locations in the flow field. However, the flow fields of interest here are highly nonequilibrium and it can be seen from Table 1 that the reaction rate coefficients for the electron reactions are proportional to the -1.5 to -4.5 power of the electron temperature, suggesting that if there were a substantial difference between the inflight translational and electron temperatures, it would be reflected in the measured electron densities. It obviously cannot be stated with certainty that such is not the case. What can be said is that if one assumes these two temperatures to be in equilibrium throughout the flow field, then reasonably good agreement is obtained between data and theory at the measuring station.

The calculations shown on Fig. 7 were obtained using the chemical model given in Table 1. The upper bound of the backward reaction rate coefficients of reactions 7-10 and 13 were used in this calculation. The values used for the reaction rate coefficients for the remaining reactions were those given in the table. Because of uncertainties in rate coefficient values, it is important to assess their influence on the calculated electron densities and the subsequent agreement with flight data. This has been accomplished by repeating the nonequilibrium calculations using the lower bound of the backward reaction rate coefficients of reactions 7-10, and 13 while maintaining those for all other reactions at the Table 1 values. Figure 9 illustrates the results of these calculations for altitudes of 233,000 ft. and 275,000 ft. The influence at intermediate altitudes was similar to that shown. The uncertainty in reaction rate coefficients changes the predicted electron density by a factor of approximately two over the plasma layer. In general, the resulting uncertainty in the calculated number densities is consistent with the uncertainty in the flight data as can be seen from Fig. 9.

It is also important to assess the influence of the chemical model on the calculated electron densities. Calculations were therefore performed for the probe location using one model in which the only positive ion was  $\text{NO}^+$  and a different model in which the positive ions were  $\text{NO}^+$ ,  $\text{N}_2^+$ ,  $\text{O}_2^+$ ,  $\text{N}^+$ , and  $\text{O}^+$ . The results of these calculations are illustrated on Fig. 10 for altitudes of 233,000 ft. and 275,000 ft. The calculated electron densities at 233,000 ft. were found to be essentially uninfluenced by ions other than  $\text{NO}^+$ . However, at 275,000 ft. inclusion of the additional ions in the chemical model drastically influenced the results. It is important to note that the results of the calculation which included only the  $\text{NO}^+$  ion fall well below the flight data in contrast to the more complete model which agrees well with flight data. At the probe location, the difference between the calculated results using these two models decreases monotonically in going from 275,000 ft. to 233,000 ft.

The electrostatic-probe data were reduced assuming that the mass of dominant ion at the probe location was that of  $\text{NO}^+$ . Figures 11 and 12 present calculated nonequilibrium species distributions across the plasma layer at the sphere-cone junction and at the probe location for altitudes of 233,000 ft. and 275,000 ft. For the probe location and at 233,000 ft., the  $\text{NO}^+$  ion is dominant by approximately a factor of ten. However, at the junction the dominant ion was calculated to be  $\text{O}^+$ . The calculations performed for the 275,000 ft. trajectory point indicate that  $\text{NO}^+$  was still dominant at the probe location but only by a factor of approximately two. The dominant ion at the junction was again  $\text{O}^+$  but  $\text{NO}^+$  and  $\text{O}_2^+$  were a close second.

To test the limits of validity of the theory, calculations were performed for a trajectory point at 214,000 ft. At this altitude, conditions are such that theoretically the formulation should not be valid, since the  $\frac{\partial p}{\partial x}$  term was neglected in the present analysis as a higher-order term. However, the results of the calculation are shown in Fig. 13 to be in reasonable agreement with the flight data. It is quite possible that this reasonably good agreement at 214,000 ft. may be fortuitous. However, the result may be of future interest if one is interested in obtaining an engineering approximation for similar vehicle and trajectory conditions.

In addition to the electrostatic probe data discussed above, flush-mounted microwave reflectometers (Ref. 7) were also flown on the RAM vehicles. These particular reflectometers can be used to ascertain the electron-density profile in the plasma layer under limited conditions, but they can generally be used to determine the peak value of the electron density at the antenna location. Figures 14 and 15 present favorable comparisons of the predicted electron-density profiles with the peak value of the electron density as determined from the flight data (Ref. 9) for  $X/R_N$  of 5.2 and 7.65 (stations 3 and 4 of Ref. 7) respectively, for altitudes of 233, 250, 265, and 275 kilofeet. Due to the nature of the reflectometers, plasma electron densities beyond  $y/\Delta$  of 0.8 would not be seen. The agreement between the theoretical results and the flight data is considered to be reasonably good.

Reflectometer measurements were also performed in the nose region at  $X/R_N$  of about 0.9 and just after the hemisphere-cone junction at 2.1. However, the agreement between theoretical prediction and flight data was not nearly as good for these locations as it was for the two downstream stations. In the nose region, the calculated peak number density was about 20 times greater than the reflectometer data and at  $X/R_N$  of 2.1 the calculated peak value was about 10 times greater than the reflectometer data.

At the present time, the reason for the discrepancy between the reflectometer data at  $X/R_N$  of 0.9 and 2.1 and the theoretical prediction is not understood. As possible causes, the translational-vibrational temperature nonequilibrium and the translational-electron temperature nonequilibrium were investigated for an altitude of 265,000 ft. A particular streamline was chosen which enters the viscous shock layer at about 30 degrees from the stagnation line. The results of the calculations of the vibrational relaxation distance for molecular nitrogen indicated that translational-vibrational equilibrium was

achieved in less than 0.8 cm. behind the shock. Molecular oxygen would achieve translational-vibrational equilibrium in significantly less distance. It therefore appears reasonable to assume translational-vibrational equilibrium for the viscous hypersonic flow around a RAM-C vehicle at high altitudes. In addition, comparison of the distribution of the electron temperature along the streamline noted above with the nitrogen vibrational temperature and the heavy-particle translational temperature showed that it is appropriate to assume translational-electron temperature equilibrium in the nose region.

## 2.6 Conclusions

In this paper, a multicomponent, ionized, viscous shock-layer flow about a blunt-nosed vehicle (sphere-cone) at high altitudes has been theoretically analyzed. This was accomplished by transforming the coordinates and the flow variables, and by utilizing the Karman-Pohlhausen integral method to the Navier-Stokes equations and the species-conservation equations under the thin shock-layer assumption.

The theoretical development was applied to a RAM-C sphere-cone vehicle ( $9^\circ$  semi-cone angle) developed by NASA because of the wealth of in-flight measurements. Eleven chemical species ( $O_2$ ,  $N$ ,  $O$ ,  $N$ ,  $NO$ ,  $NO^+$ ,  $O^+$ ,  $N^+$ ,  $O_2^+$ ,  $N_2^+$  and  $e^-$ ) were included in the analysis for eleven reactions involving only the neutral species and fifteen reactions for charged species. Solutions were obtained at various altitudes where the viscous shock-layer flow exists around the vehicle. The theoretical results for the electron-concentration profiles compare favorably with the experimental data obtained using electrostatic probes located at the base of the vehicle. In addition, the heavy-particle translational temperatures obtained from theory seems to agree fairly well with the electron temperatures measured from the voltage swept thin-wire electrostatic probes.

The effect of the reaction-rate coefficients on the quantitative theoretical results was also analyzed and shown to be within the uncertainty range of the flight data. The results also demonstrate the importance of including in the chemical model the positive ions  $N^+$ ,  $O^+$ ,  $O_2^+$ ,  $N_2^+$  in addition to  $NO^+$  for high altitudes and velocities considered here.

### 3. ANTENNA IMPEDANCE DETERMINATION OF ELECTRON DENSITY

#### 3.1 Introduction

Many (Refs. 7, 9, 42-48) different diagnostic techniques have been employed to determine the electron-density level in the plasma layer surrounding an entry vehicle. Several (Refs. 9, 42-48) of these instruments can be located flush with the vehicle skin while others (Ref. 7) protrude into the flow field. It is generally recognized that if one is interested in obtaining information about the electron-density gradient and level in the plasma layer, then the protruding probes are the most desirable. However, for some vehicles and under certain flight conditions, protruding objects are not feasible thus requiring use of flush-mounted diagnostics in order to obtain as much of the desired information as possible.

Bailey and Swift (Ref. 49) have treated theoretically the problem of a circular-aperture antenna excited in the  $TE_{11}$  mode. Swift, et al. (Ref. 46) and Grantham (Ref. 9) have used circular antennas on a re-entry vehicle to obtain in-flight admittance measurements from which they could deduce the plasma properties in the near field.

The accuracy of the calculational technique (Ref. 49) has not been assessed for a flowing plasma and it is therefore the purpose of this study to investigate the agreement between experimental and theoretical antenna admittance for a known distribution of electron density in the plasma layer adjacent to a flat-plate surface located in a flowing plasma. The experimental phase of this work is an extension to the previous work of Taylor (Ref. 50) who utilized the same antenna employed here to perform admittance measurements in a shock-tube flow but under much different gas-dynamic conditions. His boundary layers were significantly thinner than the present ones and the axial length of the uniform plasma was much less. The collision frequency,  $\nu/\omega$  of his plasma (0.1 torr experiments) was less than 0.15 which is of the same order as that obtained here. Taylor illustrates good agreement between his admittance data and the predictions of Croswell, et al. (Ref. 51). However, because his boundary layers were thin, it was not possible to probe them in order to obtain a measured electron-density profile for use in the calculations.

#### 3.2 The Input-Admittance Method of Plasma Diagnostics

The theory of the input admittance of plasma-covered aperture antennas has been studied by a number of investigators over the past several years. These studies were motivated by the desire to extend the diagnostic range of antennas beyond a simple marker of critical electron density. If the antenna consists of a waveguide opening onto a flat ground plane, the normalized input-admittance expression is given by

$$Y_{IN} = \frac{1}{Y_c} \frac{1}{|V_o|^2} \iint_{APERTURE} (\vec{E}_{AP} \times \vec{H}^*)_{z=0} d\vec{s} \quad (1)$$

where  $\gamma_c$  is the characteristic admittance of the waveguide,  $V_o$  is the impressed voltage,  $E_{ap}$  is the electric field at the aperture,  $H^*$  is the magnetic field,  $dS$  is the surface element in the  $z-y$  plane, and  $z = 0$  defines the ground plane. The relationship between input admittance and the complex reflection coefficient  $\Gamma$  is:

$$\Gamma = \frac{1 - \gamma_{in}}{1 + \gamma_{in}} \quad (2)$$

The near-field properties of the circular-wave guide antenna were investigated by Bailey and Swift (Ref. 49), and later generalized to account for stratified layers of inhomogeneous dielectric material (including plasmas). The formulation of the problem resulted in a reduction of Equation (1) to a single integral which was numerically evaluated as a function of collision frequency, electron density, and gradients of electron density.

Prior to the shock-tunnel experiments, the input admittance was calculated as a function of boundary-layer thickness ( $\delta$ ) and free-stream electron density for the antenna shown in Fig. 16. The plasma profiles used for these calculations (given in Fig. 17) were assumed to be parabolic, with parameters adjusted so that the electron density was zero at the wall and the free-stream value at  $\delta$ . The particular values of  $\delta$  selected for the pre-experiment analysis were 0, 0.2, 0.4, 0.6, 1.2, and 2.4 inches. Beyond the point at which  $n_e/n_{e,cr}$  reached 1, the plasma was assumed to be homogeneous to 10 cm which was sufficiently thick so that reflections from the air-plasma interface at 10 cm were negligible.

The theoretical results are shown in Fig. 18 as a function of  $\delta$  and  $n_e/n_{e,cr}$  for  $v/\omega = 0.1$ . These results suggest the following diagnostic applications of the circular-aperture antenna:

1. The measurements of the initial response of the antenna near  $n_e/n_{e,cr} = 1$  can be used to uniquely infer both  $n_e/n_{e,cr}$  and  $\delta$ .

2. When the plasma is overdense, the admittance measurements can be used to infer either  $n_e/n_{e,cr}$  or  $\delta$ . Some "a priori" knowledge of one of the parameters must be given in order to provide a measurement of the other.

The boundary-layer electron-density profile was measured at two locations on the flat-plate model for one of the experimental conditions used in this work. With this information, it was possible to theoretically estimate the magnitude of the boundary-layer thickness for the remaining experimental conditions. By assuming that the peak electron density occurs at the boundary-layer edge, which introduces some error because previous experimental results (Refs. 52, 53) for similar conditions suggest that it occurs at distances slightly less than the boundary-layer thickness, it was possible to obtain reasonable estimates of electron density in the overdense region. It is worth noting that the antennas and the calculations reported in Fig. 18 can be scaled for application at frequencies other than S-band. The antenna for which these calculations and experiments were performed is a reproduction of one flown on a re-entry experiment (Ref. 8) and will henceforth be designated as the RAM C-III S-band antenna.

Another type of circular-aperture antenna was also used in these laboratory experiments and in the RAM flight experiments. This antenna was designed for and used on the RAM C-II flight two years before the boundary-value problem of the circular-waveguide antenna was developed. Although the antenna operated at the same frequency as the one discussed above, there were some major design differences. Referring back to Fig. 16, these differences are:

1. The antenna was extended through the dielectric material so that the aperture was contiguous to the plasma.
2. The diameter of the antenna was designed to be smaller than that of the one shown in Fig. 16 in order to reduce the effects of lateral gradients of electron density over the aperture.
3. Because the waveguide section was near cut-off, tuning screws were inserted to match the antenna to free space. This tuning was accounted for in the theoretical model.

Subsequent to the flight of RAM C-II, the aperture admittance was computed using Equation (1) in connection with the transformation derived in Appendix A. This transformation was used to calculate the admittance in preparation for the tunnel experiments described herein.

### 3.3 Experimental Apparatus and Technique

An engineering drawing of the RAM C-III S-band antenna used in the experiments is shown in Fig. 16. It consists of a circular cavity 4.5 inches deep and 2.65 inches in diameter. A co-ax-to-waveguide transition was inserted 0.4 inches from the back wall of the cavity, i.e., one-quarter of a guide wavelength. The length and diameter of the probe were adjusted to obtain a 1:1 impedance match between the waveguide and RG-141 coaxial cable at the operating frequency of 3.348 GHz. An 0.8 inch teflon plug was inserted into the waveguide flush with the aperture and the ground plane was covered with 0.3 inches of plexiglas. The reasons for selecting these dimensions is discussed elsewhere (Ref. 46).

The antenna described above and a second one mentioned previously were mounted in a sharp flat-plate model which was subsequently placed in the fiberglass nozzle of the shock tunnel (Ref. 52). The C-III antenna was operated at 6.75 inches from the plate leading edge and the C-II antenna was operated at 11.25 inches from the leading edge. The boundary layer over the plate provided an electron-density gradient in the near field of the antenna. This boundary-layer was sufficiently thick so as to permit good resolution of the electron-density profile by detailed probing with thin-wire Langmuir probes.

The flat-plate model was 7-inches wide by 30-inches long. The top surface was constructed of plexiglas with the exception of a 1-inch long stainless-steel leading edge. Boundary-layer surveys were performed at distances

from the leading edge of 6.75 and 11.25 inches. At the most upstream location, the flow was considered to be two-dimensional since spanwise static-pressure measurements obtained by Boyer, et al. (Ref. 53) at 5 and 10 inches from the leading edge, for similar flow conditions, indicated that the flow was uniform across the plate. However, for the 11.25 inch location pressure measurements were not obtained, and it is possible that the flow here may not have been two-dimensional.

During all of the experiments noted above, an independent measurement of the integrated free-stream electron density was obtained at 11 inches and one inch upstream of the flat-plate leading edge using microwave interferometers operating at frequencies of 35 and 17 GHz, respectively.

The probes used in these experiments were constructed by surrounding 0.004 inch diameter tungsten wires with a quartz envelope, leaving a nominal 0.400 inch length of bare wire exposed. Immediately prior to each run, the tungsten oxide was removed by placing the probe in a dilute solution of sodium hydroxide and passing approximately 400  $\mu$ A of current through the circuit for approximately 10 minutes. In performing the probe measurements, care was taken to keep the probe holder far out in the flow to avoid any possible interference effects in the subsonic-flow region. The quartz tubing surrounding the probes was bent as shown in Ref. 52. The 1/16-inch diameter tubing used in the probe construction did not permit probing to distances less than 0.060 inches off the plate surface.

Figure 19 illustrates the two S-band antennas mounted in the flat-plate model. Also shown is an X-band horn antenna, the results of which are not reported here. A schematic diagram of the four-probe reflectometer is given in Fig. 20. The reflected signal was also monitored as indicated on the schematic. This system was convenient for data reduction purposes in that five arcs were always available for Smith chart construction. Waveguide instead of coaxial cable was used wherever possible in the system.

As part of the pre-experiment calibration, the diode spacings were measured using a moveable short. If the microwave diodes are numbered so that #1 is nearest the generator and #4 is nearest the short, then the spacings were  $1-2 = 0.1255 \lambda_g$ ,  $2-3 = 0.1218 \lambda_g$ ,  $3-4 = 0.1278 \lambda_g$ , and  $4-1 = 0.1252$  where  $\lambda_g$  was the guide wavelength of 11.378 cm. The reflectometer system was tuned using a matched load with VSWR of approximately 1.025 to 1.035. Each of the diodes was then calibrated as follows. An attenuation of 3 db was set on the variable attenuator and the four diode outputs were adjusted until they were equal. The attenuation was increased in increments of 1 db until reaching 26 db. The attenuator was then set to  $\infty$  attenuation and the final readings taken. The voltages were normalized so that the diode output at 3 db attenuation represented the diameter of the Smith chart. During the experiments this 3 db tare was always set on the variable attenuator.

The free-space admittance was measured with the antenna inside and outside of the shock tunnel, but no difference was observed between the results. Aluminum foil was then placed over the aperture of the antennas to

obtain the antenna-short reference. In addition, the coaxial cable was shorted at the antenna input terminal to obtain an additional reference.

The antenna admittance and the Langmuir-probe measurements were performed in separate experiments. In both cases, the test gas was carbon monoxide but the level of residual nitrogen present in the test gas was different. The carbon monoxide used in the antenna experiments was supplied by Lif-O-Gen, Inc. A chemical analysis of the gas indicated the following:  $25 \pm 5$  ppm of nitrogen, argon less than 2 ppm, carbon dioxide less than 10 ppm, helium less than 2 ppm, oxygen less than 2 ppm and water less than 1 ppm. Unfortunately, a sufficient quantity of this gas could not be obtained for the boundary-layer measurements and it was necessary to use ultra high-purity grade supplied by Air Products and Chemicals, Inc. The principal impurity in this gas was nitrogen estimated to be on the order of 1500 to 2000 ppm. The presence of this additional nitrogen was important from a chemical kinetics viewpoint and had to be considered. However, even with the nitrogen, the dominant ion in the free-stream flow was calculated to be  $C^+$  consistent with the calculations for the purer gas.

### 3.4 Electron-Density and Electron-Temperature Measurements

The boundary-layer measurements of electron density and electron temperature reported here were performed in carbon monoxide that had expanded from equilibrium reservoir conditions of  $7060^\circ K$  at 17.3 atm. The relative magnitudes of the mean free paths  $\lambda_{i-n}$ ,  $\lambda_{n-n}$ ,  $\lambda_{e-n}$ ,  $\lambda_{i-i}$ , and  $\lambda_{e-e}$  were calculated using the expressions summarized by Sonin (Ref. 54) and presented in Fig. 18. The electron density was obtained from the ion-current portion of the Langmuir-probe current-voltage characteristic using the free-molecular flow theory of Laframboise (Ref. 36). In some cases the electron-current portion of the characteristic could be used to obtain electron density which was found (Ref. 55) to be in good agreement with the value obtained from the ion current. An ion mass of 12 was used in the data reduction consistent with the calculated species concentrations presented in Ref. 30.

Electron-density measurements obtained in the boundary layer at 6.75 inches from the plate leading edge are shown in Fig. 22. The measured boundary-layer values approach the estimated free-stream value at approximately 1.2 inches from the surface. This estimate of the free-stream number density was obtained from microwave-interferometer data taken at the measuring station in the absence of the plate, assuming that the plate does not significantly disturb the flow.

Since the dominant ion in the free-stream flow was  $C^+$  and the electron-temperature measurements shown in Fig. 23 suggest a relatively constant value, it is unlikely that gas-phase recombination of ions and electrons would be important. However, it is difficult to be certain as to whether or not the plexiglas surface would provide a good catalyst for surface recombination of ions and electrons. If the wall were catalytic, then a diffusion controlled

boundary layer would be appropriate and it would have a number-density profile consistent with the measurements. One cannot be certain without detailed calculations which were beyond the scope of this work, but it is likely that the boundary-layer gas phase chemistry was frozen at an upstream value and that surface recombination controlled the boundary-layer electron-density profile.

The boundary-layer electron-density and electron-temperature profiles obtained at 11.25 inches from the leading edge are presented in Figs. 22 and 23. The number-density measurements suggest a slightly thicker boundary layer at this location but the profile shape is similar to that measured at 6.75 inches. The electron temperature was again found to remain rather uniform through the boundary layer and along the plate.

The antenna measurements to be discussed later were performed for several reflected-shock reservoir conditions in order to achieve a range in the magnitude of  $n_e/n_{e,cr}$ , but the boundary-layer measurements were performed for only one experimental condition because of the detailed nature of this experiment. The range of test conditions was such that boundary-layer electron-density profiles in terms of  $n_e/n_{e,\infty}$  vs  $y/\delta$  could be constructed and assumed similar. This profile could then be appropriately adjusted for the different free-stream conditions. To aid in constructing the electron-density profiles for conditions other than the measured one, a simple estimate of the boundary-layer thickness,  $\delta$ , was required. The technique selected was that described by Burke (Ref. 56) and Figs. 22 and 24 show that the results of this method are somewhat less than the value that one might have estimated on the basis of the electron-density measurements. However, for the intended purpose of scaling the profiles, this result is quite satisfactory.

### 3.5 Admittance Measurements

The RAM C-III antenna was installed in the flat plate at 6.75 inches from the leading edge and the top side of the plate was located on the nozzle centerline with the leading edge at 22.5 inches from the nozzle throat. For these experiments, the peak electron density over the antenna was varied in the range of approximately  $0.5 < n_e/n_{e,cr} < 5$  by adjusting the strength of the incident shock. The experimental results obtained, including the arc lengths for the five diodes, are summarized in Table II.

The RAM C-II antenna was operated at 11.25 inches from the leading edge. The major differences between the 6.75 and 11.25-inch measuring stations are the boundary-layer thickness and the peak value of the electron density. Several experiments were performed at the 11.25-inch location and these spanned the range from  $0.2 < n_e/n_{e,cr} < 2.1$ . The results of these experiments are given in Table III.

Figure 26 is typical of the oscilloscope records obtained for the reflectometer diodes. The test-flow duration is noted on the oscilloscope records.

The 50- $\mu$ sec duration pulse near the right side of these records is the zero-signal level obtained by turning off the TWT power supply with a gating pulse. The horizontal line is the no-plasma signal level recorded approximately two milliseconds prior to plasma arrival at the plate leading edge. A limited number of lower confidence-level data points can be obtained from the post test-time plasma. In some cases this was done and the data points are so designated in Table II and III.

All of the reflectometer data obtained in the CO plasma with this antenna are compared with the theoretical predictions on Fig. 27 for the RAM C-III antenna and on Fig. 28 for the RAM C-II antenna. The circles represent the uncertainty of the measurements as determined by the intersection of the five diode voltages. Much of the phase rotation uncertainty associated with these records was due to the #1 diode arc being consistently long. Care was taken to calibrate each of the oscilloscopes just prior to and after each experiment using a vacuum-tube volt meter, thus it is doubtful that the difficulty is associated with a calibration error. This diode appeared to operate satisfactorily when obtaining the free-space admittance for which the circle of uncertainty was comparatively small. The estimated uncertainty in the value of  $n_e/n_{e\text{cr}}$  is also given on Figs. 27 and 28.

The theoretical results presented in Fig. 27 were obtained using a parabolic profile of electron density that represented the best fit to the electron-density profile measured at the antenna location ( $\delta \sim 1.2$  inch). The comparison between the theoretical and the experimental values of  $n_e/n_{e\text{cr}}$  presented in Fig. 27 indicates a consistent difference of about 20 to 40 percent. This discrepancy is possibly due to an uncertainty in the experimental determination of the free-stream electron density over the antenna. Recall that the admittance measurements and the boundary-layer probing measurements were performed in separate experiments in order to avoid interference effects. Microwave interferometer measurements of the averaged free-stream electron density were performed at 1 inch and 11 inches upstream of the plate leading edge for all experiments and thus provided the only quantitative link between the measurements. When obtaining the admittance measurements, these microwave interferometer results were extrapolated to the antenna locations in order to obtain an estimate of the free-stream electron density assuming that the expanding plasma was not influenced by the presence of the model. Figures 22 and 24 illustrate that the extrapolation described above is reasonably good, but an error of 20 to 40 percent in the estimated electron density would be within the uncertainty.

Figure 28 presents a comparison of the experimental data with the theoretical results for the RAM C-II antenna. These results were obtained with the antenna located at 11.25 inches from the plate leading edge. The experimentally determined electron-density profile given in Fig. 24 was used in order to obtain the theoretical results presented in Fig. 28. The results obtained using this antenna are similar to those obtained for the C-III antenna in that the experimentally determined reflection coefficients are about 30 percent less than the theoretical values at values of  $n_e/n_{e\text{cr}}$  less than 1. The agreement becomes better as the electron density ratio increases to

values greater than 1. The experimentally determined phase rotations are shown to be generally in better agreement with the theory except at the very small values of  $n_e/n_{e\text{cr}}$ . Phase measurements at low values of  $n_e/n_{e\text{cr}}$  is more difficult than at higher values because of the small reflection coefficients.

### 3.6 Conclusions

Two circular-aperture flush-mounted antennas, for which a theoretical description of the antenna-plasma interaction has been developed, were operated in the presence of ionized boundary layers of low collision frequency. The boundary-layer electron-density profile was independently measured using voltage-swept thin-wire probes and this measured profile was used as an input condition for the theory. Both antennas demonstrated marked increases in reflection coefficient and phase rotation when the peak electron density over the antenna approached critical. In general, good agreement was obtained between the predicted and measured reflection coefficient and phase rotation over the range of  $m_e/n_{e\text{cr}}$  studied. These results illustrate that the input admittance method can be effectively used to obtain local measurements of electron density. Calculations of the admittance of a flush-mounted antenna have been presented as useful working curves from which boundary-layer thickness and free-stream electron density can be determined. These curves can be used at arbitrary frequencies by appropriate electromagnetic scaling.

## 4. USE OF POSITIVELY BIASED ELECTROSTATIC PROBES TO OBTAIN ELECTRON DENSITY IN COLLISIONLESS FLOWS

### 4.1 Introduction

There are several well known (Refs. 57-61) advantages of using the electron-current portion of an electrostatic-probe current-voltage characteristic for determination of electron density. Perhaps the most important advantages are that the collected current is independent of the ion mass and also independent of the probe orientation relative to the mass motion of heavy particles because of the relatively high electron thermal speed. In addition, the collision cross sections for electron-particle interactions are generally smaller than those for ion-particle interactions suggesting that the collisionless-flow approximation should be valid over a greater range of gas densities. Further, the electron current collected by the probe can be made insensitive to the electron temperature by working at large probe voltages. Sutton (Ref. 62) has described the feasibility of using thin-wire probes biased for electron current in order to measure electron-density fluctuations in hypersonic turbulent wakes. However, relatively few (Ref. 61) experimental studies have been reported in the literature that have attempted to show that the electron-current region can be successfully used to obtain these electron-density measurements within the framework of existing theoretical results. It is thus the purpose of this paper to report the results of an experimental study undertaken in order to determine if the existing theoretical results of Laframboise (Ref. 36) for the current collected by thin-wire probes operating in the free-molecular flow regime could be successfully used in the electron-current region. Many people have illustrated the correctness of this theory for the ion-current region. The details of Laframboise's work are well known and will not be described here.

The current studies were motivated by the availability of in-flight voltage-swept probe data obtained by Jones (Ref. 63) as part of the Langley Research Center RAM program. The voltage applied to his probes was sufficiently positive that the probes were swept well into the electron-current region at altitudes for which the free-molecular flow approximation should be valid. Electron densities have been obtained from the ion-current portion of his probe characteristics and are reported elsewhere (Ref. 63).

Center (Ref. 61) used a pressure-driven shock tube to produce a plasma behind the incident shock in which he performed probe experiments under free-molecular flow conditions. The voltage on his probes was held constant during the experiment because of the rapidly varying conditions behind the incident shock. By performing a series of experiments he was able to construct the current-voltage characteristic and subsequently show that the experimental data are predicted by the theoretical results of Laframboise (Ref. 36). The results presented in this paper are in agreement with those described by Center. However, the fluid-flow environments in which the experiments were performed were significantly different and the probe characteristics were obtained by sweeping the probe voltage instead of maintaining constant voltage.

#### 4.2 Experimental Apparatus and Technique

A pressure-driven shock tube was used to produce a reservoir of high-temperature gas which was subsequently expanded in a conical nozzle constructed of Fiberglas. A detailed discussion of this shock tube and nozzle is given in Refs. 64 and 65.

The majority of the probe measurements reported here were performed in the boundary layer of a sharp flat plate mounted in the nozzle flow such that its leading edge was 22.5 inches from the throat and its top surface was on the nozzle centerline. A few experiments were also performed in the absence of the plate with the probes located on the nozzle centerline at 32.5 inches from the throat. An independent and simultaneous measurement of averaged free-stream electron density was obtained at 11.5 and 21.5 inches (31.5 inches for the free-stream experiments) from the throat using microwave interferometers operating at 35 and 17 GHz, respectively. Carbon monoxide was used as the test gas for the boundary-layer experiments. The carbon monoxide test gas was expanded from an equilibrium reservoir condition of  $7060^{\circ}$  K at 17.3 atm pressure. However, the free-stream measurements were performed in both carbon monoxide and nitrogen test gases. The nitrogen test gas was expanded from an equilibrium reservoir condition of  $7200^{\circ}$  K at 17.1 atm pressure. Previous boundary-layer experiments have been reported (Ref. 52) which used nitrogen as the test gas but in these measurements the probes were not swept into the electron-current region.

The carbon monoxide used here was ultra high-purity grade supplied by Air Products and Chemicals Inc. The principal impurity in this gas was nitrogen estimated to be on the order of 1500 to 2000 ppm. The nitrogen test gas was ultra-pure carrier grade also supplied by Air Products and Chemicals Inc. A chemical analysis of the nitrogen gas indicated the following: oxygen less than 0.5 ppm, total hydrocarbons less than 1 ppm, and water less than 0.15 ppm.

The probes used in these experiments were constructed by surrounding 0.004 in. diameter tungsten wires with a quartz envelope, leaving a nominal 0.400 in. length of bare wire exposed. Immediately prior to each run, the tungsten oxide is removed by placing the probe in a dilute solution of sodium hydroxide and passing approximately 400  $\mu$ a of current through the circuit for approximately 10 minutes.

#### 4.3 Discussion of Results

By using Laframboise's (Ref. 36) theory to obtain electron temperatures and electron densities from the experimentally determined probe characteristics, it has been assumed that the flow conditions were collisionless with respect to the probe diameter. At all of the measuring stations, the electron mean free paths were many times greater than the probe diameter. Because of the relative insensitivity of electron collection to the magnitude of the ion-neutral

and neutral-neutral mean free paths, it is anticipated that the electron temperature deduced from the electron-retarding region and the electron density deduced from the electron-current region of the probe characteristic should be correct. The ion-neutral mean free path was the shortest, being slightly greater than the probe diameter at the upstream measuring station. However, the electron-density results presented later in this paper suggest that the ion-neutral mean free path apparently had a relatively insignificant influence on the collected ion current. The calculated mean free paths and species concentrations in the expanding carbon monoxide and nitrogen flows used for the present experimental test conditions are given in detail in Refs. 30 and 66, respectively.

It is important to note that the carbon monoxide test gas used in the work reported in Ref. 30 had substantially less impurities (25 ppm nitrogen) than that used in the present experiments (1500 to 2000 ppm nitrogen). It was not possible to obtain additional CO from Lif-O-Gen Inc. with the low nitrogen content. The additional nitrogen appeared to influence the chemical kinetics of the expanding plasma by decreasing the electron-density level by a factor of approximately two throughout the expansion. For the purposes of this study the details of the kinetics are important and had to be considered. Even with the nitrogen present, the dominant ion in the expansion was calculated to be  $C^+$  so that ion mass 12 was used in the analysis of the ion-current data. The method of probe-data reduction used here has been outlined in detail in Ref. 67 and will not be repeated. The familiar normalized ion-and electron-current densities ( $i_+$  and  $i_-$ ) were taken from Laframboise's theoretical results for  $T_i/T_e = 0$  and are given in Figs. 29 and 30, respectively. For the experimental conditions considered here the  $T_i/T_e = 0$  theoretical results are satisfactory since the free-stream ion temperature to electron temperature ratio was on the order of 0.1 to 0.2.

Table IV presents a summary of the experimental results obtained as part of this study. Included in this table are the electron densities determined from the ion- and electron-current portions of the current-voltage characteristics, the calculated values of  $R_p/\lambda_D$  for these regimes, a comparison of  $(V_\infty - V_f)$  obtained from the tangent intercept technique and an estimate obtained from the theory, the electron temperatures determined from the electron-retarding region, and electron densities determined using a microwave interferometer when free-stream probe measurements are given.

Figures 31 and 32 present the ion-current region and the electron-retarding and electron-current regions respectively of the probe characteristic obtained in the boundary layer for a typical experiment. On Figure 31 the ion current is utilized to deduce the number-density at  $\chi_p = -25$ . For this particular case the value of  $(R_p/\lambda_D)^2 i_+$  was 16.55 which is in the orbital-motion limited regime. The corresponding value of  $R_p/\lambda_D$  was 1.72 and the floating potential was -0.43 volts. The electron density calculated using the theoretical results of Laframboise (Ref. 36) was  $1.2 \times 10^{10} e^-/\text{cm}^3$ . Also shown on Fig. 31 is the electron density calculated using the electron current at a potential of  $\chi_p = +5$ . The electron current at  $\chi_p = +7.5$  was also used but the resulting electron density was essentially unchanged. The value of

$(R_p/\lambda_D)^2 \lambda_+$  at  $\chi_p = +5$  was calculated to be 7.36 and the corresponding value of  $R_p/\lambda_D$  was 1.78 which is reasonably close to the value calculated from the ion current. The number density deduced from the electron current was  $1.3 \times 10^{10} e^-/\text{cm}^3$  which is in very good agreement with the value previously obtained from the ion-current portion of the characteristic.

The electron temperature was obtained from the results presented in Fig. 32. The value of  $e/kT_e$  for this particular experiment was 5.37 or  $T_e = 2160^\circ \text{ K}$ . By extrapolating the line faired through the retarding-field region to intersect with a line faired through the electron-current region one can obtain an estimate of the plasma potential. For this case, the extrapolation gave a plasma potential of +0.5 volts; the floating potential, which is easily determined from Fig. 31 was -0.43 volts resulting in an experimental value of  $(V_\infty - V_f)_{\text{exp}} = 0.93$  volts. Using the theoretical expressions given in Eqs. 1 and 2 of Ref. 59 and equating  $j_i$  to  $j_e$  at the floating potential, one can obtain an estimate of the value of  $(V_\infty - V_f)_{\text{est}}$  from the theory to be given by  $(kT_e/e) \ln (m_i/m_e)^{0.5} \lambda_+$ . We will refer to this value as  $(V_\infty - V_f)_{\text{est}}$  and compare it in Table IV with  $(V_\infty - V_f)_{\text{exp}}$  determine from the experimental data using the tangent intercept method in a manner illustrated on Fig. 32. For the purposes of this paper,  $\lambda_+$  was assumed to be equal to 1.0 which results in a maximum error in  $(V_\infty - V_f)$  of 10 to 12 percent for the conditions of these experiments.

Assuming  $\text{C}^+$  to be the dominant ion, then  $(V_\infty - V_f)_{\text{est}} \approx (T_e/2320)$ ; then assuming  $\text{N}^+$  to be the dominant ion in the nitrogen experiments, gives  $(V_\infty - V_f)_{\text{est}} \approx T_e/2290$ . Using the previous expression for the  $\text{C}^+$  ion the value of  $(V_\infty - V_f)_{\text{est}}$  for the results presented in Figs. 31 and 32 is equal to 0.932 as compared to the experimental value of 0.93. The agreement between  $(V_\infty - V_f)$  estimated from the theory and the value obtained from the experiment was not always this good (as illustrated in Table IV but in general the agreement was within 0.2 volts).

Table IV also contains number-density results obtained in the free-stream flow using both the microwave interferometer and voltage-swept probes. For the CO plasma, the probe-determined electron densities were in good agreement with each other (ion and electron current) but in two of the three cases they were about 30 to 40 percent less than the microwave results. This same general trend was reported in Ref. 30 but the reason for the disagreement is unknown. Probe and microwave-interferometer results for a nitrogen plasma are also reported in Table IV. With the exception of the final entry in the table, the number densities determined from the ion- and electron-current portions of the characteristic are in good agreement. In all cases, the number densities determined from the ion current were in good agreement with the microwave-interferometer measurements.

Figures 33 and 34 present a comparison of the experimentally determined current-voltage characteristic with the theoretical characteristic of Laframboise. The data used here are the same as those given in Figs. 31 and 32. To obtain the comparison, the plasma potential ( $V_\infty$ ) was assumed to be 0.5 volts consistent with Fig. 32 and the experimental characteristic was matched to the

have been made wholly or in part in the previous analyses and the justification for these assumptions can be found in Refs. 15, 16, 18, 19.

Based on the above assumptions the governing equations for the viscous, ionized shock layer in the merged-layer regime become

$$\frac{\partial}{\partial x} (\rho u r^t) + \frac{\partial}{\partial y} (\rho v r^t) = 0, \quad (1)$$

$$\rho u \frac{\partial u}{\partial x} + \rho v \frac{\partial u}{\partial y} = - \frac{\partial}{\partial y} \left( \mu \frac{\partial u}{\partial y} \right), \quad (2)$$

$$\frac{\rho u^2}{R_c} = - \frac{\partial p}{\partial y}, \quad (3)$$

$$\begin{aligned} \rho u \frac{\partial H}{\partial x} + \rho v \frac{\partial H}{\partial y} &= - \frac{\partial}{\partial y} \left\{ \frac{\mu}{P_r} \frac{\partial}{\partial y} \left[ H + (P_r - 1) \frac{u^2}{2} \right] \right\} \\ &+ \frac{\partial}{\partial y} \left\{ \frac{\mu}{P_r} (L_{e_i} - 1) \sum_i h_i \frac{\partial C_i}{\partial y} \right\}, \end{aligned} \quad (4)$$

$$\rho u \frac{\partial C_i}{\partial x} + \rho v \frac{\partial C_i}{\partial y} = - \frac{\partial}{\partial y} \left( \rho D_i \frac{\partial C_i}{\partial y} \right) + \dot{\omega}_i, \quad (5)$$

$$p = \rho R T \sum_i (C_i / m_i). \quad (6)$$

These equations express the conservation of mass, momentum, energy, and chemical species, respectively, along with an equation of state. (See Fig. 1 for a description of the flow field.) The eleven chemical species considered are: O<sub>2</sub>, N<sub>2</sub>, O, N, NO, NO<sup>+</sup>, O<sup>+</sup>, N<sup>+</sup>, O<sub>2</sub><sup>+</sup>, N<sub>2</sub><sup>+</sup>, and e<sup>-</sup>. With the two-layer model of Cheng, Equations 1-6 are applied to the viscous shock layer allowing for the diffusion of the species into the shock-transition zone by using the modified Rankine-Hugoniot conditions. Analysis of the entire flow field as performed in Ref. 19 reinforces the applicability of the two-layer model, and thus only the viscous shock layer will be considered here. The chemical reactions and their associated reaction rate coefficients used simultaneously for dissociation and ionization are given in Table I and are discussed in detail in Ref. 69. It is appropriate to note here that eleven reactions are used involving only neutral species and fifteen reactions involving charged species.

In obtaining solutions to the differential equations, the coordinates and the flow variables were first transformed, and the Karman-Pohlhausen integral method was applied because of the ease of application and the relatively small computation time without unduly sacrificing the accuracy of the results (Refs. 2, 21, 69). The transformed equations were integrated along the body from the stagnation region through the sphere-cone junction to the afterbody conical section by using the Adams-Molton predictor-corrector method. In order to simplify the analysis while accounting for changes in shock shape along the body, the distribution of the shock angle was initially assumed and updated from the results. Based on the cases considered in the present analysis, two iterations were usually sufficient to obtain the correct shock shape for the body. The solutions are obtained in terms of the flow variables such as the velocity and temperature, and in terms of the chemical-species distributions in the shock layer and along the body surface.

The present analysis was applied to two different bodies: a  $9^\circ$  sphere cone with a 6 inch nose radius at 233 kft and a  $20^\circ$  sphere cone with a 4 ft nose radius at 280 kft and 310 kft. The latter geometry was used to approximate the windward plane of symmetry flow configuration of a space shuttle. The free-stream velocity for both bodies was taken to be 25,100 ft/sec. Solutions were obtained for a flow field including not only the nose region but also the far downstream region ( $\chi/R_N \sim 90$ ).

### 5.3 Results and Discussion

Figure 35 shows the distributions of the viscous shock-layer thickness and the temperature behind the shock for the two ( $9^\circ$  and  $20^\circ$ ) sphere-cone bodies. It is noted that the temperatures behind the shock in the nose region are about equal for both bodies, due to the same free-stream kinetic energy being converted into thermal energy there. On the other hand, great divergence in the static temperatures is noted in the downstream region beyond the sphere-cone junction. This is due primarily to the shock shape which takes on an angle close to the respective semi-cone angles ( $\Theta_c$ ). The shock standoff distance normalized with respect to its own nose radius, i.e.,  $\Delta/R_N$ , also displays the effect of the semi-cone angle of the two bodies considered. However,  $T_{sh}$  and  $\Delta/R_N$  for the hemisphere  $-20^\circ$  cone were essentially the same as a function of  $\xi$  for both 280 and 310 kft.

The temperature profiles within the viscous shock layer are shown in Figs. 36-38 for  $\alpha = 20^\circ$  and  $\alpha = 9^\circ$ , respectively. In the stagnation region, the maximum temperature is located immediately behind the shock, while in the downstream region the peak temperature moves toward the body surface, signifying the appearance of the viscous heating effect in a layer near the body. In a region sufficiently far downstream, this layer is thin compared to the shock-layer thickness, thus "recovering" a thin boundary layer. Similar results were observed by Cheng (Ref. 15) and Davis (Ref. 70) in their analyses of hyperboloidal bodies. Thus a continuous solution is obtained which encompasses the "merged-layer" regime in the stagnation region through a "vorticity-interaction" regime (Refs. 16, 18) to a "boundary-layer" regime in the far downstream region of a blunted cone. Comparison of Figs. 36 and 37 with

Fig. 38 indicates a significant difference in the magnitude of  $T/T_{sh}$  for a given value of  $\xi$ . This is primarily due to the difference in  $T_{sh}$  for the two bodies as illustrated on Fig. 35.

The heat-transfer characteristics for a sphere cone at high altitudes are presented in Figure 39 in terms of the Stanton number ( $St$ ) along the body surface. The figure shows diminishing local heat-transfer rates in the downstream direction, as in Refs. 2 and 15. In addition, the results display the effect of the cone angle on the Stanton number such that the decrease is greater for the  $\Theta_c = 20^\circ$  case than for the  $\Theta_c = 9^\circ$  case. The influence of altitude can also be seen by comparing the  $\Theta_c = 20^\circ$  results at 310,000 ft with those at 280,000 ft.

The distributions of the peak levels of the dissociated chemical species along the body are shown in Figs. 40 and 41 for the  $\Theta_c = 20^\circ$  cases. The relative mass fractions of  $N_2$  and  $O_2$  are not shown. Similar results were obtained for  $\Theta_c = 9^\circ$  but are not included here. It is interesting to note from Figs. 40 and 41 that the present chemical nonequilibrium distributions for the neutral species (and also the ionized species) display a minimum far downstream (on the order of ten nose radii) of the junction point and show a gradual increase in their levels beyond this point. This type of behavior was observed for the case of a thin boundary-layer flow over a blunted cone at low altitudes, e.g., Refs. 71, 72. The present results for a viscous shock layer appear to display similar bluntness effects on the flow. It is also important to note the relative magnitudes of the atomic ions  $N^+$  and  $O^+$  and the diatomic ion  $N_2^+$  in the nose region. In addition, the  $O_2^+$  ion is shown on Fig. 41 to be important in the downstream region for the 310 kft results. These calculations suggest that all of the air ions should be included in the chemical model.

The electron-density profiles calculated for a nonequilibrium, reacting gas are shown in Figs. 42 and 43 for  $\Theta_c = 20^\circ$  cases at various downstream locations. For the 280,000 ft calculation, the electron-density levels sharply decrease in the downstream direction until at about ten nose radii a minimum is reached due to expansion around the sphere-cone junction, and thereafter the number density gradually increases as mentioned previously. In the case of the 310,000 ft calculations, this minimum occurred at about 30 nose radii downstream. Similar results were also obtained for the  $\Theta_c = 9^\circ$  case for both the nose region and the far downstream region but are not included here.

#### 5.4 Estimated Plane-Wave Transmission Coefficients for an Approximate Space-Shuttle Flow Field

In order to obtain some estimate of the potential communications difficulties with the space-shuttle orbiter during earth entry, plane-wave transmission coefficients were calculated for several axial locations along the windward generator at several trajectory points. These calculations are very approximate at the present time because an accurate flow-field description for the orbiter is not available. However, by approximating

the flow field, the electron-density and collision-frequency distributions necessary for the E-M wave calculations were obtained, including non-equilibrium chemical reactions. Only pure air chemistry was included in these calculations and the chemical reactions and associated reaction rate coefficients are given in Table 1. The possible influence of ablation-product ionization on the electron-density level was not included. This consideration is particularly important at the lower altitudes where the electron density from pure air ionization is decreasing.

In an effort to make maximum use of published work, the approximate flow field obtained by Lordi, Vidal and Johnson (Ref. 68) for the windward plane of symmetry of a blunted delta orbiter was used at altitudes of 250,000 ft and below. These authors located streamlines in the inviscid flow field and determined the pressure distributions for these streamlines. They also performed calculations of the nonequilibrium species distributions at several altitudes of interest in this study for several of the streamlines. Because flow-field calculations were required over a large altitude range, we have used their calculations where available and performed additional nonequilibrium calculations at other trajectory points of interest by utilizing the streamline locations and pressure distributions supplied by Lordi and Vidal. It is important to note that the only ion included in their calculations was  $\text{NO}^+$ . For their purposes, including  $\text{NO}^+$  was appropriate but for the purposes of estimating electron-density levels, future calculations should include the remaining ions of air. Therefore, to be consistent, we used only the  $\text{NO}^+$  ion in our low-altitude streamtube calculations. However, as previously noted, the additional ions of the air model,  $\text{N}_2^+$ ,  $\text{O}_2^+$ ,  $\text{N}^+$ , and  $\text{O}^+$ , were used in our high-altitude viscous-layer analysis.

The plane-wave transmission coefficients as a function of altitude are shown in Fig. 44 to 48 for the windward generator at  $S/R_N = 1.22, 10, 30, 50$  and 90. Carrier frequencies of 100, 2200 and 10,000 MHz have been considered in this study. For altitudes of 250,000 ft and below, the 20° angle of attack flow-field description of Lordi, et.al. was used to obtain the required electron-density and collision-frequency distributions. Above 250,000 ft the viscous flow-field analysis for a 20° blunted cone described earlier in this report was used. For the purposes of the E-M wave calculations, the gradient of electron density in the direction of propagation was accounted for by assuming the plasma layer to be composed of many smaller homogeneous slabs. However, the calculation technique (Ref. 73) is restricted in that it requires that the gradients normal to the direction of electromagnetic propagation be negligible.

A typical shuttle entry trajectory and the trajectory points for which calculations were performed are given on Fig. 49. The calculations were based on an early trajectory and do not correspond exactly to the updated trajectory given on Fig. 49. However, for the preliminary nature of this study, the correspondence is sufficiently close. It is significant to note that for an operating frequency of 2200 MHz, the transmission from an antenna located at  $X/R_N$  of 1.22 will probably be significantly attenuated for a

period of approximately 15 minutes during the entry trajectory as a result of pure air ionization.

The preliminary nature of the results described here must be emphasized. They are presented here only for the purpose of estimating the severity of a potential problem. Before the selection of antenna frequencies and locations is made, it is recommended that a more detailed description of the flow field should be obtained and that the potential influences of ablation product ionization should be assessed.

As mentioned above, the results of the previously published flow field work of Lordi, Vidal and Johnson for the windward plane of symmetry of a blunted delta orbiter was used to obtain streamline locations and pressure distributions, as well as electron-density distributions for some streamlines, at altitudes below 250,000 ft. In order to provide a more complete report, the electron-density distributions obtained from these calculations are given in Figs. 50-53. The reader is cautioned that the only positive ion used in these calculations was  $\text{NO}^+$  and that ablation-product contamination at low altitudes was not considered.

### 5.5 Conclusions

A theoretical analysis is presented which yields a continuous solution for a nonequilibrium viscous shock-layer flow around a sphere cone at high altitudes. Results are given for two different bodies ( $\Theta_c = 9^\circ$  and  $20^\circ$ ) in terms of the temperature, the Stanton number and the electron-density distributions. These calculations show the effects of the bluntness, chemical non-equilibrium and the semi-cone angle on the above quantities. The present analysis was undertaken as a first step in the possible application of an approximate technique to the calculation of a complicated flow field surrounding the space shuttle.

Plane-wave transmission coefficients were calculated for several axial locations along the windward generator of a  $20^\circ$  half-angle spherically blunted cone and a blunted delta at  $20^\circ$  angle of attack. These calculations considered only pure air ionization. Transmission difficulties would probably be encountered from approximately 300 to 200 kilofeet for frequencies less than 2200 MHz. Ablation product ionization would tend to increase this altitude range. The transmission-coefficient results presented here are very approximate. Before the antenna frequencies and locations are selected for the shuttle vehicle, a more detailed analysis should be performed.

## 6. POST-RETRACTION ELECTROSTATIC-PROBE RESULTS

Voltage-swept thin-wire electrostatic probes were flown on the RAM C-III vehicle as described in detail in Section 2. At an altitude of approximately 200,000 ft. the probes were retracted into the base-flow region but the voltage sweeping was continued. It was therefore the purpose of this study to investigate these post-retraction data and determine if useful electron-density and electron-temperature results could be obtained.

The complex nature of the flow field in the base-flow region precluded use of the ion-current portion of the probe characteristic for determining the electron density. However, the electron-current portion of the characteristic could possibly be used. As discussed in Section 4, the collected current in this portion of the characteristic is independent of the ion mass and also independent of the probe orientation relative to the mass motion of heavy particles. Because of the relative insensitivity of electron collection to the magnitude of the ion-neutral and neutral-neutral mean free paths, it is anticipated that the electron temperature deduced from the electron-retarding region, where the electron current is much larger than the ion current, should be correct.

The flight data were reviewed in some detail and it was determined that those data in the altitude range of 190,000 to 180,000 ft were relatively free of foreign materials which were injected into the flow field as part of the flight-test program. Therefore, it was felt that the probe characteristics obtained in this altitude range could be used to infer the electron temperature and electron density in the base region. The technique used to obtain these values from the probe characteristics has been previously described in Sections 2 and 4 and will not be repeated here.

Figures 54 and 55 illustrate the base region electron-density and electron-temperature data for the RAM C-III flight for the altitude range 190,000 to 180,000 ft. One of the four thin-wire probes was not operating during the post-retraction period so that results could only be obtained for three locations in the base region instead of four. The location of the probe relative to the vehicle shoulder is illustrated on the figures. The electron density at 7 to 10 cm. of the shoulder was on the order of  $3 \text{ to } 4 \times 10^{10} \text{ e}^-/\text{cm}^3$  but fell off rapidly to approximately  $2 \times 10^9$  at 13 cm. It is difficult to compare these flight results with predicted values because of the complexities involved in determining the flow field in the near-wake region. However, one can make comparisons with electron densities calculated for the shoulder prior to expansion into the base region in order to obtain an indication of whether or not the results are reasonable. Huber\* has calculated the peak electron number density in the plasma layer prior to expansion to be approximately  $2 \times 10^{11} \text{ e}^-/\text{cm}^3$  for the altitude range of interest. Qualitatively, the flight data nearest the shoulder appear to be comparable with the calculated values.

\* These unpublished results were generously supplied to us by Mr. Paul Huber of NASA, Langley Field.

Figure 55 suggests that the electron temperature in the base region was reasonably uniform between 8 and 13 cm. at a value of about 4000 to 5000° K. The peak heavy-particle translational temperature in the plasma layer at the shoulder prior to expansion calculated by Huber was approximately 4000° K. Once again, the flight data are qualitatively compatible with the calculations suggesting that the electron temperature in the base region may be nearly equal to the heavy-particle temperature just prior to the expansion.

## 7. THREE-DIMENSIONAL, VISCOUS SHOCK LAYER FOR SPACE SHUTTLE-TYPE BODY

Section 5 of this report described preliminary estimates of the high altitude heat-transfer and electron-density distributions that were obtained for the windward plane of symmetry by approximating the shuttle vehicle as a blunted cone at zero angle of attack. These calculations were used to estimate the electromagnetic-wave transmission coefficients at various vehicle stations for a typical entry trajectory. The purpose of the work described in this section was to formulate a method for obtaining solutions of the viscous shock layer for a shuttle-type body at angle of attack so that the preliminary results presented in Section 5 can be improved and so that calculations can be performed for locations other than the windward generators.

The viscous hypersonic flow around a space shuttle vehicle at high altitudes at angle of attack is described by the Navier-Stokes equations (Ref. 74) and other continuum conservation equations (Ref. 75). The coordinate system chosen is "body oriented", similar to the conventional boundary-layer coordinate system (Ref. 18).

Based on experience with the axisymmetric viscous-flow analyses (Refs. 2, 20, 41, 69), the following assumptions are made:

- 1) a thin shock layer
- 2) two-layer model of Cheng (Ref. 15)
- 3) Negligible changes in the flow properties such as the velocity and total enthalpy due to the chemical reaction in the flow field
- 4) constant Prandtl and Schmidt numbers
- 5) binary diffusion due to concentration gradient only
- 6) negligible nonequilibrium effects due to electronic and vibrational relaxation
- 7) ambipolar diffusion for the electrons and ions

These assumptions have been made in part or wholly in the previous analyses and the rationale for these assumptions may be found, for example, Refs. 15, 18, 19

### BASIC EQUATIONS

With the above assumptions the governing equations for the three-dimensional, viscous, ionized shock layer become s (see Figure 1 for a description of the flow field).

Continuity:

$$\frac{\partial}{\partial x} (\rho u r) + \frac{\partial}{\partial y} (\rho v r) + \frac{1}{r} \frac{\partial}{\partial \phi} (\rho w r) = 0$$

Streamwise Momentum:

$$\rho \left( u \frac{\partial u}{\partial x} + v \frac{\partial u}{\partial y} + \frac{w}{r} \frac{\partial u}{\partial \phi} - \frac{w^2}{r} \frac{dp}{dx} \right) = - \frac{\partial p}{\partial x} + \frac{\partial}{\partial y} \left( \mu \frac{\partial u}{\partial y} \right)$$

Transverse Momentum:

$$\rho \left( u \frac{\partial w}{\partial x} + v \frac{\partial w}{\partial y} + \frac{w}{r} \frac{\partial w}{\partial \phi} + \frac{uw}{r} \frac{dp}{dx} \right) = - \frac{1}{r} \frac{\partial p}{\partial \phi} + \frac{\partial}{\partial y} \left( \mu \frac{\partial w}{\partial y} \right)$$

Normal Momentum:

$$\frac{\rho u^2}{R_c} = \frac{\partial p}{\partial y}$$

Energy:

$$\rho \left( u \frac{\partial H}{\partial x} + v \frac{\partial H}{\partial y} + \frac{w}{r} \frac{\partial H}{\partial \phi} \right) = \frac{\partial}{\partial y} \left( \frac{\mu}{P_r} \frac{\partial H}{\partial y} \right) - \frac{\partial}{\partial y} \left[ \frac{(1-P_r)}{2P_r} \mu \frac{\partial}{\partial y} (u^2 + w^2) \right]$$

Species:

$$\rho \left( u \frac{\partial C_i}{\partial x} + v \frac{\partial C_i}{\partial y} + \frac{w}{r} \frac{\partial C_i}{\partial \phi} \right) = \frac{\partial}{\partial y} \left( \rho \infty \frac{\partial C_i}{\partial y} \right) + \dot{w}_i$$

State:

$$p = \rho R T \sum_i \left( \frac{C_i}{m_i} \right)$$

With the two-layer model of Cheng, these equations are applied to the viscous shock layer allowing for the diffusion of the species into the shock-transition zone by using the modified Rankine-Hugoniot conditions. The boundary conditions for a fully catalytic solid wall are:

at  $y = 0$ :

$$u = 0 ; v = 0$$

$$H = H_b(x, \phi)$$

$$p = p_b(x, \phi)$$

$$C_i = C_i(\infty) \quad (O_2, N_2)$$

$$C_i = 0 \quad (\text{ALL OTHER SPECIES})$$

at  $y = \Delta(x, \phi)$ ;

$$\rho_\infty v_\infty (u_e - u_\infty) = \mu_e \left( \frac{\partial u}{\partial y} \right)_e$$

$$\rho_\infty v_\infty (w_e - w_\infty) = \mu_e \left( \frac{\partial w}{\partial y} \right)_e$$

$$\rho_\infty v_\infty (H_e - H_\infty) = \frac{\mu_e}{P_r} \left( \frac{\partial H}{\partial y} \right)_e - \frac{1-P_r}{2P_r} \mu_e \frac{\partial}{\partial y} (u^2 + w^2)_e$$

$$\rho_\infty v_\infty (C_{i_e} - C_{i_\infty}) = \frac{\mu_e}{Sc_i} \left( \frac{\partial C_i}{\partial y} \right)_e$$

where

$$u_\infty = U_\infty (\cos \alpha \cos \beta - \sin \alpha \sin \beta \cos \phi)$$

$$v_\infty = -U_\infty (\cos \alpha \sin \beta + \sin \alpha \cos \beta \cos \phi)$$

$$w_\infty = U_\infty (\sin \alpha \sin \phi)$$

### Transformation

In solving the equations the following coordinate transformations are made:

$$d\xi \equiv \frac{dx}{R_N} ; \quad dn \equiv r d\phi$$

$$F \equiv \frac{1}{G} \int_0^y \frac{\rho}{\rho_\infty} \frac{dy}{R_N} ; \quad G \equiv \int_0^\Delta \frac{\rho}{\rho_\infty} \frac{dy}{R_N}$$

In addition two stream functions are introduced such that

$$\psi \equiv \rho_\infty U_\infty r^2 \cos \alpha \cdot f$$

$$S \equiv \rho_\infty U_\infty r^2 \sin \alpha \cdot g$$

Along with the nondimensional velocities  $U, W$  defined as

$$U \equiv \frac{u}{U_\infty \cos \beta \cos \alpha} ; \quad W \equiv \frac{w}{U_\infty \cos \beta \sin \alpha}$$

we obtain

$$\frac{\partial f}{\partial F} = \frac{UG}{Z} \cos \beta ; \quad \frac{\partial g}{\partial F} = \frac{WG}{Z} \cos \beta$$

With introduction of the above transformation, the equations become, after a series of manipulations:

Streamwise Momentum:

$$\begin{aligned} & \frac{\partial}{\partial \xi} (Z \cos^2 \beta G U^2) + \tan \alpha \frac{\partial}{\partial n} (Z \cos^2 \beta UW) \\ &= \tan^2 \alpha \cos^2 \beta \frac{dZ}{d\xi} GW^2 + \frac{Z \cos \beta}{K^2 G \cos \alpha} \frac{\partial}{\partial F} \left( l \frac{\partial U}{\partial F} \right) \\ & - \frac{Z R_N G}{Q U_\infty^2 \cos^2 \alpha} \left( \frac{1}{R_N} \frac{\partial p}{\partial \xi} + \frac{\partial F}{\partial x} \frac{\partial p}{\partial F} \right) + \cos \beta \frac{\partial}{\partial F} \left[ U \left\{ \frac{\partial}{\partial \xi} (Z^2 f) + Z^2 \tan \alpha \frac{\partial g}{\partial n} \right\} \right] \end{aligned}$$

Transverse Momentum:

$$\begin{aligned} \frac{\partial}{\partial \xi} (\mathcal{Z} \cos^2 \beta G U W) + \tan \alpha \frac{\partial}{\partial n} (\mathcal{Z} \cos^2 \beta G W^2) \\ = -G \cos^2 \beta \frac{d \mathcal{Z}}{d \xi} U W + \frac{\mathcal{Z} \cos \beta}{K^2 G \cos \alpha} \frac{\partial}{\partial F} \left( \ell \frac{\partial W}{\partial F} \right) - \frac{\mathcal{Z} R_N G}{\rho U_\infty^2 \sin \alpha \cos \alpha} \left( \frac{1}{R_N} \frac{\partial p}{\partial n} \right. \\ \left. + \frac{1}{r} \frac{\partial F}{\partial \phi} \frac{\partial p}{\partial F} \right) + \cos \beta \frac{\partial}{\partial F} \left[ W \left\{ \frac{\partial}{\partial \xi} (\mathcal{Z}^2 f) + \mathcal{Z}^2 \tan \alpha \frac{\partial g}{\partial n} \right\} \right] \end{aligned}$$

Normal Momentum:

$$\frac{\partial p}{\partial F} = \rho_\infty \frac{R_N}{R_c} G U_\infty^2 \cos^2 \beta \cos^2 \alpha U^2$$

Energy:

$$\begin{aligned} \frac{\partial}{\partial \xi} [(1-t_b) \mathcal{Z} G \cos \beta U \theta] + \tan \alpha \frac{\partial}{\partial n} [(1-t_b) \mathcal{Z} G \cos \beta W \theta] \\ = \frac{\mathcal{Z} (1-t_b)}{P_r K^2 G \cos \alpha} \frac{\partial}{\partial F} \left( \ell \frac{\partial \theta}{\partial F} \right) + (1-t_b) \frac{\partial}{\partial F} \left[ \theta \left\{ \frac{\partial}{\partial \xi} (\mathcal{Z}^2 f) + \mathcal{Z}^2 \tan \alpha \frac{\partial g}{\partial n} \right\} \right] \\ + \frac{\mathcal{Z} U_\infty^2 \cos^2 \beta}{K^2 G H_\infty \cos \alpha} \frac{\partial}{\partial F} \left[ \frac{(1-P_r)}{2 P_r} \ell \frac{\partial}{\partial F} (U^2 \cos^2 \alpha + W^2 \sin^2 \alpha) \right] \end{aligned}$$

Species:

$$\begin{aligned} \frac{\partial}{\partial \xi} [\mathcal{Z} G \cos \beta U C_i] + \tan \alpha \frac{\partial}{\partial n} [\mathcal{Z} G \cos \beta W C_i] \\ = \frac{\mathcal{Z}}{K^2 G \cos \alpha} \frac{\partial}{\partial F} \left( \frac{1}{S c_i} \frac{\partial C_i}{\partial F} \right) + \frac{\mathcal{Z} G R_N}{U_\infty \cos \alpha} \frac{\dot{w}_i}{\rho} + \frac{\partial}{\partial F} \left[ C_i \left\{ \frac{\partial}{\partial \xi} (\mathcal{Z}^2 f) + \mathcal{Z}^2 \tan \alpha \frac{\partial g}{\partial n} \right\} \right] \end{aligned}$$

where

$$\ell \equiv \frac{\rho \mu}{P_r \mu_r} ; \quad \mathcal{Z} \equiv \frac{r}{R_N} ; \quad K^2 = \frac{\rho}{P_r} \frac{\rho_\infty U_\infty R_N}{\mu_r} ; \quad t_b = \frac{H_b}{H_\infty}$$

and, for a solid wall:

$$f = \frac{G}{\mathcal{Z}} \cos \beta \int_0^F U dF ; \quad g = \frac{G}{\mathcal{Z}} \cos \beta \int_0^F W dF$$

At the conclusion of the present contract, the formulation has been completed but results have not been obtained. However, possible methods of solution have been investigated and some tentative conclusion regarding the most promising approaches are presented.

As methods of solution to the partial, non-linear differential equations, the integral method (Refs. 2, 20, 21, 69), the unsteady method (Refs. 76, 77), the explicit method (Refs. 78, 79), and the implicit method (Refs. 70, 80) were considered. From the viewpoint of quick but approximate results, the integral method has been shown (Refs. 2, 20, 21, 69) to be adequate, even in the three-dimensional flow situation (Ref. 81). If, however, more accurate and elaborate results are desired, the implicit scheme appears to be the most reasonable method, being usually free from convergence problem

even in the non-linear case. For the case of a three-dimensional incompressible, boundary-layer flow, initial success using the implicit scheme is reported in Ref. 80 and 82. However, because the geometry of the space shuttle is rather complicated, both the integral method and the implicit scheme should be investigated before settling on one particular method.

## APPENDIX A

Admittance data taken during the experiments are presented relative to a short circuit as are the values derived from the circular aperture theoretical model. In special cases, where the antenna is experimentally matched to free space or partially matched using tuning stubs, calculations must be adjusted accordingly\*.

No adjustments are necessary for RAM C-III antenna since the circular aperture theoretical model values include the natural mismatch of the aperture and plug. However, because the RAM C-II antenna admittance for the no plasma case was different from its natural value, adjustments were necessary. The equivalent circuit used to make the adjustments is shown below.

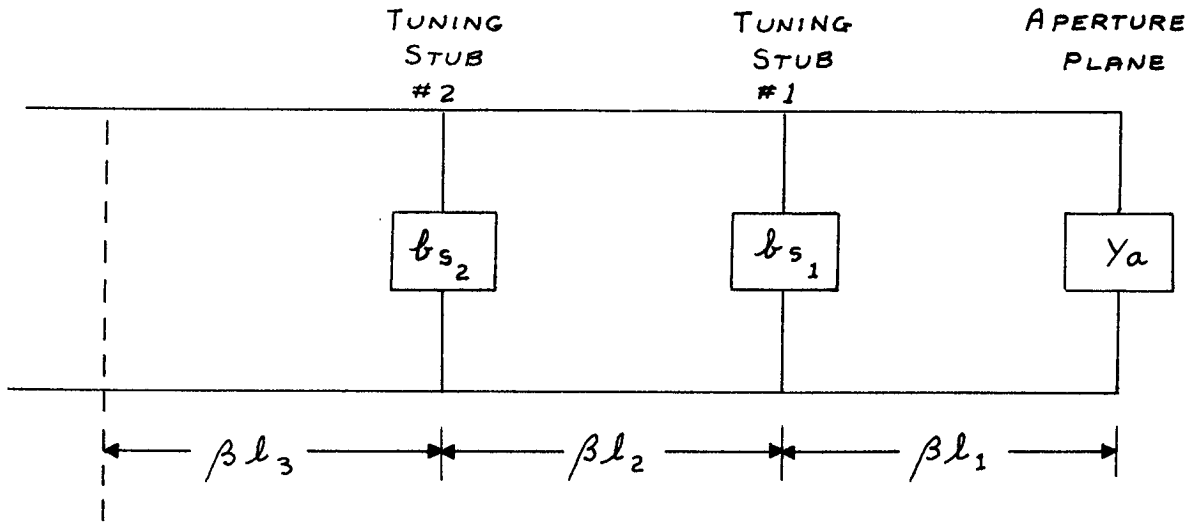


Figure A-1

The aperture admittance  $Y_a$  is transformed to a line length  $\beta l$ , to the first stub and the shunt susceptance,  $b_s$ , added to the network. Both  $\beta l_1$  and  $b_s$ , have values such that the aperture admittance of the antenna is matched to free space in the no plasma case. The admittance of the antenna at the terminals of the first stub is given by the transmission line equation

$$Y = \frac{Y_a + j \tan \beta l_1}{1 + j Y_a \tan \beta l_1} + j b_s$$

\* The authors are grateful to Dr. John Q. Howell for formulating these relationships and applying them to the unmatched antenna.

A second stub is added at a distance  $\beta l_2$  from the first stub such that the transformed admittance at the measurement reference plane is the same value as measured in the experiment for the no plasma case.

The position of the reference plane is the null location for a shorted aperture and is adjusted by selection of  $\beta l_2$  after the length  $\beta l_3$  is determined.  $\beta l_3$  and  $b_{s_2}$  were adjusted to give an admittance value of  $1.38 + j .18$  at the reference plane for the no plasma case. Only minor deviations from this value were observed during the course of the experiments as shown in Table II.

## REFERENCES

1. Dellinger, T.C., "Nonequilibrium Air Ionization in Hypersonic Fully Viscous Shock Layers", AIAA Paper No. 70-806, 3rd Fluid and Plasma Dynamics Conference, Los Angeles, California, June 1970.
2. Kang, S. W., "Nonequilibrium, Ionized, Hypersonic Flow Over a Blunt Body at Low Reynolds Number", AIAA Journal, Vol. 8, No. 7, July 1970, pp. 1263-1270.
3. Blottner, F.G., "Viscous Shock Layer at the Stagnation Point with Nonequilibrium Air Chemistry", AIAA Journal, Vol. 7, No. 12, December 1969, pp. 2281-2288.
4. Adams, J.C., Jr., "Shock Alip Analysis of Merged Layer Stagnation Point Air Ionization", AIAA Journal, Vol. 8, No. 5, May 1970.
5. Akey, N.D., and Cross, A.E., "Radio Blackout Alleviation and Plasma Diagnostic Results From a 25,000 ft/sec Blunt-Body Re-entry", NASA TN D-5615, February 1970.
6. Schroeder, L.C., "Flight Measurements at 25,000 ft/sec of Plasma Alleviation by Water and Electrophilic Injection", Proceedings of the Symposium on the Entry Plasma Sheath and its Effects on Space Vehicle Electromagnetic Systems, NASA SP-253, Vol. 2, 1971, pp. 77-100.
7. Jones, W.L. and Cross, A.E., "Electrostatic Probe Measurements of Plasma Surrounding Three 25,000 ft/sec Reentry Flight Experiments", Proceedings of the Symposium on the Entry Plasma Sheath and its Effects on Space Vehicle Electromagnetic Systems, NASA SP-252, Vol. 1, 1971, pp. 109-136.
8. Swift, C.T., Beck, F.B., Thomson, J. and Casfellow, S.L., "The RAM C-C S-Band Diagnostic Experiments", Proceedings of the Symposium on the Entry Plasma Sheath and its Effects on Space Vehicle Electromagnetic Systems, NASA SP-252, Vol. 1, 1971, pp. 137-156.
9. Grantham, W.L., "Flight Results of a 25,000 ft/sec Reentry Experiment Using Microwave Reflectometers to Measure Plasma Electron Density and Standoff Distance", NASA TN D-6062, Dec. 1970.
10. Croswell, W.F. and Jones, W.L., "Effects of Entry Plasma on RAM C-I VHF Telemetry Antennas", Proceedings of the Symposium on the Entry Plasma Sheath and its Effects on Space Vehicle Electromagnetic Systems, NASA SP-252, Vol. 1, 1971, pp. 183-2-2.

11. Jones, W. L. and Cross, A. E., "Electrostatic Probe Measurements of Plasma Parameters for Two Re-entry Flight Experiments at 25,000 ft/sec", NASA TN D-6617, April 1972.
12. Schroeder, L.C., Jones, W.L., Swift, C.T., and Cross, A.E., "Radio Blackout Alleviations by Fluid Injection and Plasma Measurements During the RAM C-III Reentry at 25,000 ft/sec," NASA TM X-2563, April 1972.
13. Evans, J.S., Schexnayder, C.J., and Huber, P.W., "Computation of Ionization in Reentry Flowfields", AIAA Journal, Vol. 8, No. 6, June 1970, pp. 1082-1089.
14. Huber, P.W., Evans, J.S., and Schexnayder, C.J., "Comparison of Theoretical and Flight-Measured Ionization in a Blunt Body Reentry Flow Field", AIAA Journal, Vol. 9, No. 6, June 1971, pp. 1154-1162.
15. Cheng, H.K., "The Blunt-Body Problem in Hypersonic Flow at Low Reynolds Number", Rept. AF 1285-A-10, Cornell Aeronautical Lab., Buffalo, N. Y.
16. Probstein, R.F., and Kemp, N., "Viscous Aerodynamic Characteristics in Hypersonic Rarefied Gas Flow", Journal of the Aerospace Sciences, Vol. 27, No. 3, March 1960, pp. 174-192.
17. Lee, R.H.C., and Ziertan, T.A., "Merged-Layer Ionization in the Stagnation Region of a Blunt Body", Proceedings of the Heat Transfer and Fluid Mechanics Institute, Stanford University Press, Stanford, Calif., 1967, pp. 452-468.
18. Hayes, W.D., and Probstein, R.F., Hypersonic Flow Theory, Academic press, New York, 1969, pp. 375-395.
19. Chung, P.M., Holt, J.F., and Liu, S.W., "Merged Stagnation Shock Layer of a Nonequilibrium Dissociating Gas", AIAA Journal, Vol. 6, No. 12, Dec. 1968, pp. 2372-2379.
20. Kang, S.W., "Hypersonic Low Reynolds-Number Flow Over a Blunt Body with Mass Injection", AIAA Journal, Vol. 7, No. 8, Aug. 1969, pp. 1546-1552.
21. Chung, P.M., and Anderson, A.D., "Dissociative Relaxation of Oxygen Over an Adiabatic Flat Plate at Hypersonic Mach Numbers", Rept. TN D-140, 1959, NASA.
22. Hall, J.G., Eschenroeder, A.Q., and Marrone, P.V., "Blunt Nose Inviscid Airflows with Coupled Nonequilibrium Processes", Journal of the Aerospace Sciences, Vol. 29, No. 9, Sept. 1962, pp. 1033-1051.

23. Wray, K. L., "Chemical Kinetics of High Temperature Air", AFBSD-TR-61-32, U.S. Air Force, June 1961.
24. Appleton, J. P., Steinberg, M. and Liquornik, D. J., "Shock-Tube Study of Nitrogen Dissociation Using Vacuum-Ultraviolet Light Absorption", Journal of Chemical Physics, Vol. 48, 1968, pp. 599-608.
25. Byron, S., "Shock-Tube Measurements of the Rate of Dissociation of Nitrogen", Journal of Chemical Physics, Vol. 44, 1966, pp. 1378-1388.
26. Allen, R. A., Keck, J. C., and Camm, J. C., "Nonequilibrium Radiation and the Recombination Rate in Shock-Heated Nitrogen", The Physics of Fluids, Vol. 5, 1962, pp. 284-291.
27. Cary, B., "Shock-Tube Study of the Thermal Dissociation of Nitrogen", The Physics of Fluids, Vol. 8, 1965, pp. 26-36; also the Physics of Fluids, Vol. 9, 1966, pp. 1046-1048 for revision.
28. Wentink, T., Sullivan, J. . and Wray, K. L., "Nitrogen Atomic Recombination at Room Temperature", Journal of Chemical Physics Vol. 29, 1958, pp. 231-232.
29. Dunn, M. G. and Lordi, J. A., "Measurement of Electron Temperature and Number Density in Shock-Tunnel Flows. Part II  $\text{NO}^+$  +  $e^-$  Dissociative Recombination Rate in Air", AIAA Journal, Vol. 7, No. 11, Nov. 1969, pp. 2099-2104.
30. Dunn, M. G., "Measurement of  $\text{C}^+$  +  $e^-$  +  $e^-$  and  $\text{CO}^+$  +  $e^-$  Recombination in Carbon Monoxide Flows", AIAA Journal, Vol. 9, No. 11, Nov. 1971, pp. 2184-2191.
31. Dunn, M. G. and Lordi, J. A., "Measurement of  $\text{O}_2^+$  +  $e^-$  Dissociative Recombination in Expanding Oxygen Flows", AIAA Journal, Vol. 8, No. 4, April 1970, pp. 614-618.
32. Dunn, M. G. and Lordi, J. A., "Measurement of  $\text{N}_2^+$  +  $e^-$  Dissociative Recombination in Expanding Nitrogen Flows", AIAA Journal, Vol. 8, No. 2, Feb. 1970, pp. 339-345.
33. Wray, K. L., Teare, J. D., Kivel, B., and Hammerling, P., "Relaxation Processes and Reaction Rates Behind Shock Fronts in Air and Component Gases", Proceedings of the 8th Symposium (International) on Combustion, The Combustion Institute, Williams and Wilkins, 1960, pp. 328-339.
34. Dunn, M. G. and Treanor, C. E., "Electron and Ion Chemistry in Flow Fields", Journal of Defense Research Series A, Spring 1970, pp. 23-52.

35. Bortner, M. H., ed., DASA Reaction-Rate Handbook, Defense Atomic Support Agency Information and Analysis Center, Oct. 1967.
36. Laframboise, J. G., "Theory of Spherical and Cylindrical Langmuir Probes in a Collisionless Maxwellian Plasma at Rest", UTIAS Rept. 100, March 1966, Univ. of Toronto, Toronto, Canada.
37. Smetana, F. O., "On the Current Collected by a Charged Circular Cylinder Immersed in a Two Dimensional Rarefied Plasma Stream", Third Symposium on Rarefied Gas Dynamics, edited by Laurmann, Paris, France, 1962, pp. 65-91.
38. Scharfman, W. E., "The Use of Langmuir Probes to Determine the Electron Density Surrounding Re-entry Vehicles", Final Rept. Contract NAS 1-3942, June 1965, Stanford Research Institute, Menlo Park, California.
39. Scharfman, W. E. and Bredfeldt, H. R., "Use of the Langmuir Probe to Determine the Electron Density and Temperature Surrounding Re-entry Vehicles", Final Rept. Contract NAS 1-4872, NASA 66275, Dec. 0966, Stanford Research Institute, Menlo Park, California.
40. Dunn, M. G., "Laboratory Measurements of Electron Density and Electron Temperature with RAM Flight Probes", Proceedings of the Symposium on the Entry Plasma Sheath and its Effects on Space Vehicle Electromagnetic Systems, NASA SP-252, Vol. 1, 1971, pp. 261-276.
41. Kang, S. W. and Dunn, M. G., "Hypersonic, Viscous Shock Layer with Chemical Nonequilibrium for Spherically Blunted Cones", Rept. AF-3093-A-1, Feb. 1972, Cornell Aeronautical Laboratory, Buffalo, New York.
42. Baird, A. W. and Lustig, C. D., "The Use of Electroacoustic Resonances to Determine Electron Density Profiles, " The Entry Plasma Sheath and Its Effects on Space Vehicle Electromagnetic Systems, National Aeronautics and Space Administration, Langley Research Center, Vol. 1, NASA SP-252, 1971.
43. Golden, K. E. and McPherson, D. A., "Analysis of VHF and X-Band Telemetry Systems Degradation by Reentry Environment," The Entry Plasma Sheath and Its Effects on Space Vehicle Electromagnetic Systems, National Aeronautics and Space Administration, Langley Research Center, Vol. 1, NASA SP-252, 1971.
44. Aisenberg, S. and Chang, K. W., "A Non-Protruding Conductivity Probe System for Re-entry Plasma Diagnostics," The Entry Plasma Sheath and Its Effects on Space Vehicle Electromagnetic Systems, National Aeronautics and Space Administration, Langley Research Center, Vol. 1, NASA SP-252, 1971.

45. Scott, L.D., Bhat, B., and Rao, B.R., "Investigations on a Cylindrical Antenna as a Diagnostic Probe for Isotropic and Magnetized Plasmas," The Entry Plasma Sheath and Its Effects on Space Vehicle Electromagnetic Systems, National Aeronautics and Space Administration, Langley Research Center, Vol. 1, NASA SP-252, 1971.
46. Swift, C.T., Beck, F.B., Thomson, J. and Castellow, S.L., "Ram C-III S-Band Diagnostic Experiment," The Entry Plasma Sheath and Its Effects on Space Vehicle Electromagnetic Systems, National Aeronautics and Space Administration, Langley Research Center, Vol. 1, NASA SP-252, 1971.
47. Tournyan, K.J. and Boyer, D.W., "Continuum Thick Sheath Probe Studies in Hypersonic Ionized Boundary Layers," U. of Japan, Symposium on Dynamics of Ionized Gases, Tokyo, Japan, 13-15 Sept. 1971.
48. Scharfman, W.E. and Bredfeldt, H.R., "Experimental Investigation of Flush-Mounted Electrostatic Probes," AIAA Journal, Vol. 8, No. 4, pp. 662, April 1970.
49. Bailey, M.C. and Swift, C.T., "Input Admittance of a Circular Waveguide Aperture Covered by a Dielectric Slab," IEEE Transactions on Antennas and Propagation, Vol. AP-16, No. 4, pp. 386-391, July 1968.
50. Taylor, W.C., "An Experimental Investigation of the Interaction of Plasmas with Antennas," NASA CR-1727, December 1970.
51. Croswell, W.F., Taylor, W.C., Swift, C.T., and Cockrell, C.R., "The Input Admittance of a Rectangular Waveguide Fed Aperture Under an Inhomogeneous Plasma: Theory and Experiment," Trans. Antenna and Propagation, AP-16, July 1968, pp. 475-484.
52. Dunn, M.G., "Electron-Density and Electron-Temperature Measurements in Boundary Layers," AIAA Journal, Vol. 9, No. 8, Aug. 1971, pp. 1561-1567.
53. Boyer, D.W., Tournyan, K.J. and Russo, A.J., "Experimental and Numerical Studies of Flush-Mounted Electrostatic Probes in Hypersonic Ionized Flows," AIAA 10th Aerospace Sciences Meeting, San Diego, California, Jan. 1972.
54. Sonin, A.A., "The Behavior of Free Molecular Cylindrical Langmuir Probes in Supersonic Flows, and their Application to the Study of the Blunt Body Stagnation Layer," Report 109, August 1965, Univ. of Toronto Institute for Aerospace Studies, Toronto, Canada.
55. Dunn, M.G., "Use of Positively Biased Langmuir Probes to Obtain Electron Density," to be published in AIAA Journal, 1972.

56. Burke, A.F., "Experimental Study of Electrical Currents to a Flat Plate in Supersonic Ionized Flow," SC-CR-67-2748, Sept. 1967, Sandia Corp., Albuquerque, New Mexico.
57. French, J.B., "Langmuir Probes in a Flowing Low Density Plasma," Rept. No. 79, Aug. 1961, Univ. of Toronto Institute for Aerospace Studies, Toronto, Canada.
58. Demetriades, A. and Doughman, E.L., "Langmuir Probe Diagnosis of Turbulent Plasmas," AIAA Journal, Vol. 4, No. 3, March 1966, pp. 451-459.
59. Sonin, A.A., "Free-Molecule Langmuir Probe and Its Use in Flow Field Studies," AIAA Journal, Vol. 4, No. 8, Sept. 1966, pp. 1588-1596.
60. Peterson, E.W. and Talbot, L., "Langmuir Probe Response in a Turbulent Plasma," AIAA Paper No. 69-698, San Francisco, Calif., June 1969.
61. Center, R.E., "Measurement of Electron Density Behind Shock Waves by Free-Molecular Langmuir Probes," Research Rept. 292, Dec. 1969, Avco Everett Research Laboratory, Everett, Mass.
62. Sutton, G.W., "Use of Langmuir Probes for Hypersonic Turbulent Wakes," AIAA Journal, Vol. 7, No. 2, Feb. 1969, pp. 193-199.
63. Jones, W.L., "Probe Measurements of Electron Density Profiles During a Blunt Body Reentry," Ph.D. Thesis, June 1971, Virginia Polytechnic Institute, Blacksburg, Virginia.
64. Dunn, M.G., "Experimental Study of High-Enthalpy Shock-Tunnel Flow: Part I. Shock-Tube Flow and Nozzle Starting Time," AIAA Journal, Vol. 7, No. 8, Aug. 1969, pp. 1553-1560.
65. Dunn, M.G., "Experimental Study of High-Enthalpy Shock Tunnel Flow: Part II. Nozzle-Flow Characteristics," AIAA Journal, Vol. 7, No. 9, Sept. 1969, pp. 1717-1723.
66. Dunn, M.G. and Lordi, J.A., "Thin-Wire Langmuir-Probe Measurements in the Transition and Free-Molecular Flow Regime," AIAA Journal, Vol. 8, No. 6, June 1970, pp. 1077-1081.
67. Dunn, M.G. and Lordi, J.A., "Measurement of Electron Temperature and Number Density in Shock-Tunnel Flows. Part I: Development of Free-Molecular Langmuir Probes," AIAA Journal, Vol. 7, No. 8, Aug. 1969, pp. 1458-1465.

68. Lordi, J.A., Vidal, R.J., and Johnson, C.B., "Chemical Nonequilibrium Effects on the Flow in the Windward Plane of Symmetry of a Blunted Delta Orbiter", NASA TM X-2506, Dec. 1971.
69. Kang, S.-W., Jones, W.L., and Dunn, M.G., "Theoretical and Measured Electron-Density Distributions for the RAM Vehicle at High Altitudes", to be presented at the AIAA 5th Fluid and Plasma Dynamics Conf., Boston, Mass., June 1972.
70. Davis, R.T., "Hypersonic Flow of a Chemically Reacting Binary Mixture past a Blunt Body", AIAA Paper 70-805, Los Angeles, California, 1970.
71. Lew, H.G., "The Ionized Flow Field over Reentry Bodies", Ge R67SD70, Dec. 1967, General Electric Space Sciences Lab., Valley Forge, Pa.
72. Kaplan, B., "The Nonequilibrium Air Boundary Layer on a Blunt Nosed Body", 68SD227, April 1968, General Electric Reentry Systems Department, Phila., Pa.
73. Bein, G.P., "Plane Wave Propagation at Arbitrary Angles of Incidence in Inhomogeneous, Lossy Plasmas and Prediction of Antenna Radiation Patterns", Cornell Aeronautical Laboratory Rept. No. ER/R15-8, Jan. 1966.
74. Back, L.H., "Conservation Equations of a Viscous, Heat-Conducting Fluid in Curvilinear Orthogonal Coordinates", Rept. TR 32-1332, Sept. 1968, NASA.
75. Bird, R.B., Stewart, W.E., and Lightfoot, E.N., Transport Phenomena, J. Wiley and Sons, New York (1960).
76. Lax, P.D., and Wendroff, B., "Difference Schemes with High Order of Accuracy for Solving Hyperbolic Equations" NYU Report 9759, Courant Inst. of Math. Sci., New York University (July 1962).
77. Moretti, G., and Salas, M.D., "The Blunt Body Problem for a Viscous Rarefied Gas Flow", AIAA Paper 69-139, New York, 1969.
78. Raetz, G.S., "A Method of Calculating Three-Dimensional Laminar Boundary Layers of Steady Compressible Flows", Northrop Corp. Rept. NAI-58-73 (BLC-114), Dec. 1957.
79. DuFort, E.C., and Frankel, S., "Stability Conditions in the Numerical Treatment of Parabolic Differential Equations", Mathematic Tables and other Aids to Computation, Vol. VII, No. 43 (July 1953).
80. Hall, M.G., "A Numerical Method for Calculating Steady Three-Dimensional Laminar Boundary Layers", Royal Aircraft Estab. Tech. Rept. 67145 (June 1967).

81. Kang, S. W., Rae, W. J., and Dunn, M. G., "Studies of Three-Dimensional Compressible Boundary Layers on Blunt Lifting Entry Bodies" Paper No. 28, Paper presented at the AGARD Specialists' Meeting on Hypersonic Boundary Layers and Flow Fields, London, England, (May 1968).
82. Dwyer, H. A., "Solution of a Three-Dimensional Boundary-Layer Flow with Separation", AIAA Journal, Vol. 6, No. 7 (July 1968), pp. 1336-1342.

Table I  
CHEMICAL REACTIONS AND RATE COEFFICIENTS USED  
IN NONEQUILIBRIUM CALCULATIONS

NO.	REACTION	FORWARD RATE COEFF, $k_F$	BACKWARD RATE COEFF, $k_B$	THIRD BODY, M
				FORWARD DIRECTION
		$\text{cm}^3/\text{mole sec}$	$\text{cm}^3/\text{mole sec OR } \text{cm}^6/\text{mole}^2 \text{ sec}$	
1	$\text{O}_2 + \text{M} \rightarrow 2\text{O} + \text{M}$	$3.6 \times 10^{18} T^{-1.0} \exp(-5.95 \times 10^4/T)$	$3.0 \times 10^{15} T^{-0.5}$	N, NO
2	$\text{N}_2 + \text{M} \rightarrow 2\text{N} + \text{M}$	$1.9 \times 10^{17} T^{-0.5} \exp(-1.13 \times 10^5/T)$	$1.1 \times 10^{16} T^{-0.5}$	O, NO, $\text{O}_2$
3	$\text{NO} + \text{M} \rightarrow \text{N} + \text{O} + \text{M}$	$3.9 \times 10^{20} T^{-1.5} \exp(-7.55 \times 10^4/T)$	$1.0 \times 10^{20} T^{-1.5}$	$\text{O}_2, \text{N}_2$
4	$\text{O} + \text{NO} \rightarrow \text{N} + \text{O}_2$	$3.2 \times 10^9 T^1 \exp(-1.97 \times 10^4/T)$	$1.3 \times 10^{10} T^{1.0} \exp(-3.58 \times 10^3/T)$	
5	$\text{O} + \text{N}_2 \rightarrow \text{N} + \text{NO}$	$7.0 \times 10^{13} \exp(-3.8 \times 10^4/T)$	$1.56 \times 10^{13}$	
6	$\text{N} + \text{N}_2 \rightarrow \text{N} + \text{N} + \text{N}$	$4.085 \times 10^{22} T^{-1.5} \exp(-1.13 \times 10^5/T)$	$2.27 \times 10^{21} T^{-1.5}$	
7	$\text{O} + \text{N} \rightarrow \text{NO}^+ + \text{e}^-$	$(1.4 \pm 0.4) \times 10^6 T^{1.5} \exp(-3.19 \times 10^4/T)$	$(6.7 \pm 2.3) \times 10^{21} T^{-1.5}$	
8	$\text{O} + \text{e}^- \rightarrow \text{O}^+ + \text{e}^- + \text{e}^-$	$(3.6 \pm 1.2) \times 10^{31} T^{-2.91} \exp(-1.58 \times 10^5/T)$	$(2.2 \pm 0.7) \times 10^{40} T^{-4.5}$	
9	$\text{N} + \text{e}^- \rightarrow \text{N}^+ + \text{e}^- + \text{e}^-$	$(1.1 \pm 0.4) \times 10^{32} T^{-3.14} \exp(-1.69 \times 10^5/T)$	$(2.2 \pm 0.7) \times 10^{40} T^{-4.5}$	
10	$\text{O} + \text{O} \rightarrow \text{O}_2^+ + \text{e}^-$	$(1.6 \pm 0.4) \times 10^{17} T^{-0.98} \exp(-8.08 \times 10^4/T)$	$(8.0 \pm 2.0) \times 10^{21} T^{-1.5}$	
11	$\text{O} + \text{O}_2^+ \rightarrow \text{O}_2 + \text{O}^+$	$2.92 \times 10^{18} T^{-1.11} \exp(-2.8 \times 10^4/T)$	$7.8 \times 10^{11} T^{0.5}$	
12	$\text{N}_2 + \text{N}^+ \rightarrow \text{N} + \text{N}_2^+$	$2.02 \times 10^{11} T^{0.81} \exp(-1.3 \times 10^4/T)$	$7.8 \times 10^{11} T^{0.5}$	
13	$\text{N} + \text{N} \rightarrow \text{N}_2^+ + \text{e}^-$	$(1.4 \pm 0.3) \times 10^{13} \exp(-6.78 \times 10^4/T)$	$(1.5 \pm 0.5) \times 10^{22} T^{-1.5}$	
14	$\text{O}_2 + \text{N}_2 \rightarrow \text{NO} + \text{NO}^+ + \text{e}^-$	$1.38 \times 10^{20} T^{-1.84} \exp(-1.41 \times 10^5/T)$	$1.0 \times 10^{24} T^{-2.5}$	
15	$\text{NO} + \text{N}_2 \rightarrow \text{NO}^+ + \text{e}^- + \text{N}_2$	$2.2 \times 10^{15} T^{-0.35} \exp(-1.08 \times 10^5/T)$	$2.2 \times 10^{26} T^{-2.5}$	
16	$\text{O} + \text{NO}^+ \rightarrow \text{NO} + \text{O}^+$	$3.63 \times 10^{15} T^{-0.6} \exp(-5.08 \times 10^4/T)$	$1.5 \times 10^{13}$	
17	$\text{N}_2 + \text{O}^+ \rightarrow \text{O} + \text{N}_2^+$	$3.4 \times 10^{19} T^{-2.0} \exp(-2.3 \times 10^4/T)$	$2.48 \times 10^{19} T^{-2.2}$	
18	$\text{N} + \text{NO}^+ \rightarrow \text{NO} + \text{N}^+$	$1.0 \times 10^{19} T^{-0.93} \exp(-6.1 \times 10^4/T)$	$4.8 \times 10^{14}$	
19	$\text{O}_2 + \text{NO}^+ \rightarrow \text{NO} + \text{O}_2^+$	$1.8 \times 10^{15} T^{0.17} \exp(-3.3 \times 10^4/T)$	$1.8 \times 10^{13} T^{0.5}$	
20	$\text{O} + \text{NO}^+ \rightarrow \text{O}_2 + \text{N}^+$	$1.34 \times 10^{13} T^{0.31} \exp(-7.727 \times 10^4/T)$	$1.0 \times 10^{14}$	
21	$\text{NO} + \text{O}_2 \rightarrow \text{NO}^+ + \text{e}^- + \text{O}_2$	$8.8 \times 10^{15} T^{-0.35} \exp(-1.08 \times 10^5/T)$	$8.8 \times 10^{26} T^{-2.5}$	
22	$\text{O}_2 + \text{O} \rightarrow 2\text{O} + \text{O}$	$9.0 \times 10^{19} T^{-1.0} \exp(-5.95 \times 10^4/T)$	$7.5 \times 10^{16} T^{-0.5}$	
23	$\text{O}_2 + \text{O}_2 \rightarrow 2\text{O} + \text{O}_2$	$3.24 \times 10^{19} T^{-1.0} \exp(-5.95 \times 10^4/T)$	$2.7 \times 10^{16} T^{-0.5}$	
24	$\text{O}_2 + \text{N}_2 \rightarrow 2\text{O} + \text{N}_2$	$7.2 \times 10^{18} T^{-1.0} \exp(-5.95 \times 10^4/T)$	$6.0 \times 10^{15} T^{-0.5}$	
25	$\text{N}_2 + \text{N}_2 \rightarrow 2\text{N} + \text{N}_2$	$4.7 \times 10^{17} T^{-0.5} \exp(-1.13 \times 10^5/T)$	$2.72 \times 10^{16} T^{-0.5}$	
26	$\text{NO} + \text{M} \rightarrow \text{N} + \text{O} + \text{M}$	$7.8 \times 10^{20} T^{-1.5} \exp(-7.55 \times 10^4/T)$	$2.0 \times 10^{20} T^{-1.5}$	O, N, NO

Table II

**SUMMARY OF EXPERIMENTAL RESULTS OBTAINED WITH RAM C-III S-BAND ANTENNA  
AT 6.75 INCHES FROM PLATE LEADING EDGE IN CARBON MONOXIDE PLASMA**

RUN #	PEAK $n_e$ OVER ANTENNA $e^-/cm^3$	$n_e/n_e$ )CR	ANTENNA IN FREE SPACE BEFORE PLASMA					ANTENNA IN FREE SPACE ROTATED & CORRECTED FOR LINE LOSS		ANTENNA WITH PLASMA OVER APERTURE					ANTENNA WITH PLASMA ROTATED & CORRECTED FOR LINE LOSS	
			#1 ARC	#2 ARC	#3 ARC	#4 ARC	REFL. ARC			#1 ARC	#2 ARC	#3 ARC	#4 ARC	REFL. ARC		
			Y	Γ												
<b>FOIL UNDER PLEXIGLAS</b>																
15	(6.3 TO 5.3) $\times 10^{11}$	4.2 ± .3	1.872	1.08	0.342	1.58	0.90			0.476	1.472	1.764	1.070	0.76	0.072 + j 0.05	0.862
16	(7.6 TO 6.4) $\times 10^{11}$	5.0 ± .4	0.728	1.164	1.32	0.952	0.325	0.47 - 0.001	0.36	0.610	1.570	1.74	0.956	0.772	0.077 - j 0.09	0.860
	*(5.4 TO 4.8) $\times 10^{11}$	3.6 ± .3								0.464	1.476	1.716	0.896	0.762	0.092 - j 0.038	0.830
17	*(4.0 TO 3.4) $\times 10^{11}$	2.6 ± .2	0.734	1.144	1.306	0.956	0.31	0.49 + j 0.005	0.342	0.376	1.404	1.816	1.230	0.80	0.060 + j 0.085	0.890
	(3.6 TO 3.0) $\times 10^{11}$	2.4 ± .2								0.324	1.304	1.780	1.290	0.792	0.065 + j 0.147	0.880
	*(4.0 TO 3.4) $\times 10^{11}$	2.6 ± .2								0.276	1.396	1.764	1.142	0.792	0.063 + j 0.06	0.880
18	(8.2 TO 7.0) $\times 10^{11}$	5.4 ± .45	0.722	1.12	1.284	0.944	0.302	0.50 + j 0.025	0.33	0.590	1.520	1.720	0.974	0.760	0.085 - j 0.075	0.845
19	(1.3 TO 1.2) $\times 10^{11}$	0.9 ± .15	0.704	1.136	1.314	0.958	0.320	0.48 + j 0.03	0.35	0.514	1.040	1.674	1.444	0.710	0.14 + j 0.418	0.790
	*(1.05 TO 1.0) $\times 10^{11}$	0.74 ± .12								0.682	0.878	1.444	1.380	0.525	0.34 + j 0.49	0.582
20	(9.0 TO 7.5) $\times 10^{10}$	0.6 ± .1	0.704	1.136	1.310	0.96	0.318	0.48 + j 0.03	0.35	0.796	1.020	1.240	1.056	0.249	0.625 + j 0.15	0.25

NOTE: 1) THE VOLTAGE REFLECTION COEFFICIENT, |Γ|, GIVEN HERE HAS BEEN CORRECTED FOR LINE LOSS. TO GET THE UNCORRECTED VALUE, MULTIPLY BY 0.90.

2) \* INDICATES POST TEST-TIME DATA AND † INDICATES PRE TEST-TIME DATA.

Table III

**SUMMARY OF EXPERIMENTAL RESULTS OBTAINED WITH RAM C-II S-BAND ANTENNA  
AT 11.25 INCHES FROM PLATE LEADING EDGE IN CARBON MONOXIDE PLASMA**

RUN #	PEAK ELECTRON DENSITY OVER ANTENNA $n_e$ $e^3/cm^3$	$n_e/n_{e,CR}$	ANTENNA IN FREE SPACE BEFORE PLASMA ARRIVAL					ANTENNA IN FREE SPACE ROTATED AND CORRECTED FOR LINE LOSS		ANTENNA WITH PLASMA OVER APERTURE					ANTENNA WITH PLASMA ROTATED AND CORRECTED FOR LINE LOSS	
			#1 ARC	#2 ARC	#3 ARC	#4 ARC	REFL. ARC	Y	$ \Gamma $	#1 ARC	#2 ARC	#3 ARC	#4 ARC	REFL. ARC	Y	$ \Gamma $
<b>SHORT OVER ANTENNA APERTURE</b>																
1	$(2.46 \pm .24) \times 10^{11}$	$1.76 \pm .17$	0.95	0.89	1.07	1.12	0.148	$1.35 + j 0.19$	0.17	1.376	1.498	0.916	0.630	0.565	$0.205 - j 0.246$	0.68
2	$(2.87 \pm .28) \times 10^{11}$	$2.05 \pm .20$	0.96	0.864	1.078	1.14	0.148	$1.38 + j 0.18$	0.18	1.522	1.396	0.670	0.842	0.630	$0.22 - j 0.470$	0.705
3	$(1.46 \pm .13) \times 10^{11}$	$1.04 \pm .09$	0.964	0.874	1.078	1.152	0.140	$1.39 + j 0.19$	0.18	0.722	1.516	1.572	0.774	0.600	$0.17 + j 0.450$	0.760
4	$(1.60 \pm .12) \times 10^{11}$	$1.14 \pm .09$	0.976	0.890	1.086	0.144	0.131	$1.36 + j 0.18$	0.165	1.136	1.620	1.200	0.434	0.58	$0.175 + j 0.04$	0.710
*	$(1.13 \pm .09) \times 10^{11}$	$0.81 \pm .06$	0.976	0.890	1.086	0.144	0.131	$1.36 + j 0.18$	0.165	0.58	1.124	1.550	1.176	0.515	$0.49 + j 0.97$	0.617
5	$(1.60 \pm .12) \times 10^{11}$	$1.14 \pm .09$	0.970	0.862	1.050	1.134	0.130	$1.38 + j 0.12$	0.165	1.196	1.550	1.170	0.476	0.56	$0.21 - j 0.016$	0.652
*	$(1.03 \pm .05) \times 10^{11}$	$0.73 \pm .03$	0.970	0.862	1.050	1.134	0.130	$1.38 + j 0.12$	0.165	0.88	0.854	1.240	1.230	0.360	$1.72 + j 0.85$	0.39
6	$(4.07 \pm .73) \times 10^{10}$	$0.29 \pm .05$	0.976	0.876	1.050	1.140	0.122	$1.38 + j 0.10$	0.165	0.976	0.876	1.050	1.140	0.122	$1.38 + j 0.10$	0.165
7	$(3.11 \pm .3) \times 10^{10}$	$0.22 \pm .02$	0.944	0.876	1.064	1.122	0.140	$1.33 + j 0.24$	0.18	0.996	0.904	1.090	1.120	0.140	$1.30 + j 0.13$	0.145
8	$(4.29 \pm .51) \times 10^{10}$	$0.31 \pm .03$	0.944	0.861	1.058	1.122	0.145	$1.38 + j 0.18$	0.175	0.944	0.861	1.058	1.122	0.145	$1.38 + j 0.18$	0.175
9	$(7.48 \pm .82) \times 10^{10}$	$0.53 \pm .06$	0.944	0.864	1.050	1.122	0.143	$1.36 + j 0.17$	0.17	0.830	0.900	1.232	1.160	0.280	$1.19 + j 0.70$	0.315
*	$(6.62 \pm .72) \times 10^{10}$	$0.47 \pm .05$	0.944	0.864	1.050	1.122	0.143	$1.36 + j 0.17$	0.17	0.856	0.762	1.110	1.240	0.305	$1.70 + j 0.65$	0.341
10	$(7.68 \pm .73) \times 10^{10}$	$0.55 \pm .05$	0.976	0.876	1.050	1.136	0.142	$1.38 + j 0.10$	0.165	0.856	0.840	1.312	1.296	0.415	$1.51 + j 0.95$	0.40
11	$(1.30 \pm .12) \times 10^{11}$	$0.93 \pm .08$	0.966	0.836	1.038	1.136	0.141	$1.43 + j 0.10$	0.182	0.57	1.336	1.562	0.952	0.560	$0.26 + j 0.67$	0.70

NOTE: 1) THE VOLTAGE REFLECTION COEFFICIENT,  $|\Gamma|$ , GIVEN HERE HAS BEEN CORRECTED FOR LINE LOSS TO GET THE UNCORRECTED VALUE, MULTIPLY BY 0.835.

2) ANTENNA FREQUENCY WAS 3348 MHz AND THEREFORE  $n_e/CR \cong 1.4 \cdot 10^{11} e^3/cm^3$

3) \* INDICATES POST TEST-TIME DATA

Table IV  
RESULTS OBTAINED FROM LANGMUIR PROBE CURRENT-VOLTAGE CHARACTERISTICS

TEST GAS	PROBE LOCATION	$\mu$ -WAVE NUMBER DENSITY AT 22.5 in. $e^-/cm^3$	NUMBER DENSITY FROM ION SATURATION $e^-/cm^3$	$R_p/\lambda_D$	$T_e$ °K	NUMBER DENSITY FROM ELECTRON SATURATION $e^-/cm^3$	$R_p/\lambda_D$	$(V_\infty - V_f)$ theo. volts	$(V_\infty - V_f)$ exp. volts
CO	FREE STREAM	$2.0 \times 10^{11}$	$1.5 \times 10^{11}$	7.5	2110	$1.3 \times 10^{11}$	6.9	0.9	0.8
CO		$1.5 \times 10^{11}$	$1.7 \times 10^{11}$	8.8	1650	$1.7 \times 10^{11}$	8.7	0.7	0.9
CO		$2.0 \times 10^{11}$	$1.2 \times 10^{11}$	7.0	1945	$1.4 \times 10^{11}$	7.4	0.85	0.8
CO	↓ BOUNDARY LAYER		$1.4 \times 10^{10}$	1.7	2500	$1.3 \times 10^{10}$	1.7	1.2	1.2
CO			$1.3 \times 10^{10}$	1.9	2090	$1.3 \times 10^{10}$	1.8	0.9	1.1
CO			$1.7 \times 10^{10}$	2.0	2320	$1.4 \times 10^{10}$	1.4	1.0	1.1
CO			$4.4 \times 10^{10}$	3.3	2300	$3.3 \times 10^{10}$	2.8	1.0	1.2
CO			$1.6 \times 10^{10}$	1.9	2510	$1.4 \times 10^{10}$	1.8	1.1	0.9
CO			$6.6 \times 10^{10}$	4.3	2000	$5.3 \times 10^{10}$	3.8	0.9	0.9
CO			$1.1 \times 10^{10}$	1.6	2170	$1.1 \times 10^{10}$	1.7	0.95	0.9
CO			$5.3 \times 10^{10}$	3.5	2310	$5.0 \times 10^{10}$	3.4	1.0	1.2
CO			$1.8 \times 10^{10}$	2.3	1810	$1.8 \times 10^{10}$	2.3	0.8	0.8
CO			$6.2 \times 10^{10}$	4.4	1730	$6.5 \times 10^{10}$	3.6	0.76	0.8
CO			$2.1 \times 10^{10}$	2.3	2100	$2.1 \times 10^{10}$	2.3	0.92	1.0
CO			$4.1 \times 10^{10}$	3.4	1950	$4.1 \times 10^{10}$	3.4	0.85	0.9
CO			$8.1 \times 10^9$	1.5	1955	$8.9 \times 10^9$	1.6	0.86	0.8
CO			$5.0 \times 10^{10}$	3.9	1960	$4.6 \times 10^{10}$	3.6	0.86	0.9
CO			$2.5 \times 10^{10}$	2.5	2130	$2.6 \times 10^{10}$	2.5	0.93	1.1
CO			$9.4 \times 10^9$	1.6	2020	$9.2 \times 10^9$	1.6	0.88	0.8
CO			$2.7 \times 10^{10}$	2.7	2060	$2.9 \times 10^{10}$	2.8	0.90	1.0
CO			$1.2 \times 10^{10}$	1.7	2160	$1.3 \times 10^{10}$	1.8	0.93	0.9
CO			$2.8 \times 10^{10}$	2.8	1980	$3.8 \times 10^{10}$	3.2	0.87	1.0
CO			$6.8 \times 10^9$	1.3	2160	$6.5 \times 10^9$	1.3	0.95	1.1
CO			$4.3 \times 10^{10}$	3.5	1915	$4.3 \times 10^{10}$	1.4	0.84	1.0
N <sub>2</sub>	FREE STREAM	$9.5 \times 10^9$	$9.0 \times 10^9$	1.4	3580	$1.1 \times 10^{10}$	1.5	1.6	2.0
N <sub>2</sub>		$1.0 \times 10^{10}$	$1.1 \times 10^{10}$	1.5	3670	$1.1 \times 10^{10}$	1.5	1.6	1.6
N <sub>2</sub>		$1.5 \times 10^{10}$	$1.4 \times 10^{10}$	1.7	3510	$1.1 \times 10^{10}$	1.5	1.53	1.5
N <sub>2</sub>		$7.2 \times 10^9$	$7.4 \times 10^9$	1.5	2450	$3.5 \times 10^9$	2.1	1.06	0.7

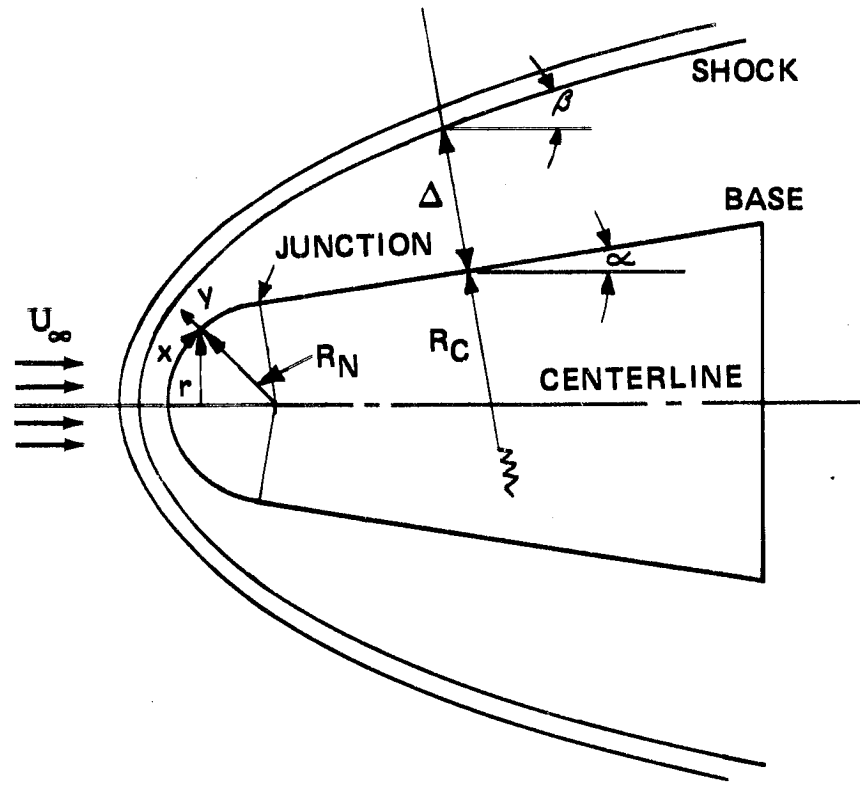


Figure 1 SCHEMATIC FLOW FIELD

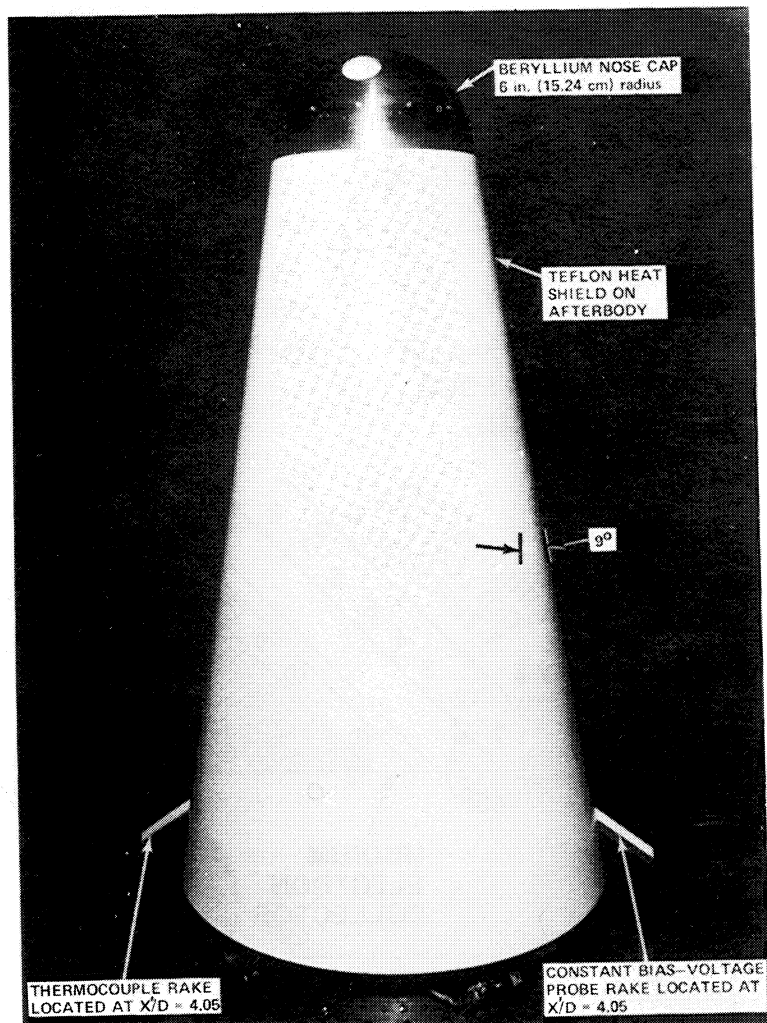
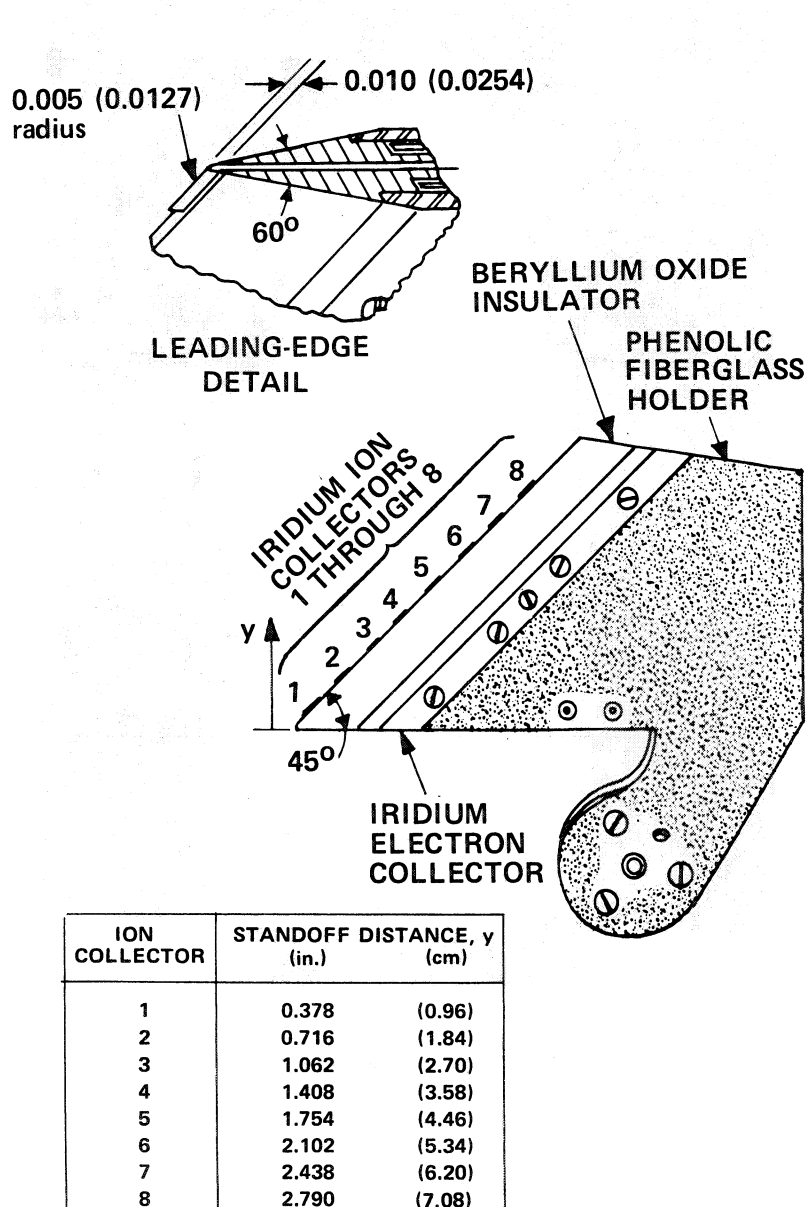


Figure 2 RAM C-II PAYLOAD EXTERNAL CONFIGURATION



**Figure 3 RAM C-II CONSTANT BIAS-VOLTAGE ELECTROSTATIC PROBE RAKE**

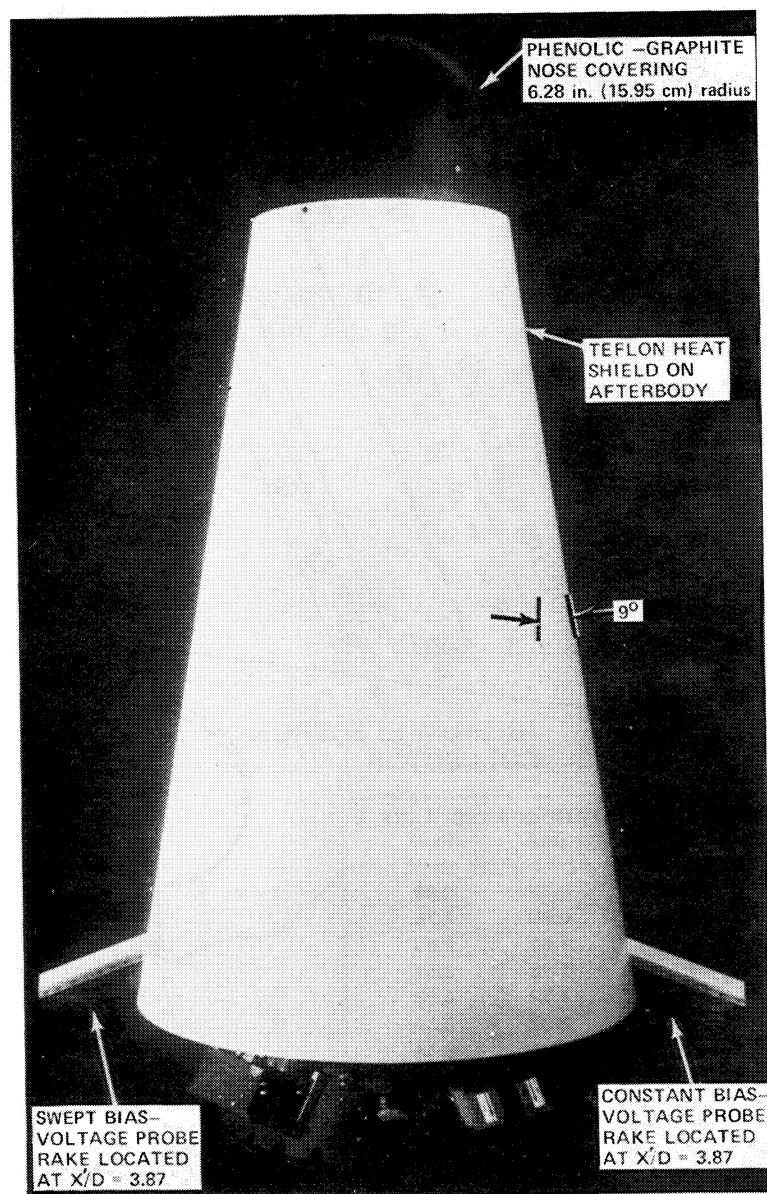


Figure 4 RAM C-III PAYLOAD EXTERNAL CONFIGURATION

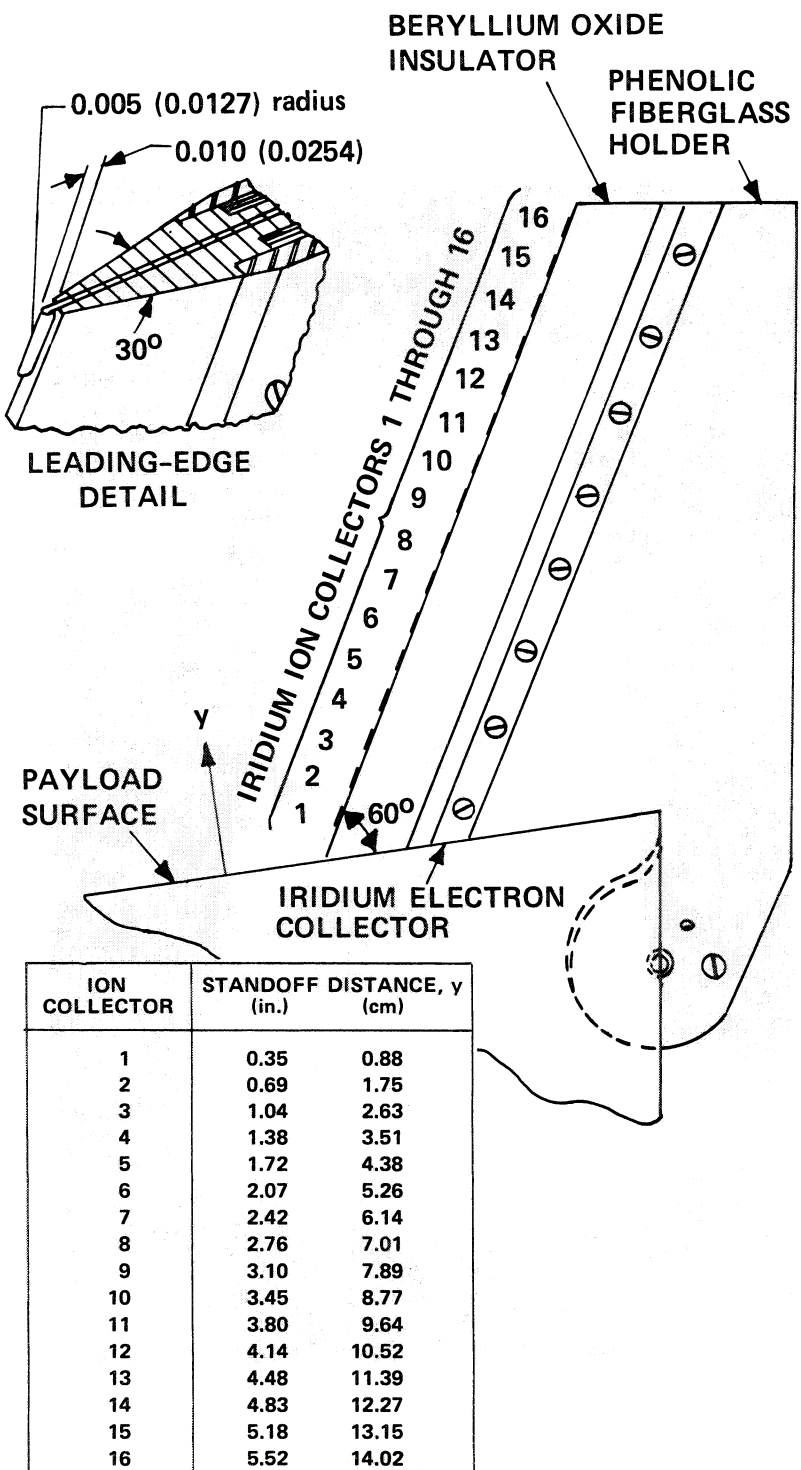


Figure 5 RAM C-III CONSTANT BIAS-VOLTAGE ELECTROSTATIC PROBE RAKE

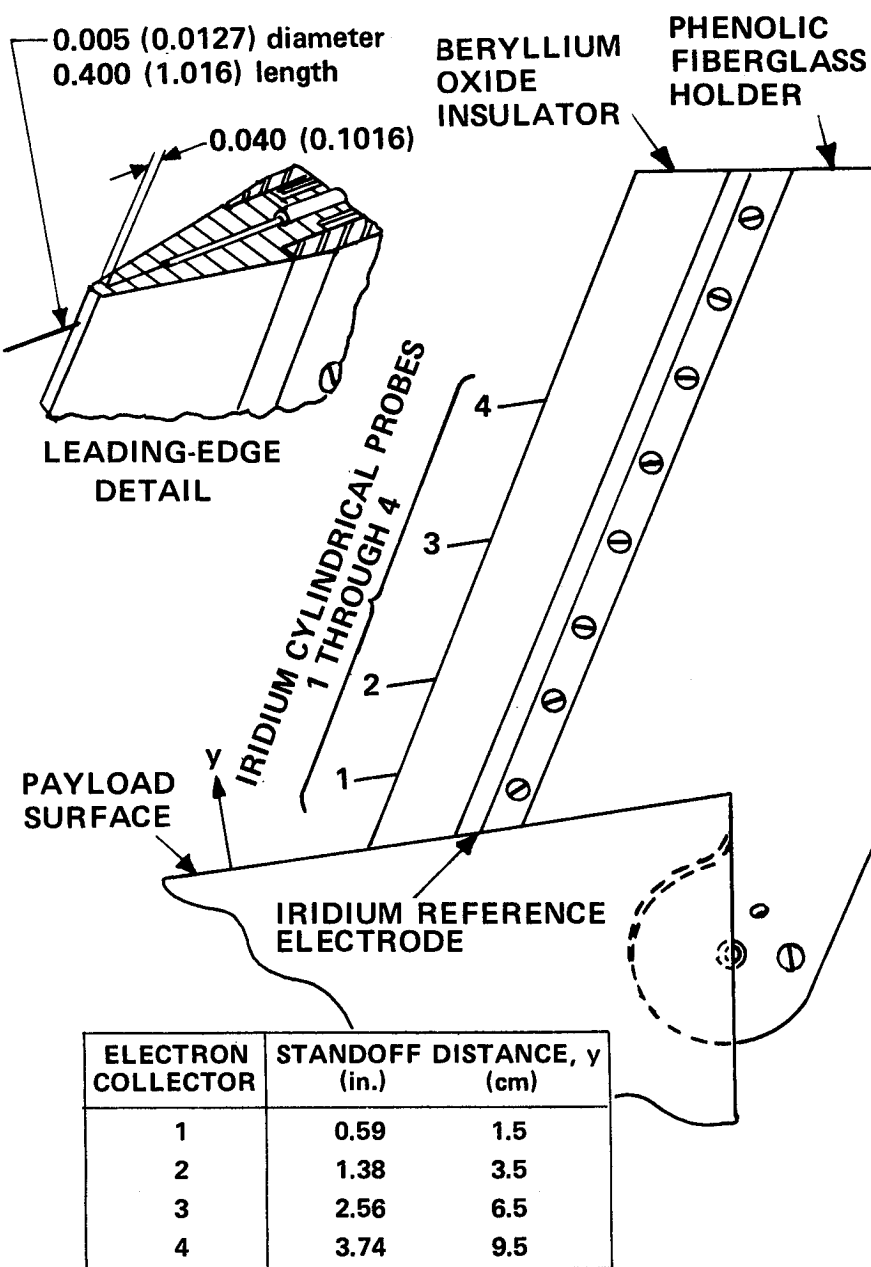
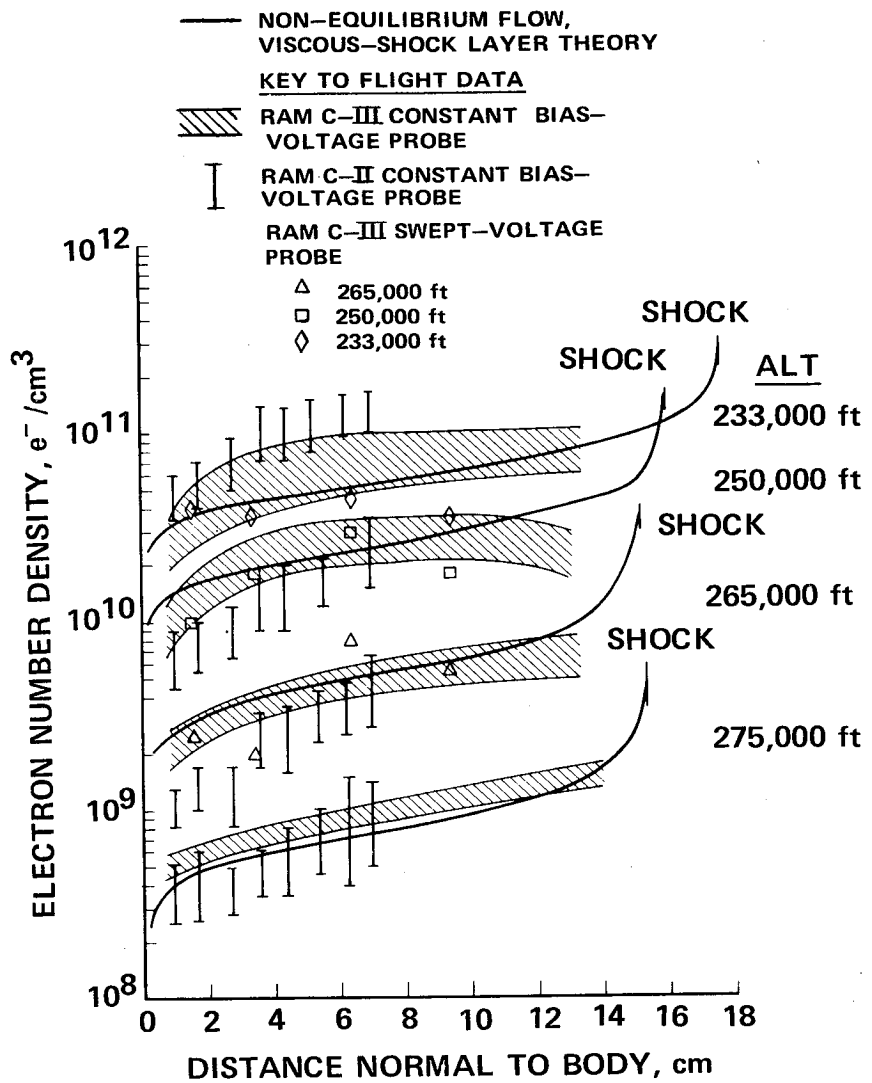
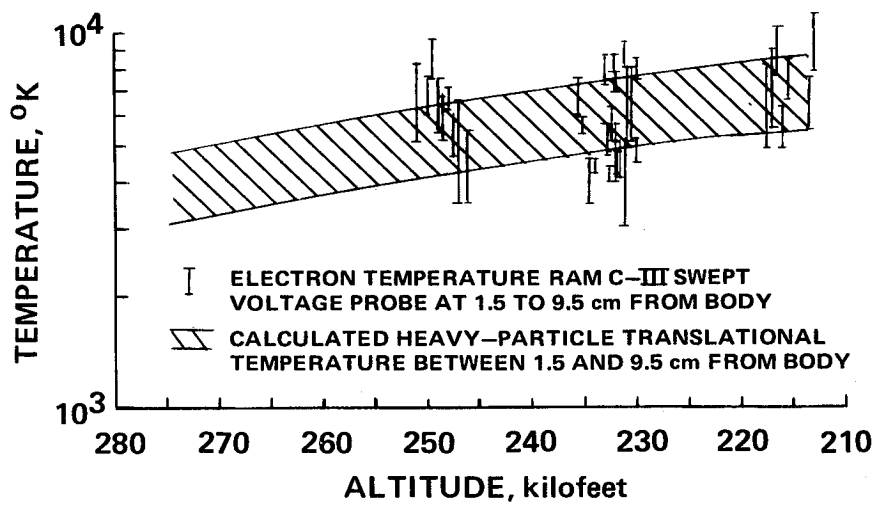


Figure 6 RAM C-III SWEPT-VOLTAGE ELECTROSTATIC PROBE RAKE



**Figure 7 COMPARISON BETWEEN CALCULATED ELECTRON DENSITY AND IN-FLIGHT ELECTROSTATIC PROBE MEASUREMENTS**



**Figure 8 COMPARISON BETWEEN CALCULATED HEAVY-PARTICLE TRANSLATIONAL TEMPERATURE AND IN-FLIGHT MEASURED ELECTRON TEMPERATURE**

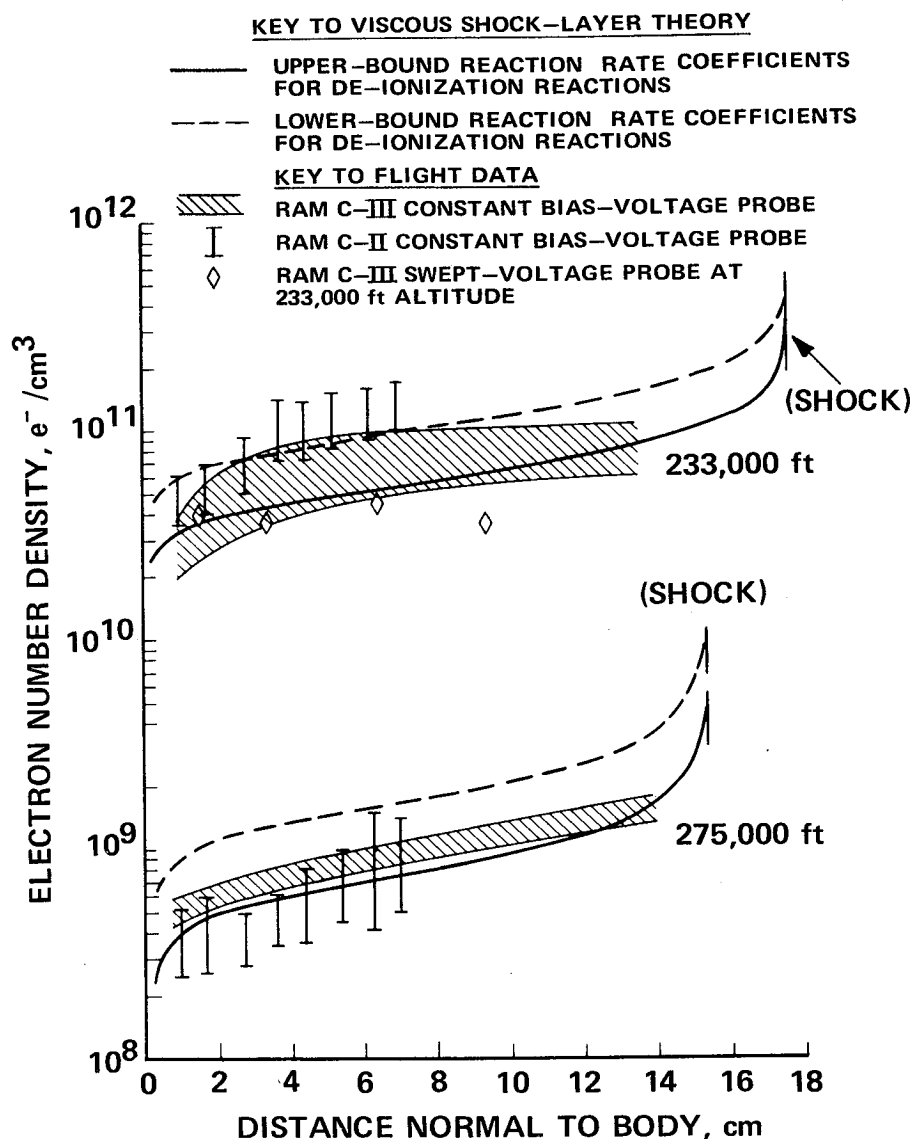


**Figure 9 INFLUENCE OF REACTION RATE COEFFICIENTS ON CALCULATED ELECTRON DENSITY AT ELECTROSTATIC PROBE LOCATION**

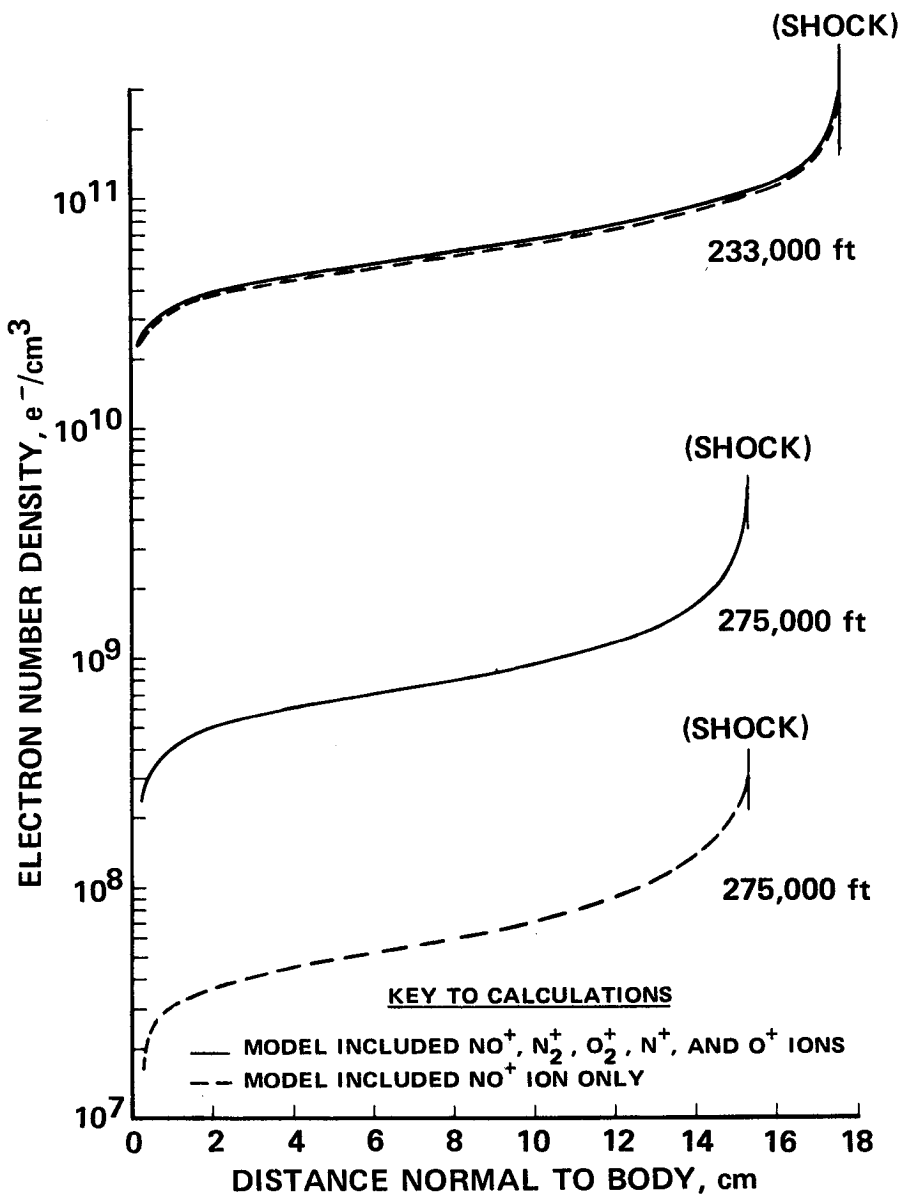


**Figure 10 INFLUENCE OF CHEMICAL MODEL ON CALCULATED ELECTRON DENSITY AT ELECTROSTATIC PROBE LOCATION**

NOTE: RESULTS ARE FOR UPPER-BOUND  
REACTION RATE COEFFICIENTS  
FOR DE-IONIZATION REACTIONS

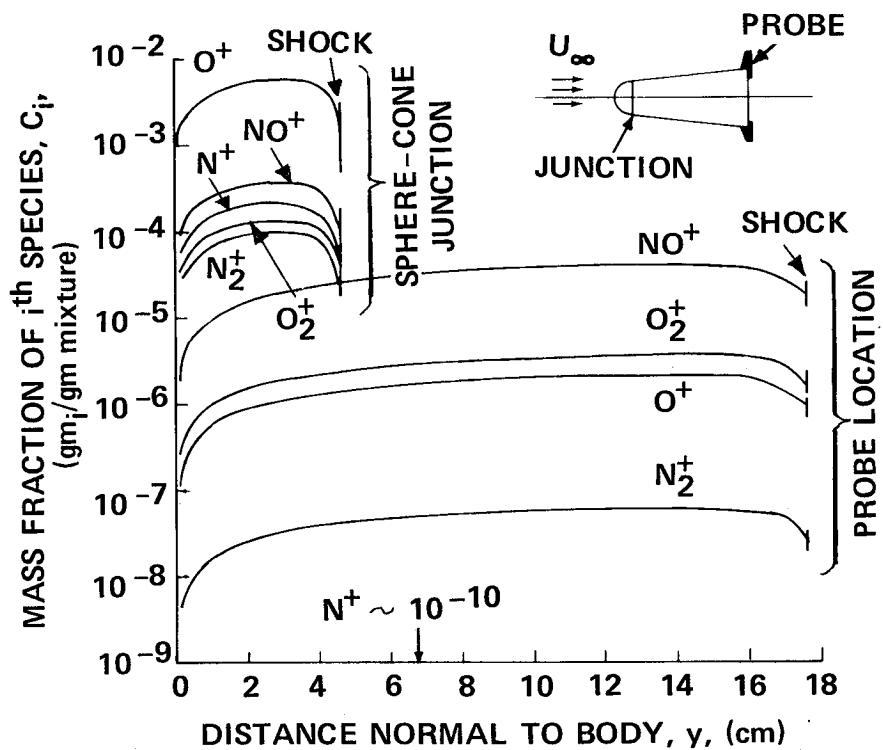


Figure 11 NONEQUILIBRIUM SPECIES DISTRIBUTIONS IN PLASMA LAYER FOR 233,000 ft ALTITUDE AT 25,000 ft/sec VELOCITY

NOTE: RESULTS ARE FOR UPPER-BOUND  
REACTION RATE COEFFICIENTS  
FOR DE-IONIZATION REACTIONS

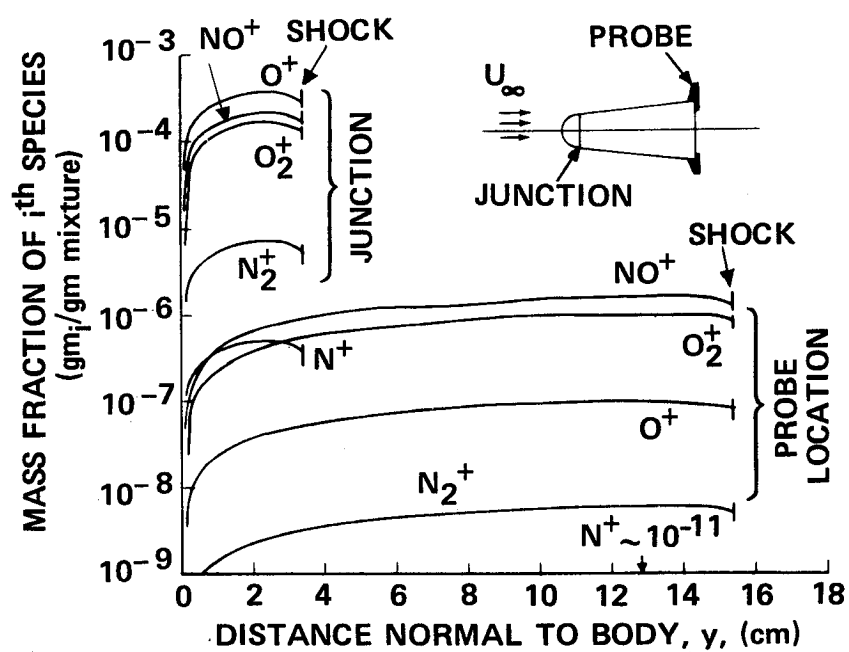


Figure 12 NONEQUILIBRIUM SPECIES DISTRIBUTIONS IN PLASMA LAYER FOR 275,000 ft ALTITUDE AT 25,000 ft/sec VELOCITY

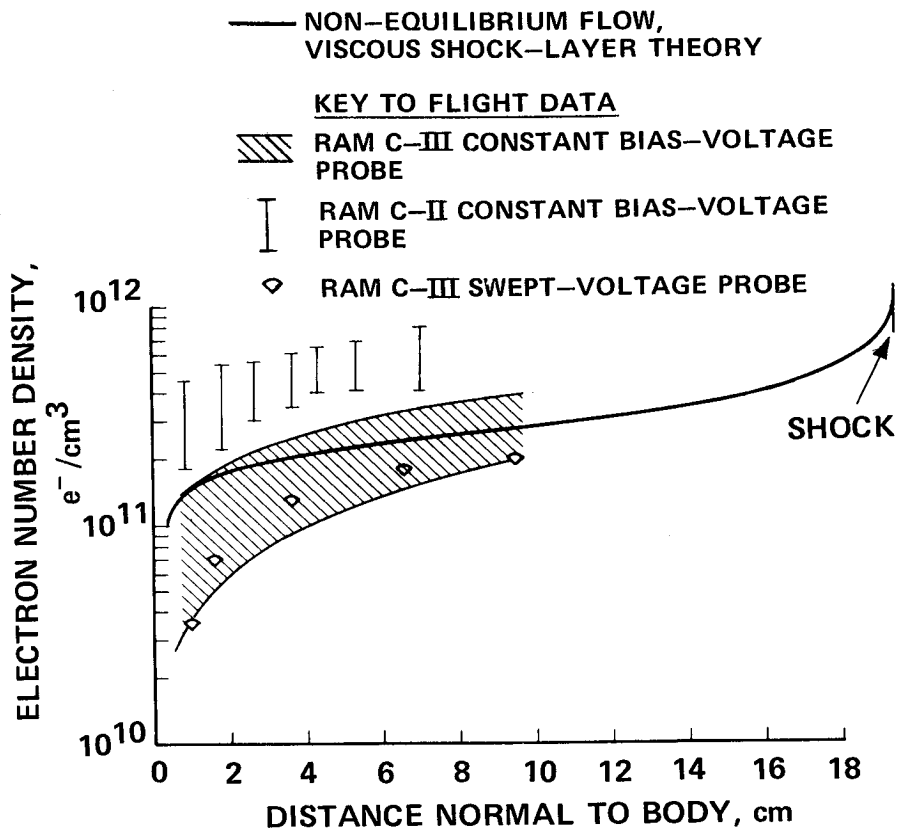
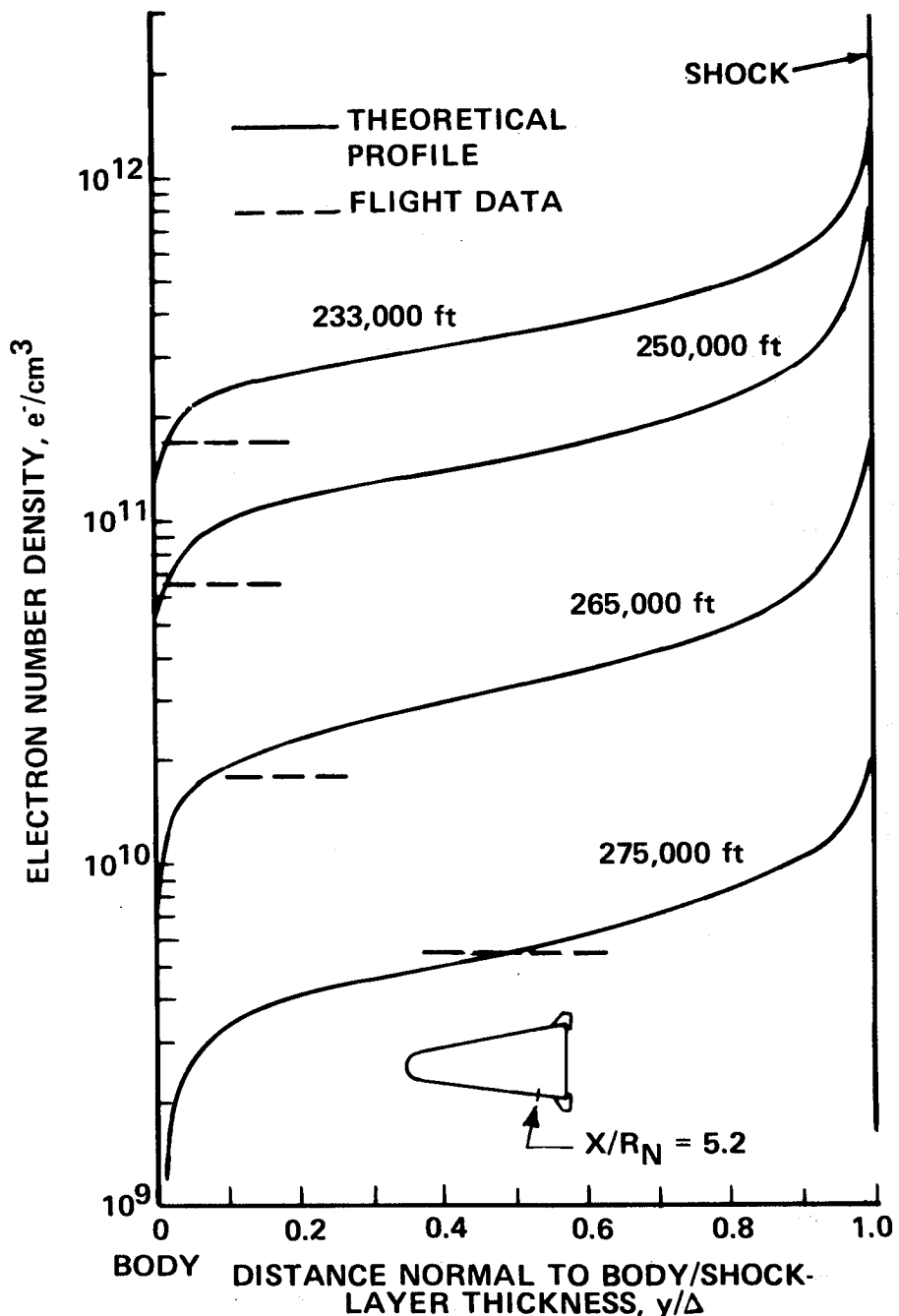


Figure 13 COMPARISON BETWEEN CALCULATED ELECTRON DENSITY AND IN-FLIGHT ELECTROSTATIC PROBE MEASUREMENTS AT 214,000 ft ALTITUDE



**Figure 14** COMPARISON OF PREDICTED  
 ELECTRON DENSITY PROFILE  
 WITH PEAK VALUE FROM  
 REFLECTOMETER FLIGHT  
 DATA AT  $X/R_N = 5.2$

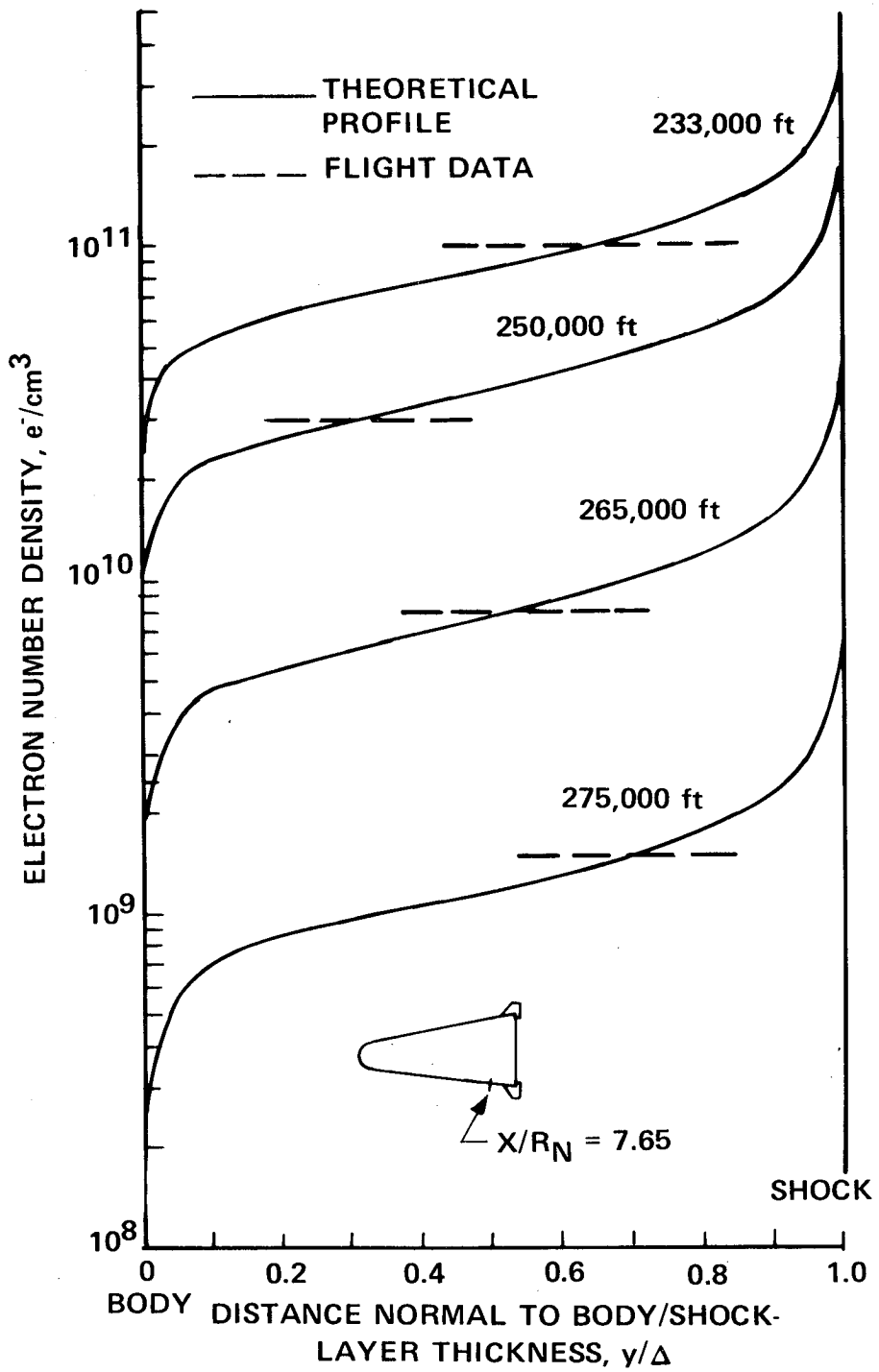


Figure 15 COMPARISON OF PREDICTED ELECTRON-DENSITY PROFILE WITH PEAK VALUE FROM REFLECTOMETER FLIGHT DATA AT  $X/R_N = 7.65$

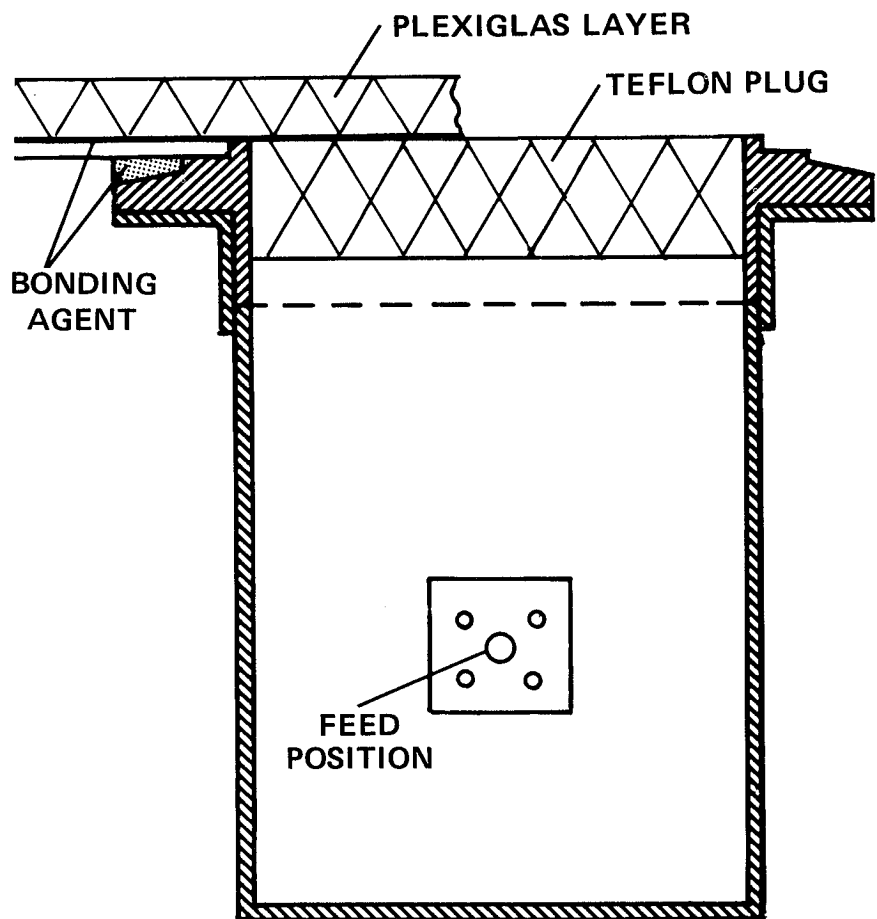
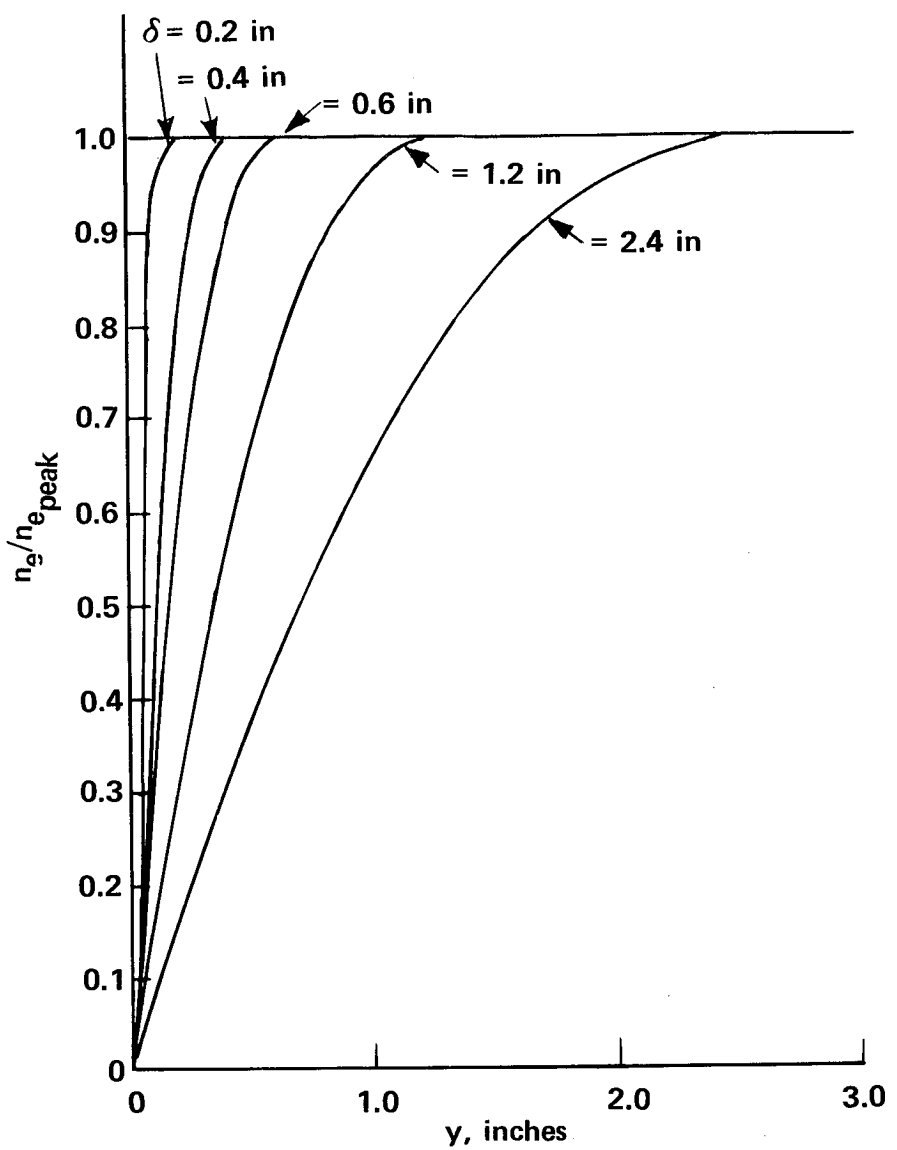
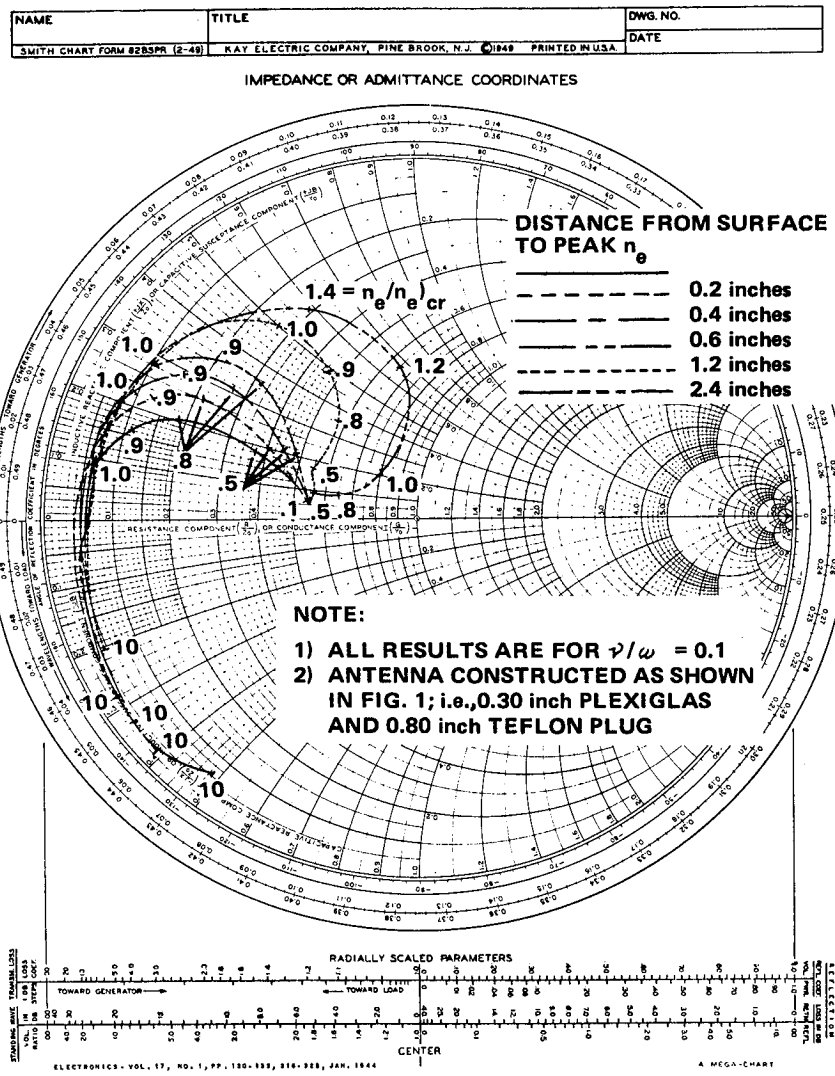


Figure 16 SKETCH OF THE RAM C-III S-BAND ANTENNA



**Figure 17 ASSUMED ELECTRON-DENSITY PROFILES FOR PRE-EXPERIMENT CALCULATIONS**



**Figure 18 INFLUENCE OF BOUNDARY LAYER ELECTRON – DENSITY PROFILE ON CALCULATED ADMITTANCE**

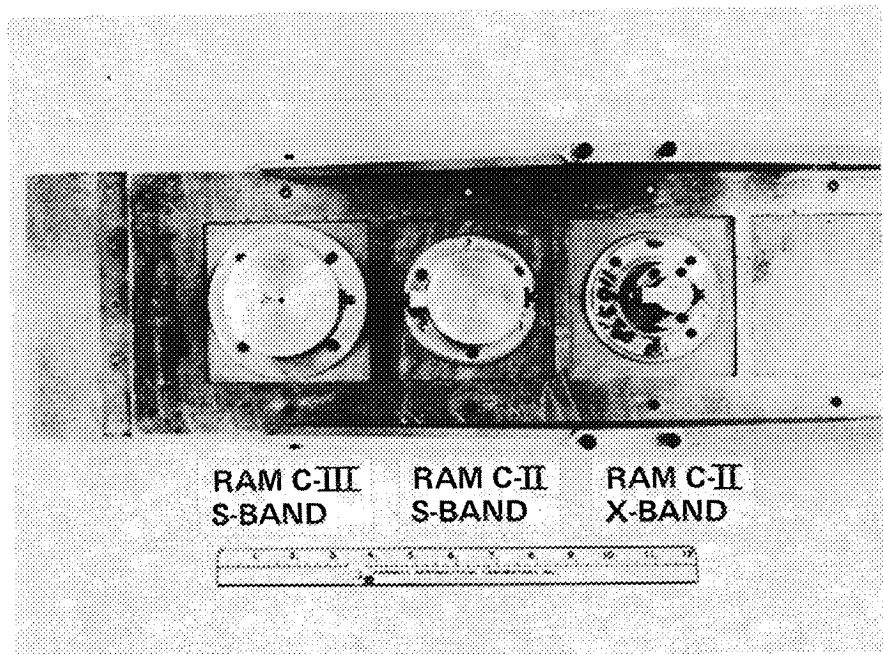


**Figure 19(a)RAM C-III AND RAM C-II S-BAND  
AND X-BAND ANTENNAS MOUNTED  
IN FLAT PLATE**

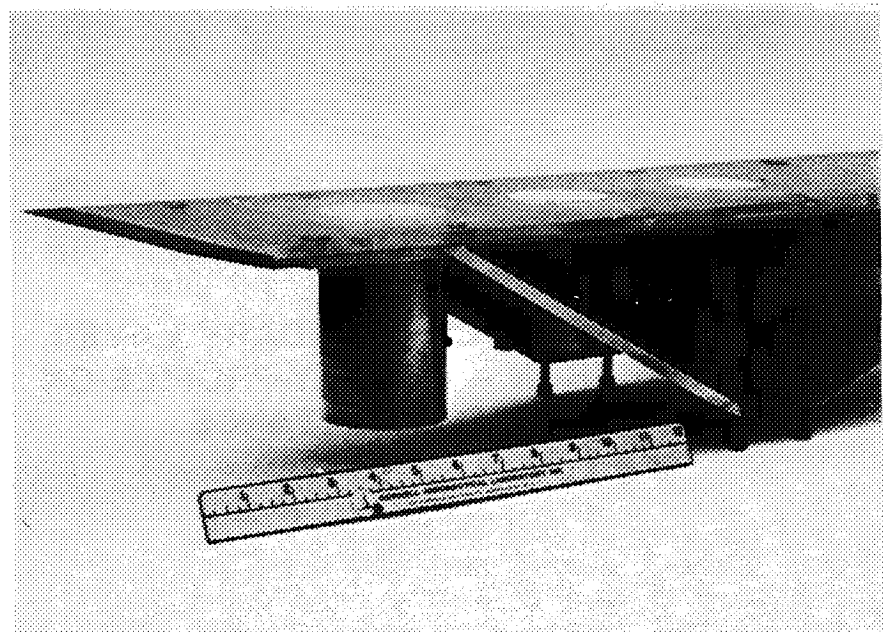


**Figure 19(b) RAM C-III AND RAM C-II ANTENNAS  
IN FLAT-PLATE MODEL**

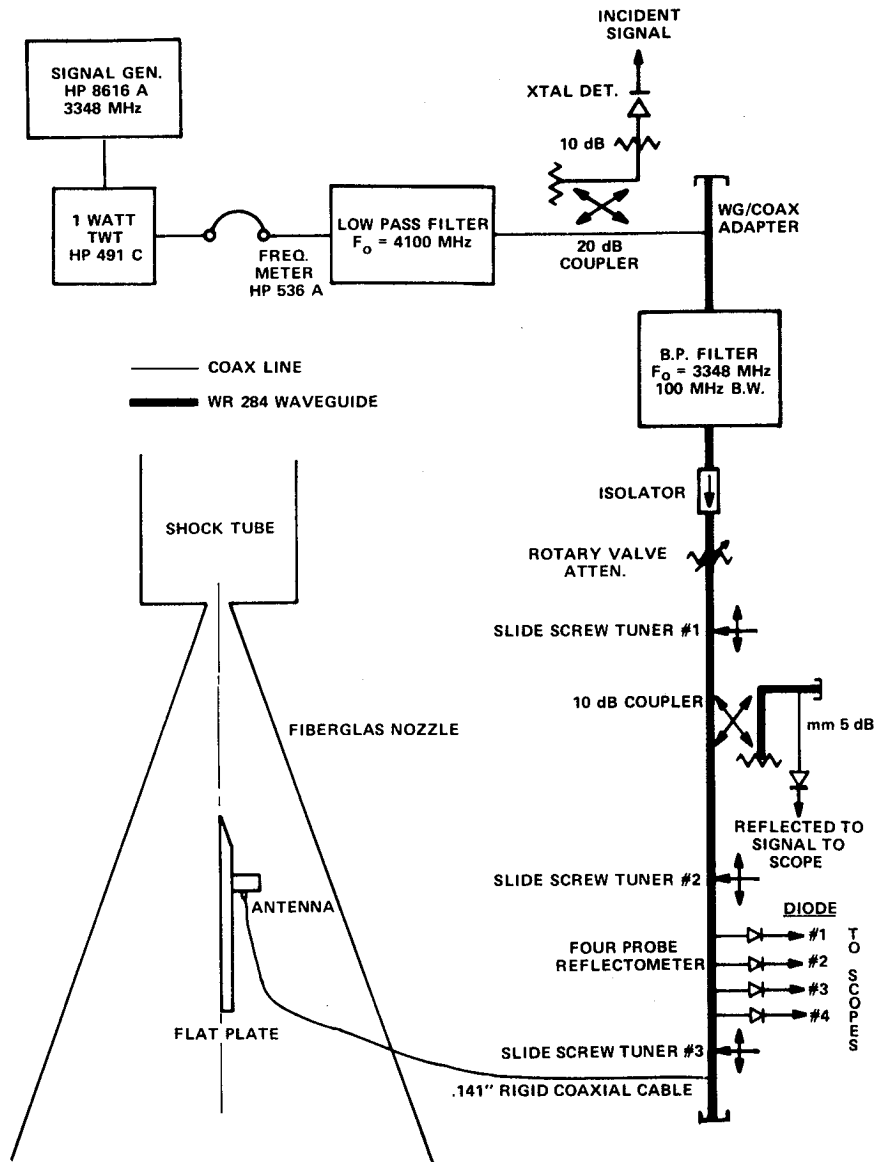


Figure 20 SCHEMATIC DIAGRAM OF FOUR-PROBE REFLECTOMETER

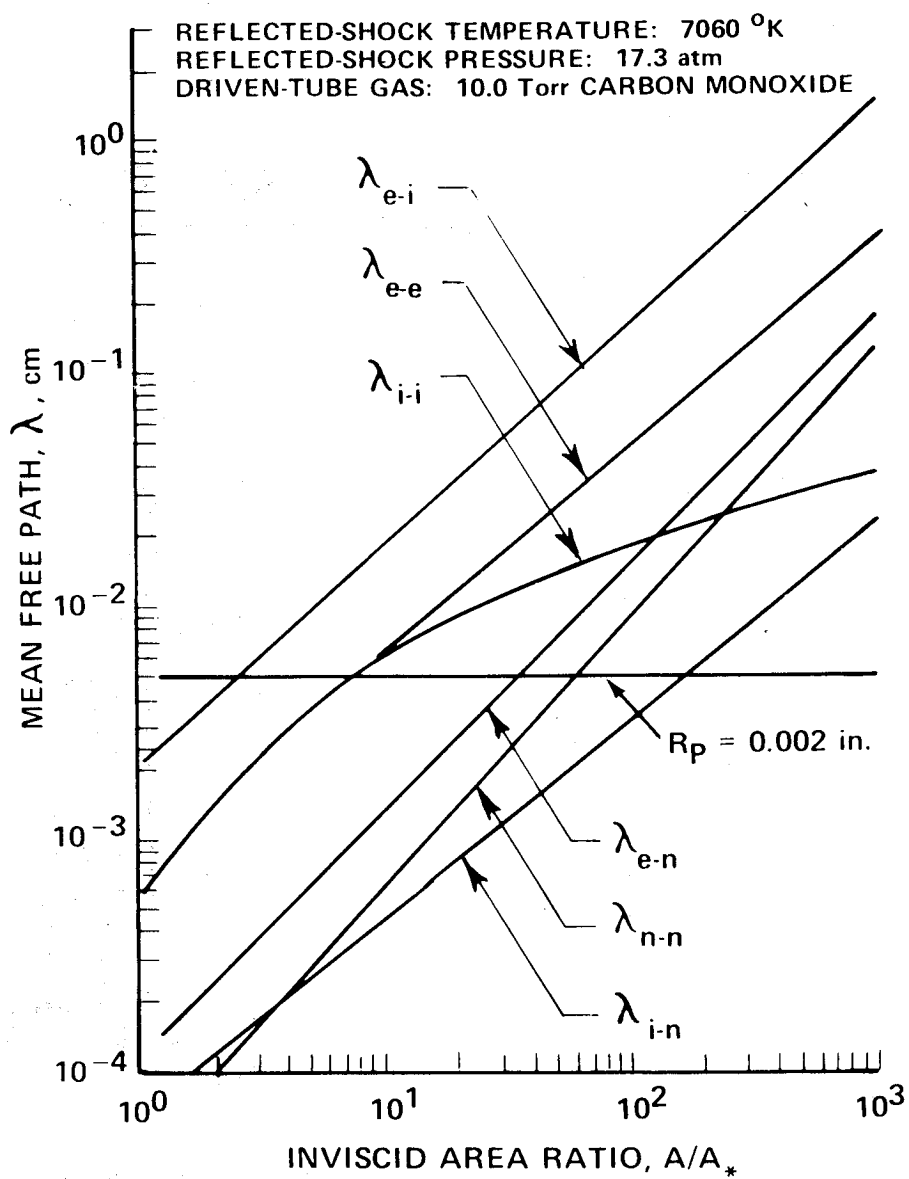
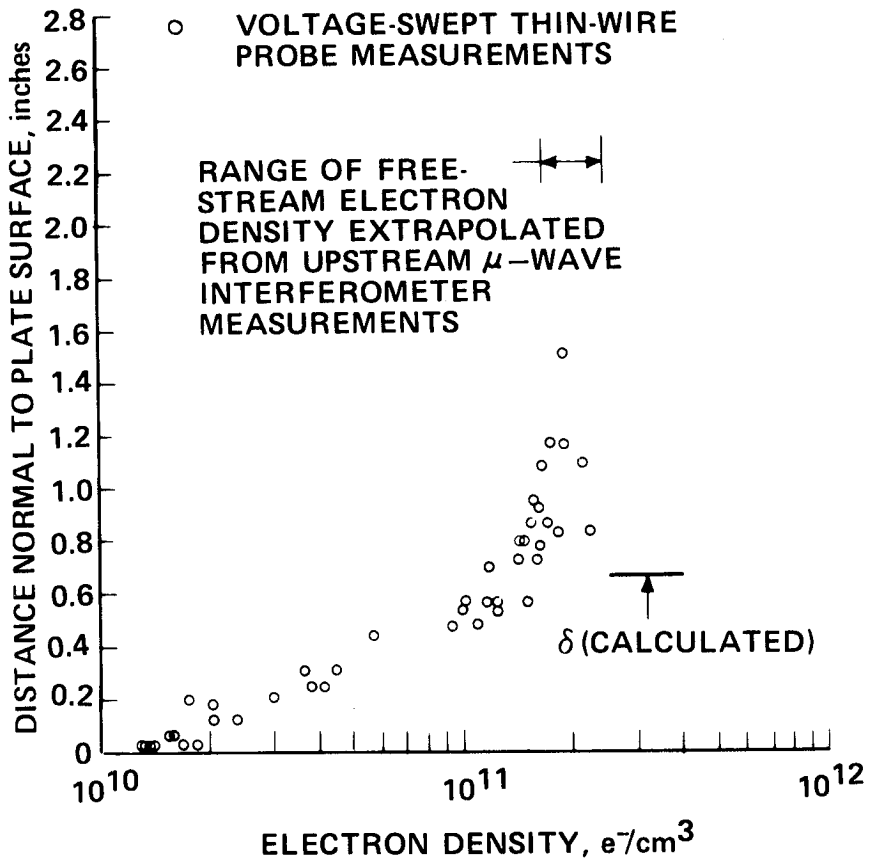
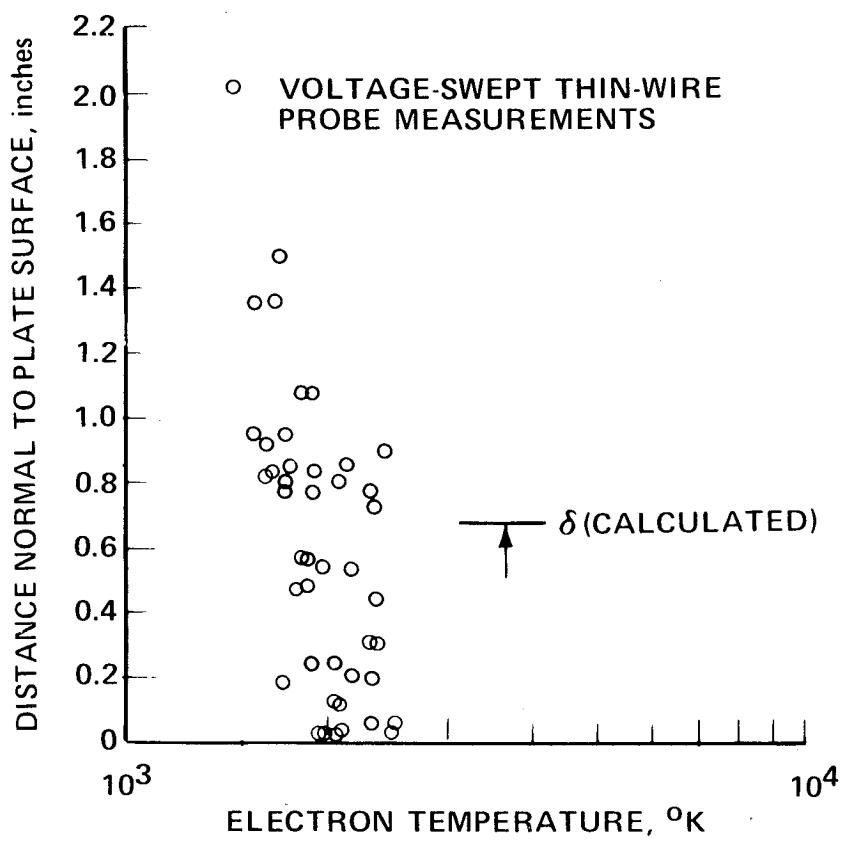


Figure 21 CALCULATED MEAN FREE PATHS IN CARBON MONOXIDE PLASMA



**Figure 22 ELECTRON NUMBER DENSITY ABOVE PLATE AT 6.75-INCHES FROM LEADING EDGE IN CARBON MONOXIDE PLASMA**



**Figure 23 ELECTRON TEMPERATURE ABOVE PLATE AT 6.75-INCHES FROM LEADING EDGE IN CARBON MONOXIDE PLASMA**

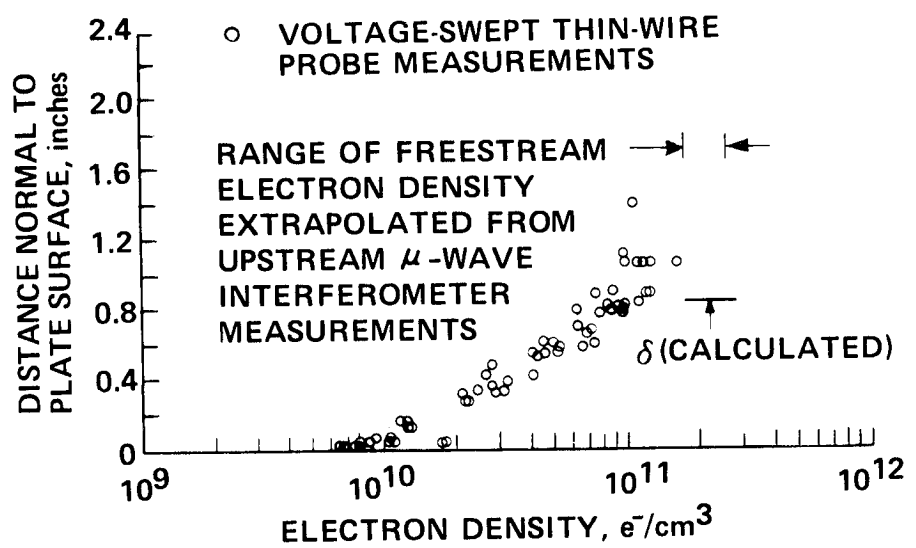


**Figure 24 ELECTRON NUMBER DENSITY ABOVE PLATE AT 11.25 INCHES FROM LEADING EDGE IN CARBON MONOXIDE PLASMA**

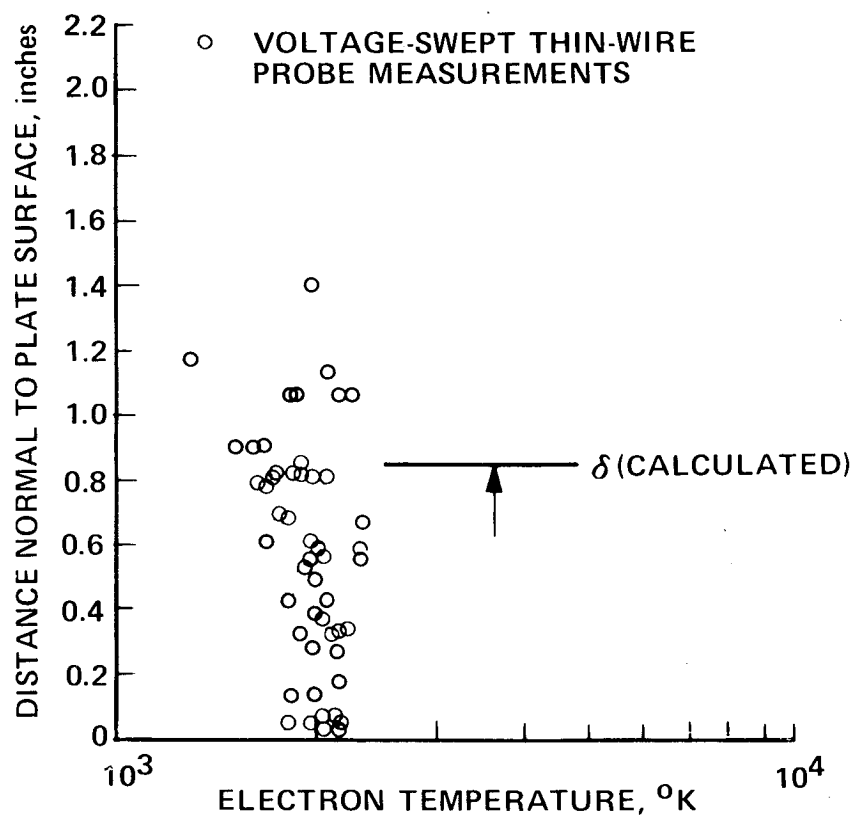
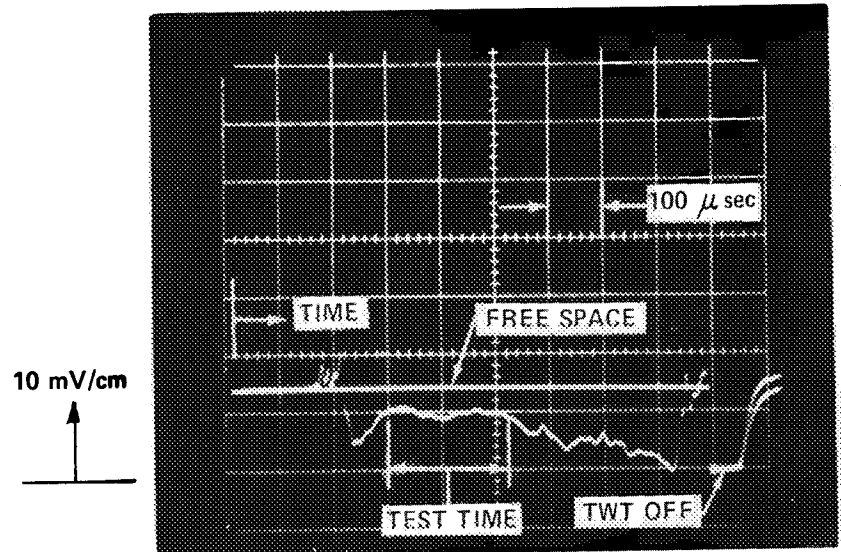
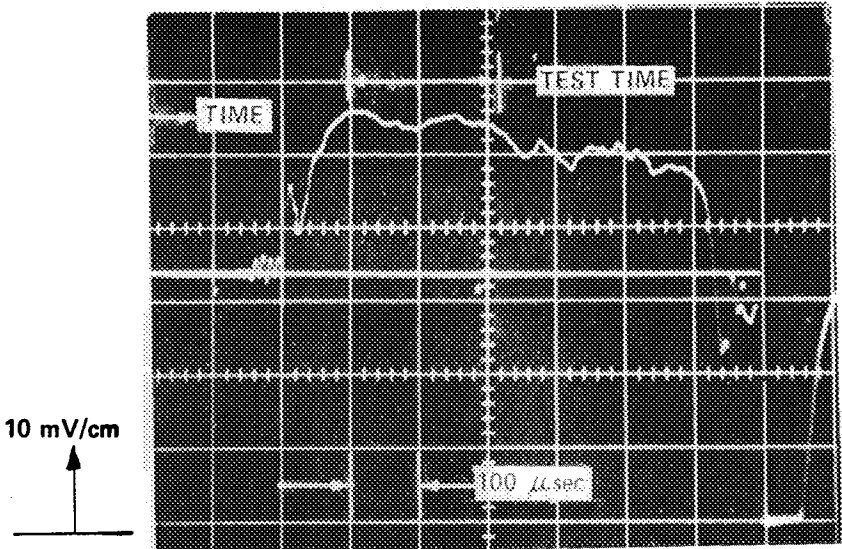


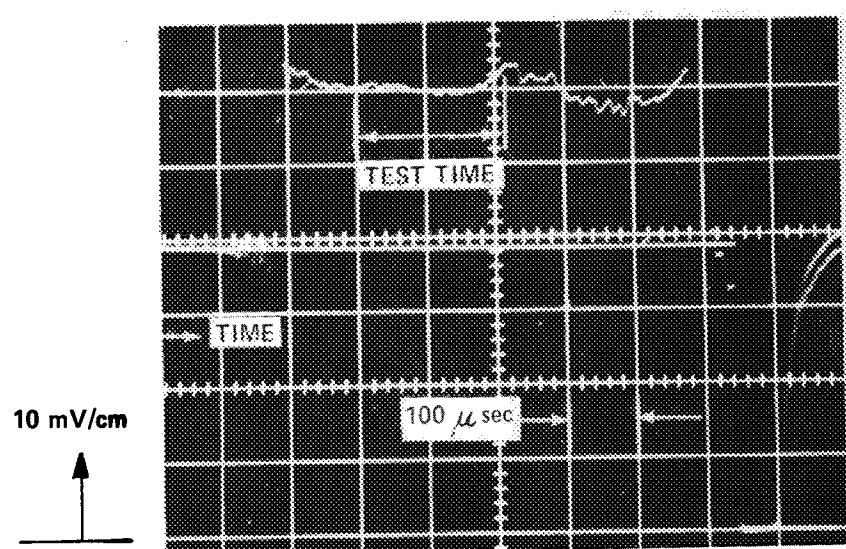
**Figure 25 ELECTRON-TEMPERATURE ABOVE PLATE AT 11.25-INCHES FROM LEADING EDGE IN CARBON MONOXIDE PLASMA**



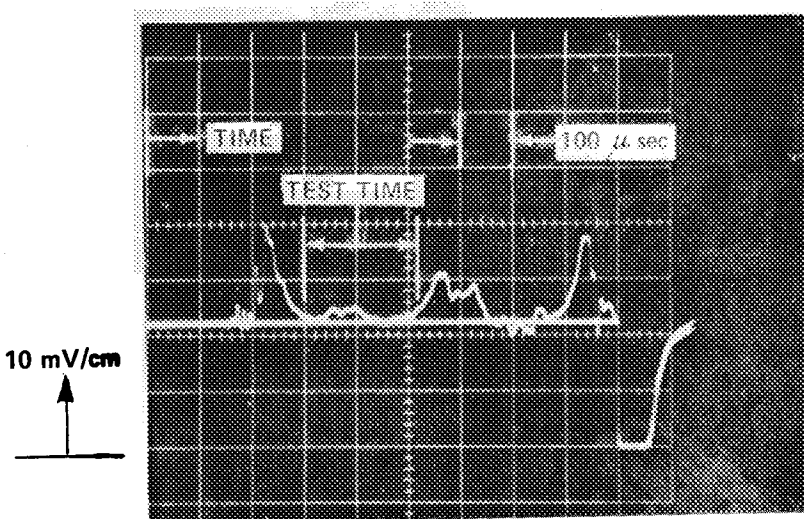
(a) REFLECTOMETER DIODE #1



(b) REFLECTOMETER DIODE #2



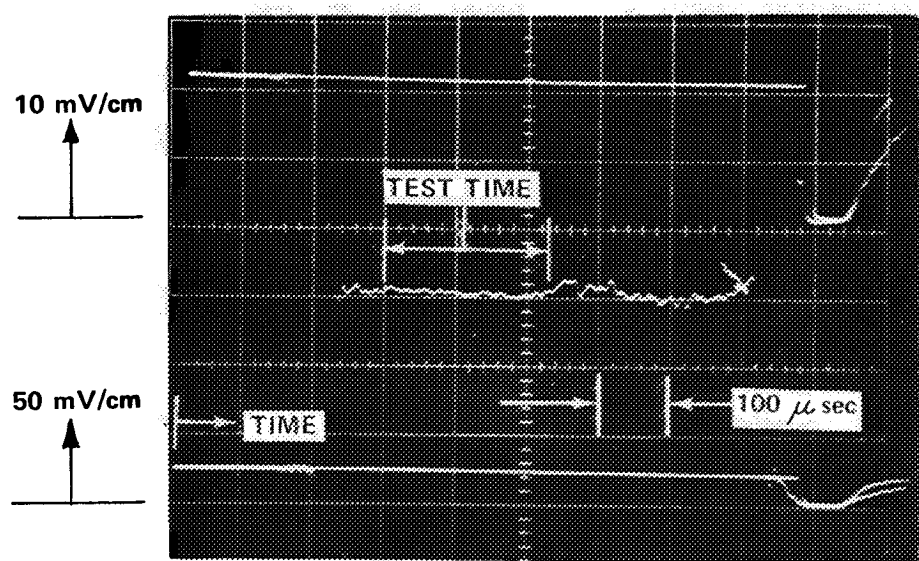
(c) REFLECTOMETER DIODE #3



(d) REFLECTOMETER DIODE #4

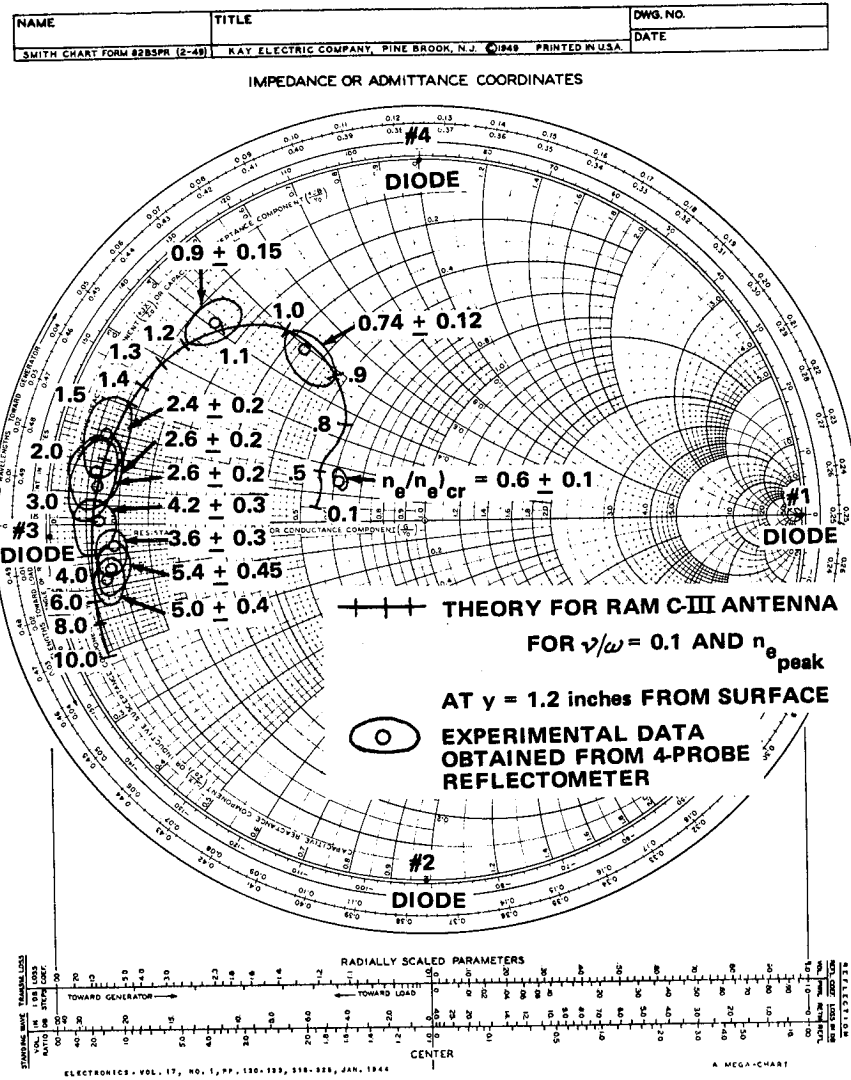
- 1) ANTENNA LOCATED AT 6.75 in. FROM PLATE LEADING EDGE  
 2) PEAK ELECTRON DENSITY OVER ANTENNA DURING TEST TIME WAS  $n_e \approx 7.6 \times 10^{11} e^-/\text{cm}^3$   
 3) RUN NO. 16, TABLE II

Figure 26 TYPICAL REFLECTOMETER AND MICROWAVE-INTERFEROMETER OSCILLOSCOPE RECORDS FOR RAM C-III S-BAND ANTENNA IN CARBON MONOXIDE PLASMA



(e) REFLECTOMETER REFLECTED SIGNAL

Figure 26 TYPICAL REFLECTOMETER AND  
MICROWAVE-INTERFEROMETER  
OSCILLOSCOPE RECORDS FOR  
RAM C-III S-BAND ANTENNA IN  
CARBON MONOXIDE PLASMA (Cont.)



**Figure 27 COMPARISON OF EXPERIMENTAL DATA WITH THEORY FOR RAM C-III ANTENNA AT 6.75 INCHES FROM PLATE LEADING EDGE**

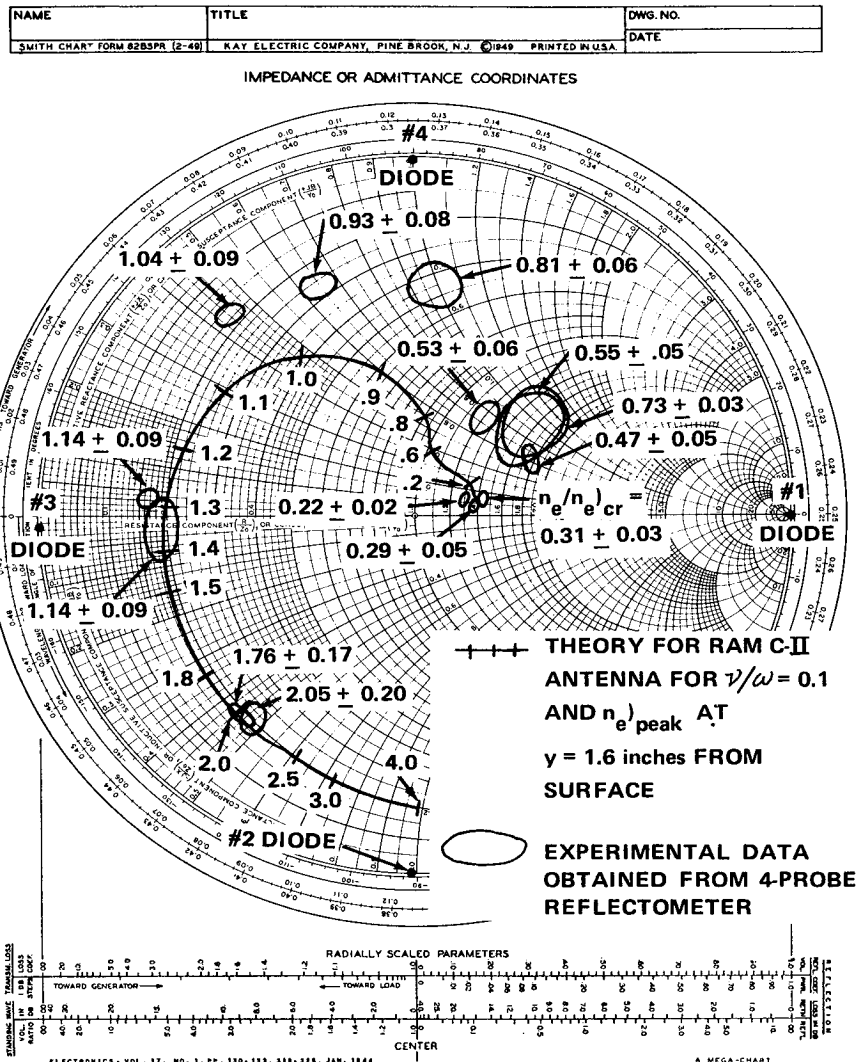


**Figure 28 COMPARISON OF EXPERIMENTAL DATA WITH THEORY FOR RAM C-II ANTENNA AT 11.25 INCHES FROM PLATE LEADING EDGE**

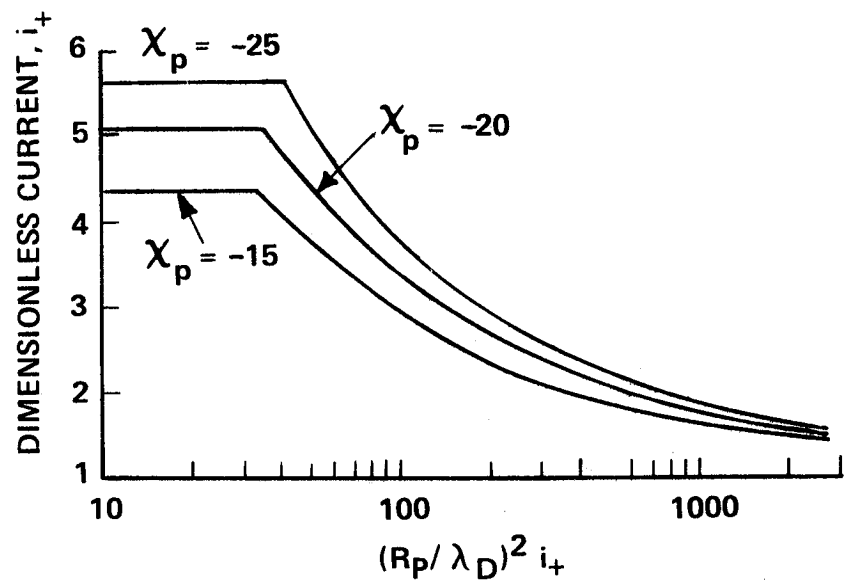


**Figure 29 LAFRAMBOISE THEORETICAL RESULT  
FOR ION CURRENT COLLECTION  
WHEN  $T_i/T_e = 0$**

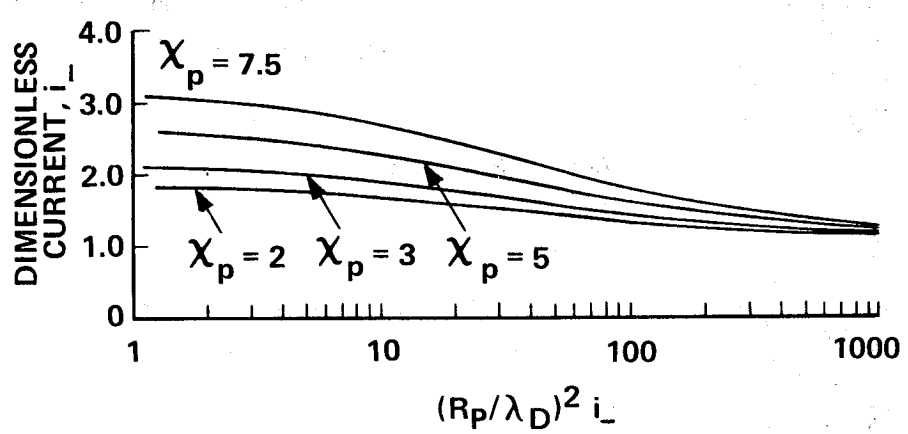


**Figure 30 LAFRAMBOISE THEORETICAL RESULT FOR ELECTRON COLLECTION WHEN  $T_i/T_e = 0$**

○ EXPERIMENTAL DATA  
 LINE FAIRED THROUGH DATA  
 RESERVOIR TEMPERATURE: 7060°K  
 LOCATION: IN BOUNDARY LAYER, 11.25 in. FROM  
 PLATE LEADING EDGE

FOR ELECTRON CURRENT AT  $|X_p| = +5$

FROM LAFRAMBOISE'S THEORY:  
 $i_- = 2.32$

$$\therefore \eta_e = 1.26 \times 10^{10} e^-/\text{cm}^3$$

$$R_p/\lambda_D = 1.78$$

FROM EXPERIMENTAL DATA:  
 $(R_p/\lambda_D)^2 i_- = 7.36$

$$V_\infty \approx +0.50 \text{ volts}$$

FOR ION CURRENT AT  $X_p = -25$

FROM EXPERIMENTAL DATA:

$$(R_p/\lambda_D)^2 i_+ = 16.55$$

$$V_f \approx -0.43 \text{ volts}$$

FROM LAFRAMBOISE'S THEORY:

$$i_+ = 5.64 \therefore \eta_e = 1.17 \times 10^{10} e^-/\text{cm}^3$$

$$R_p/\lambda_D = 1.72$$

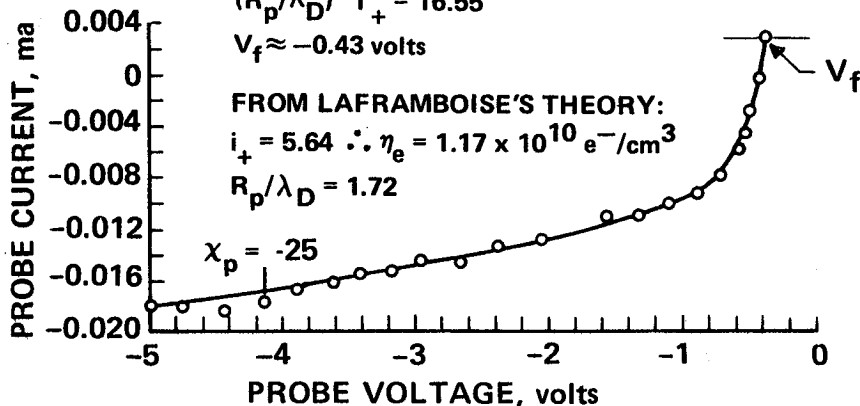
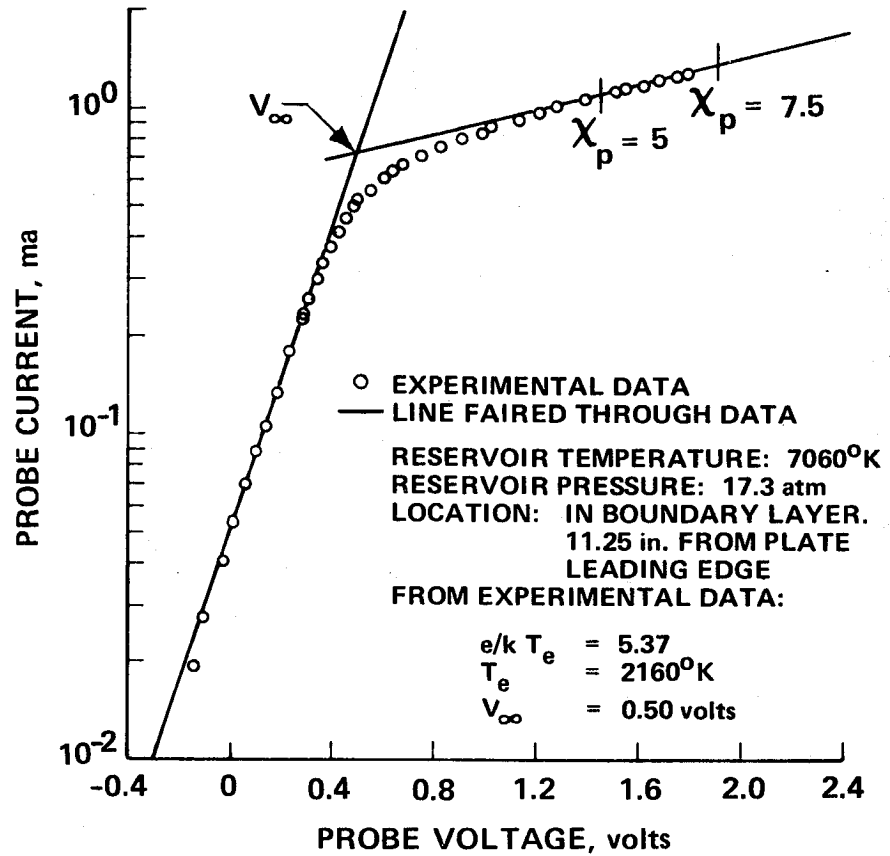


Figure 31 ION-CURRENT REGION OF  
EXPERIMENTAL PROBE  
CHARACTERISTIC IN  
CARBON MONOXIDE



**Figure 32 ELECTRON-RETARDING AND ELECTRON-CURRENT REGIONS OF EXPERIMENTAL PROBE CHARACTERISTICS IN CARBON MONOXIDE**

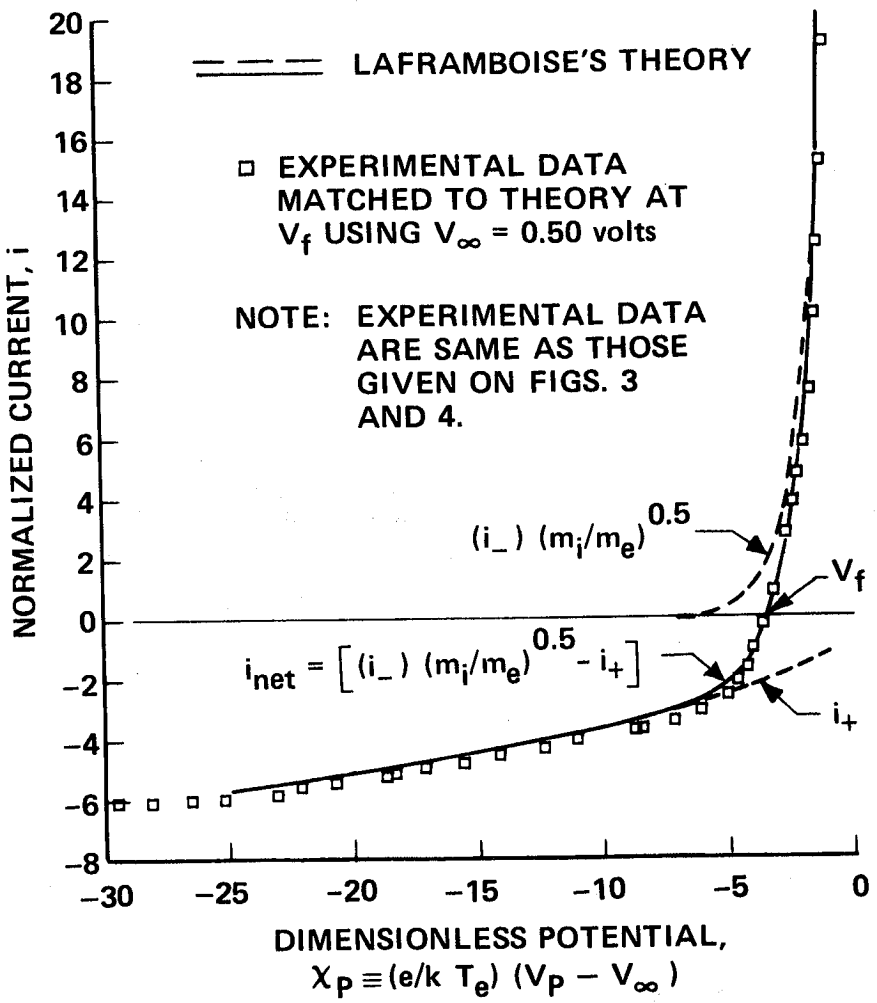
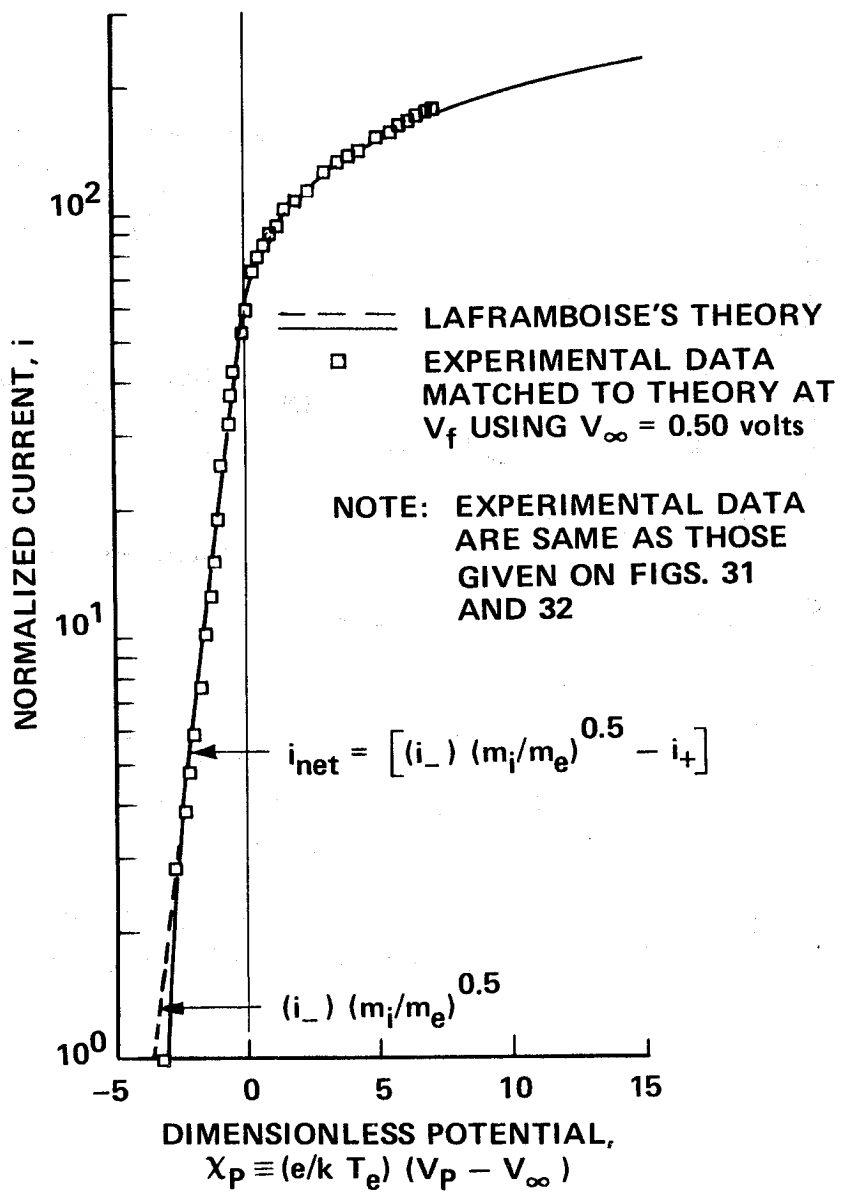


Figure 33 COMPARISON OF ION-CURRENT AND ELECTRON-RETARDING REGIONS WITH LAFRAMBOISE'S THEORY



**Figure 34 COMPARISON OF ELECTRON-RETARDING AND ELECTRON-CURRENT REGIONS WITH LAFRAMBOISE'S THEORY**

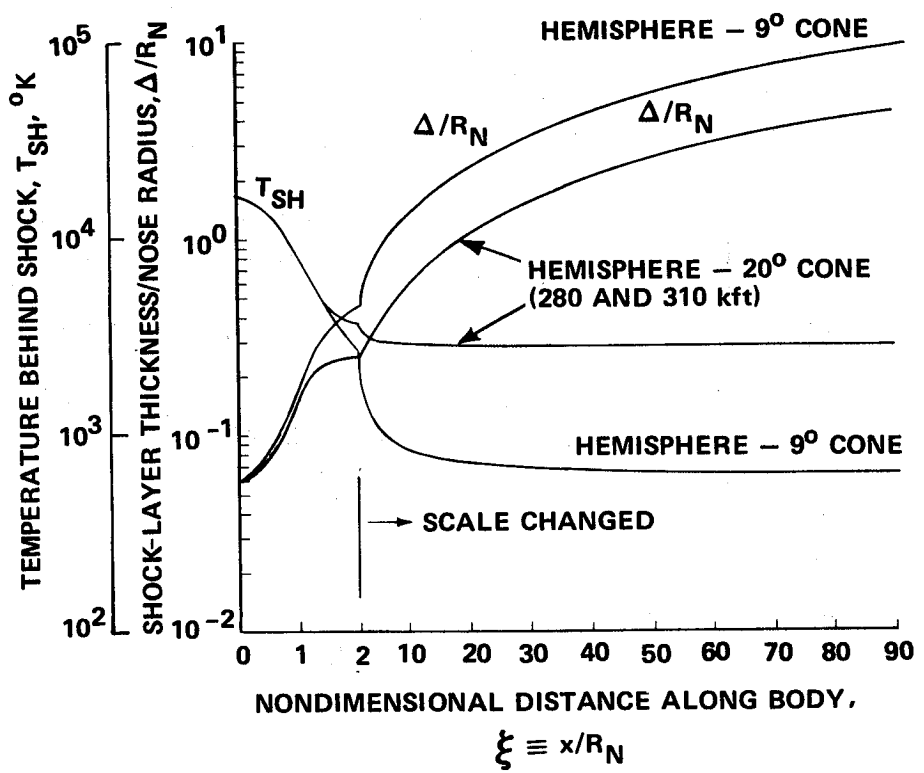


Figure 35 TEMPERATURE BEHIND SHOCK  
AND SHOCK-LAYER THICKNESS

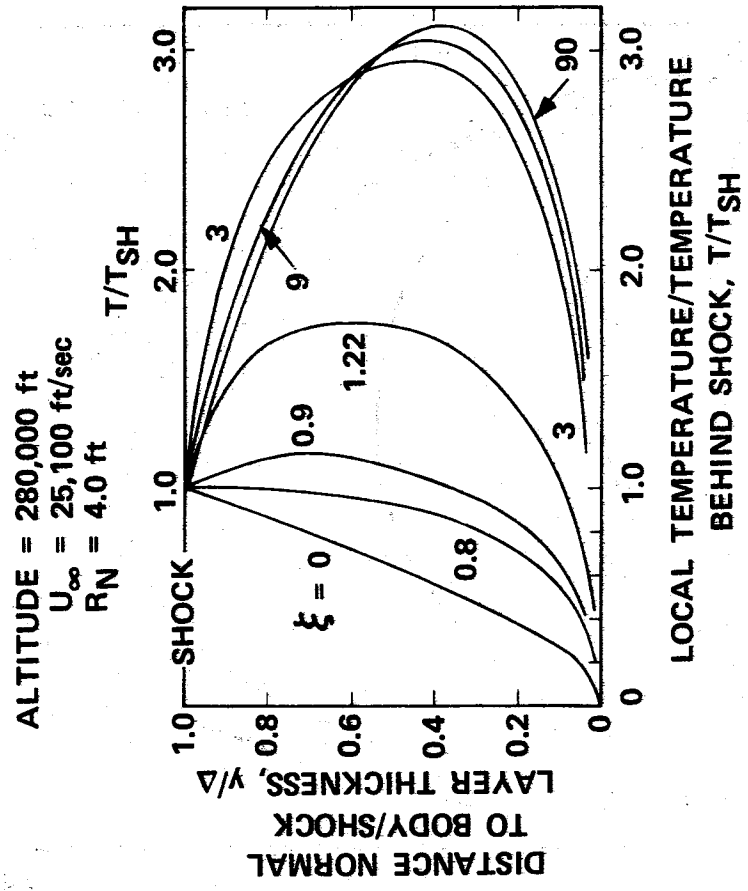


Figure 36 TEMPERATURE PROFILE FOR HEMISPHERE -  $20^{\circ}$  CONE

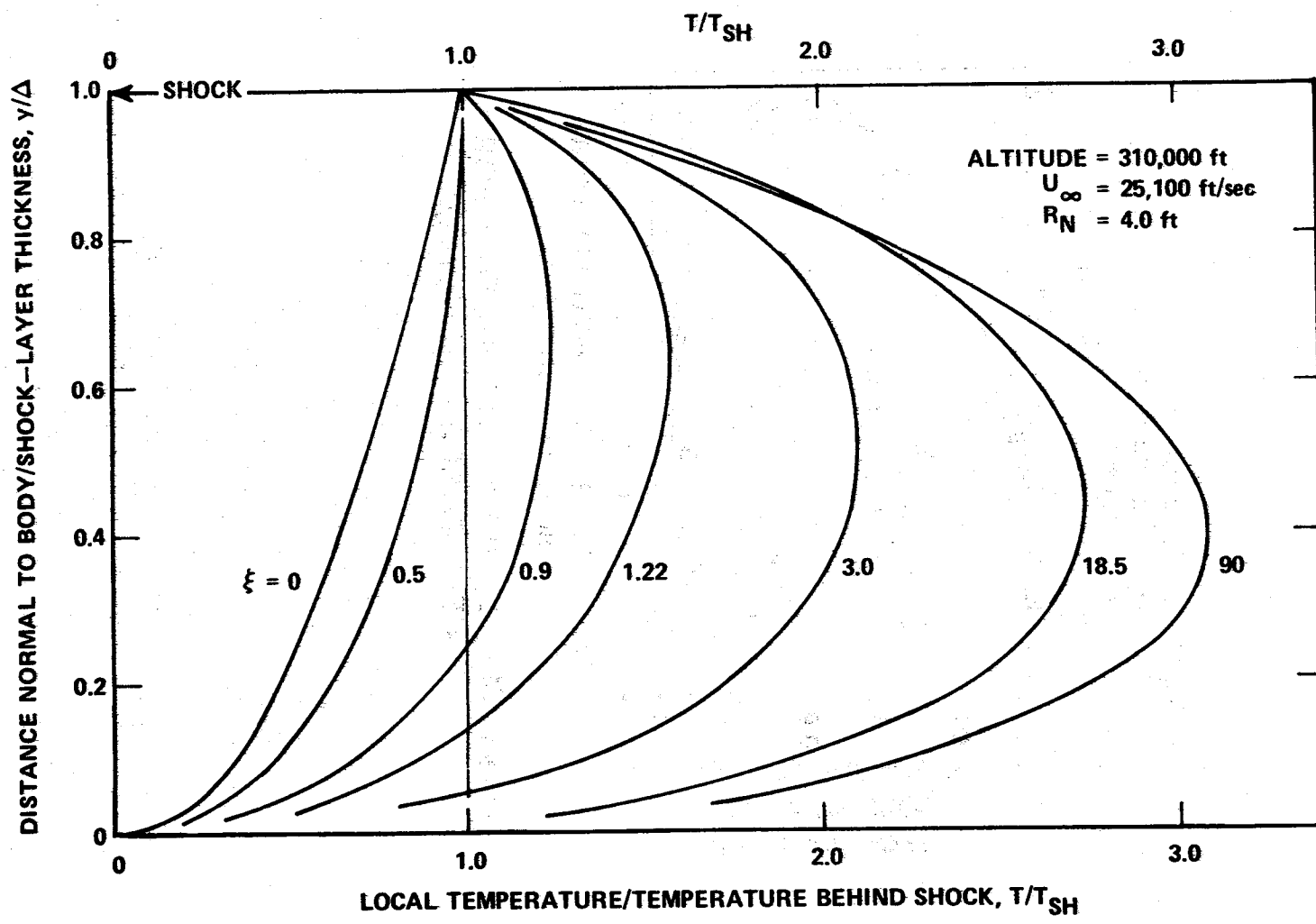
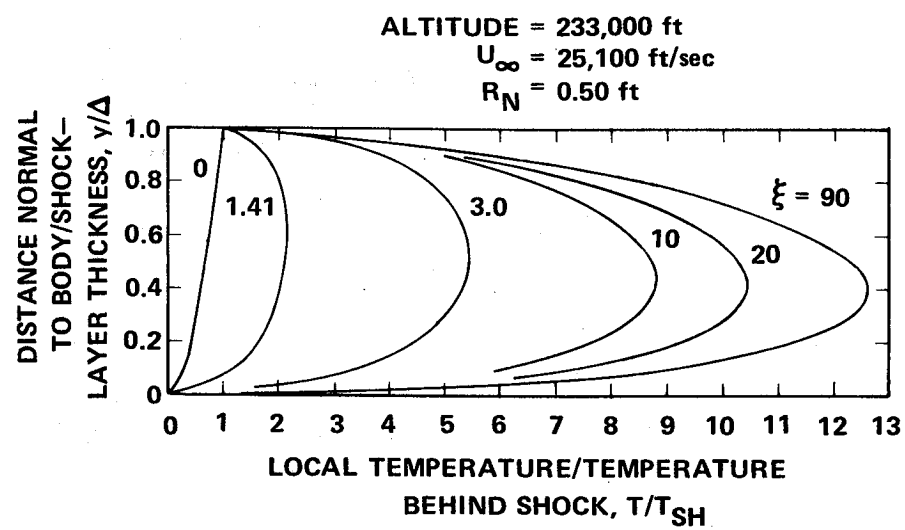
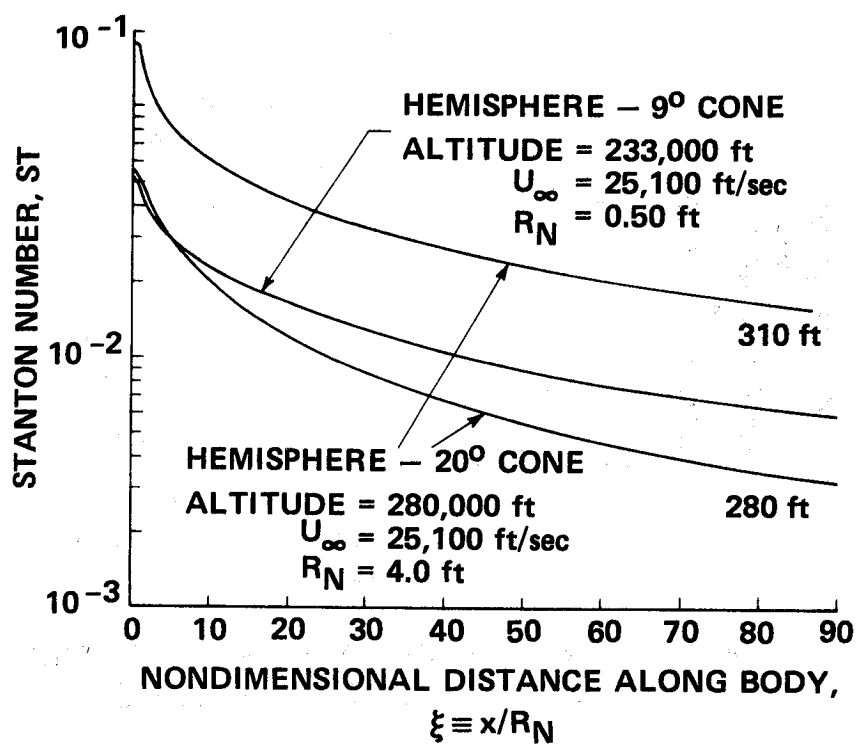


Figure 37 TEMPERATURE PROFILE FOR HEMISPHERE -20° CONE



**Figure 38 TEMPERATURE PROFILE FOR HEMISPHERE — 9° CONE**



**Figure 39 STANTON-NUMBER DISTRIBUTION FOR HEMISPHERE-CONE BODY**

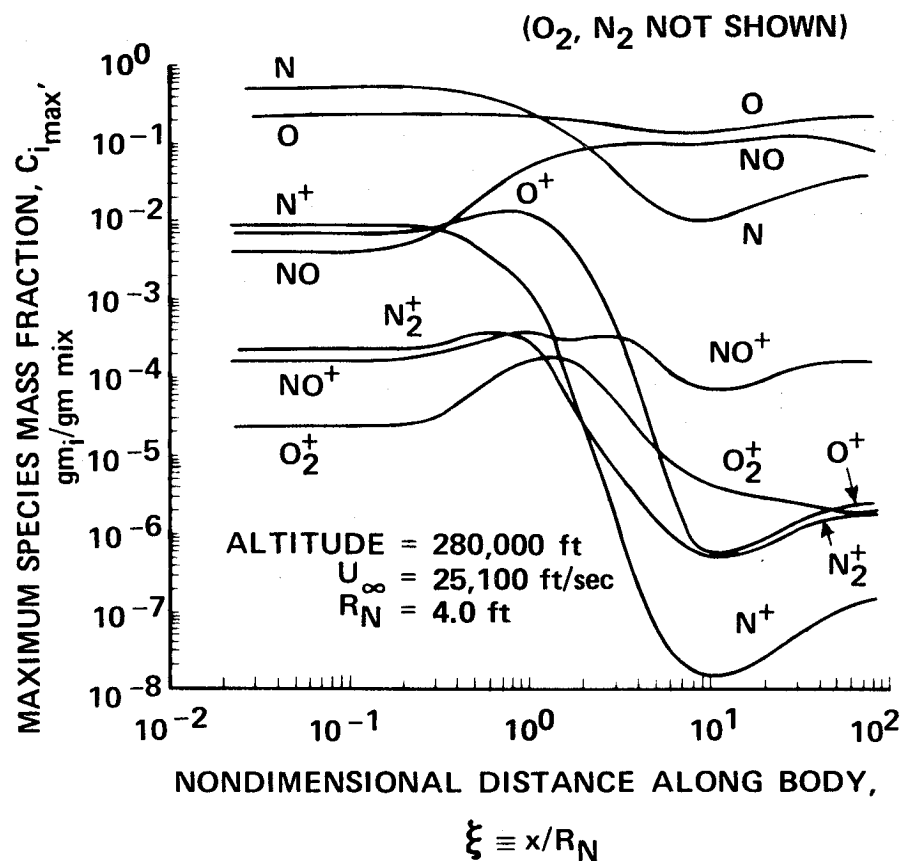


**Figure 40** NONEQUILIBRIUM FLOW SPECIES DISTRIBUTION FOR HEMISPHERE - 20° CONE

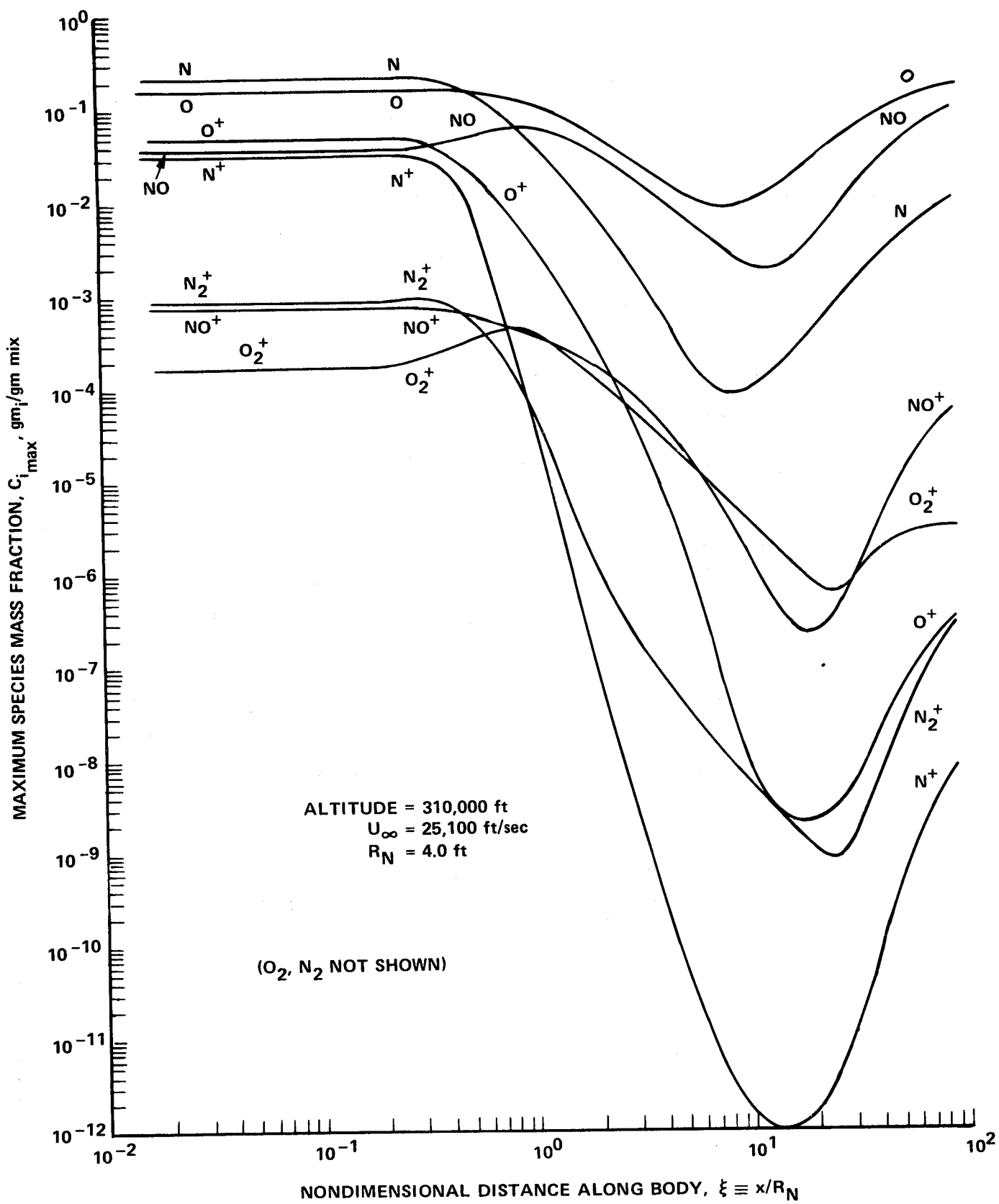
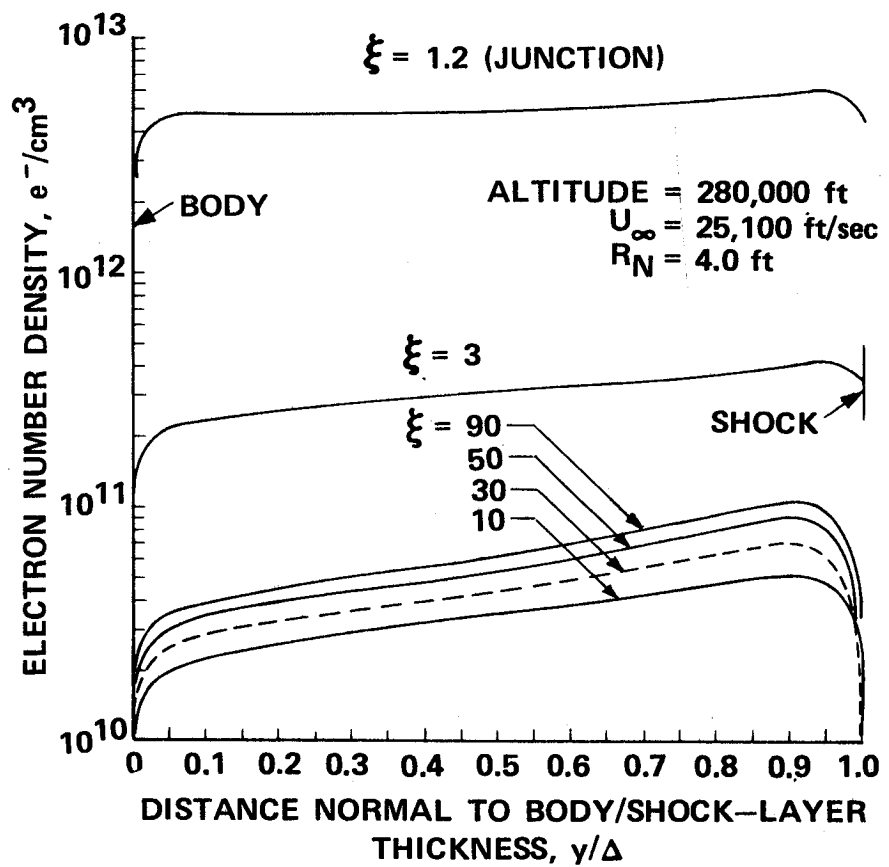


Figure 41 NONEQUILIBRIUM FLOW SPECIES DISTRIBUTION FOR HEMISPHERE – 20° CONE



**Figure 42 ELECTRON NUMBER DENSITY DISTRIBUTION IN SHOCK-LAYER FOR HEMISPHERE - 20° CONE**

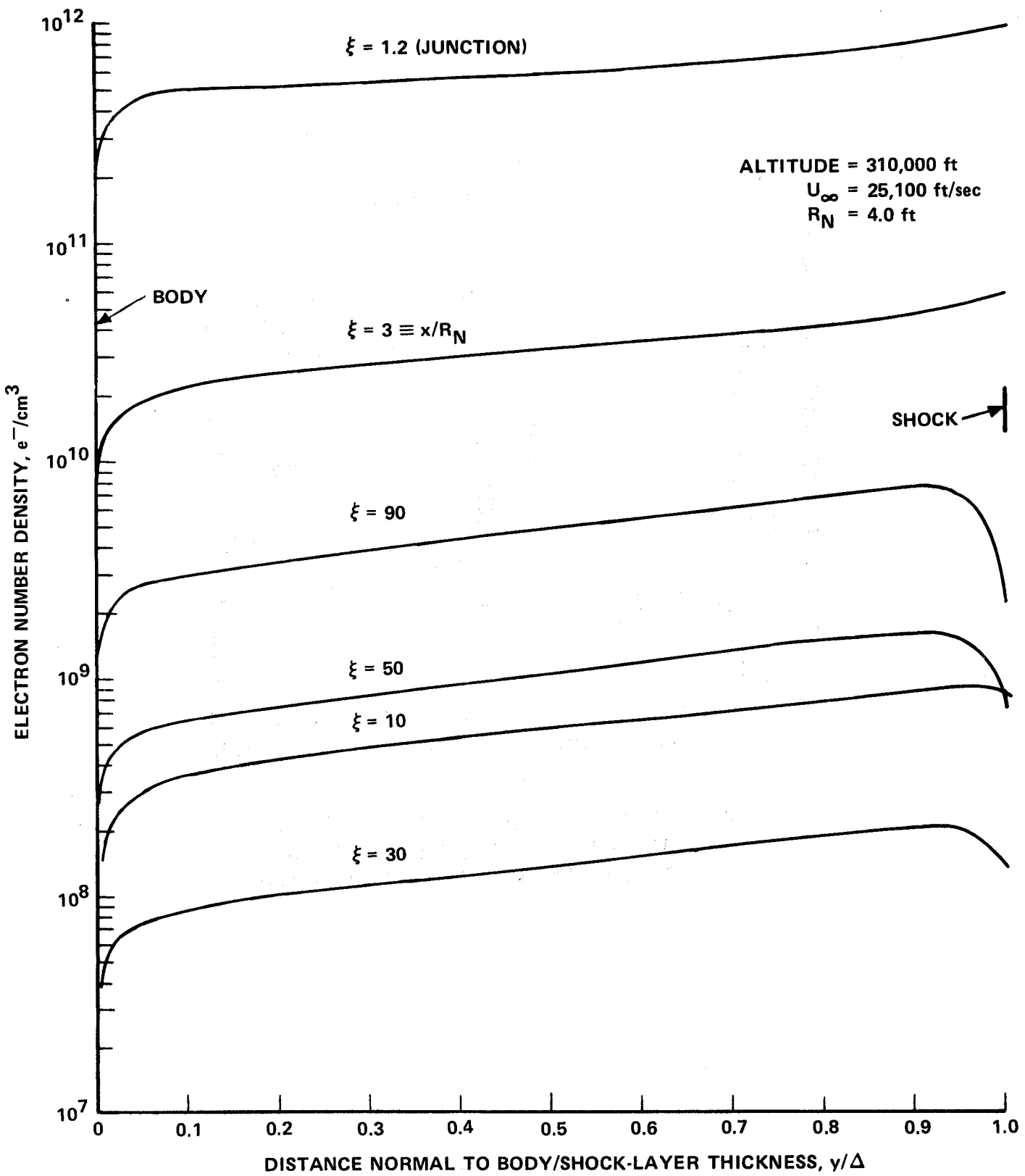


Figure 43 ELECTRON NUMBER-DENSITY DISTRIBUTION IN SHOCK LAYER FOR HEMISPHERE -  $20^\circ$  CONE

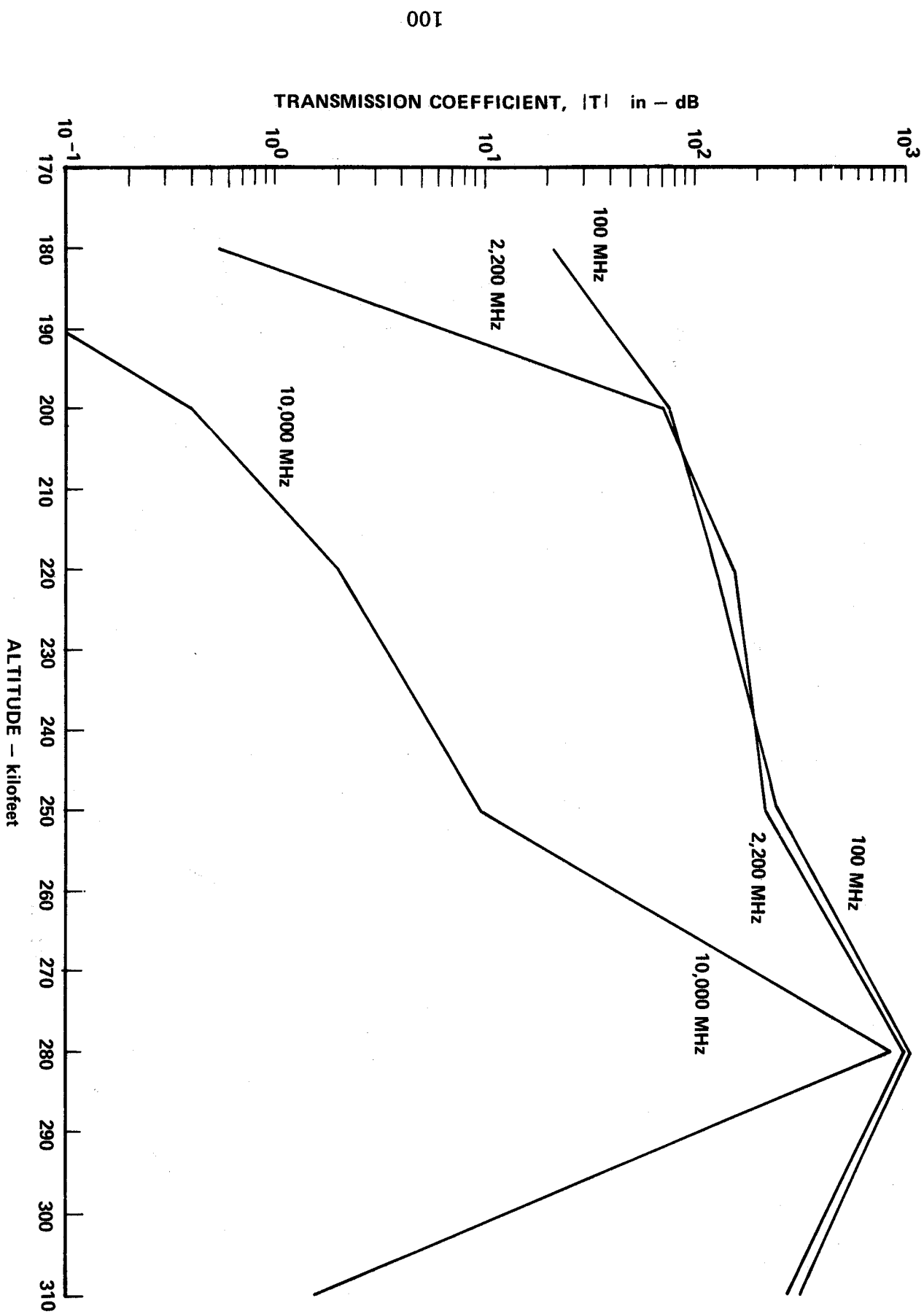


Figure 44 PLANE-WAVE TRANSMISSION COEFFICIENT AT  $\xi = 1.22$

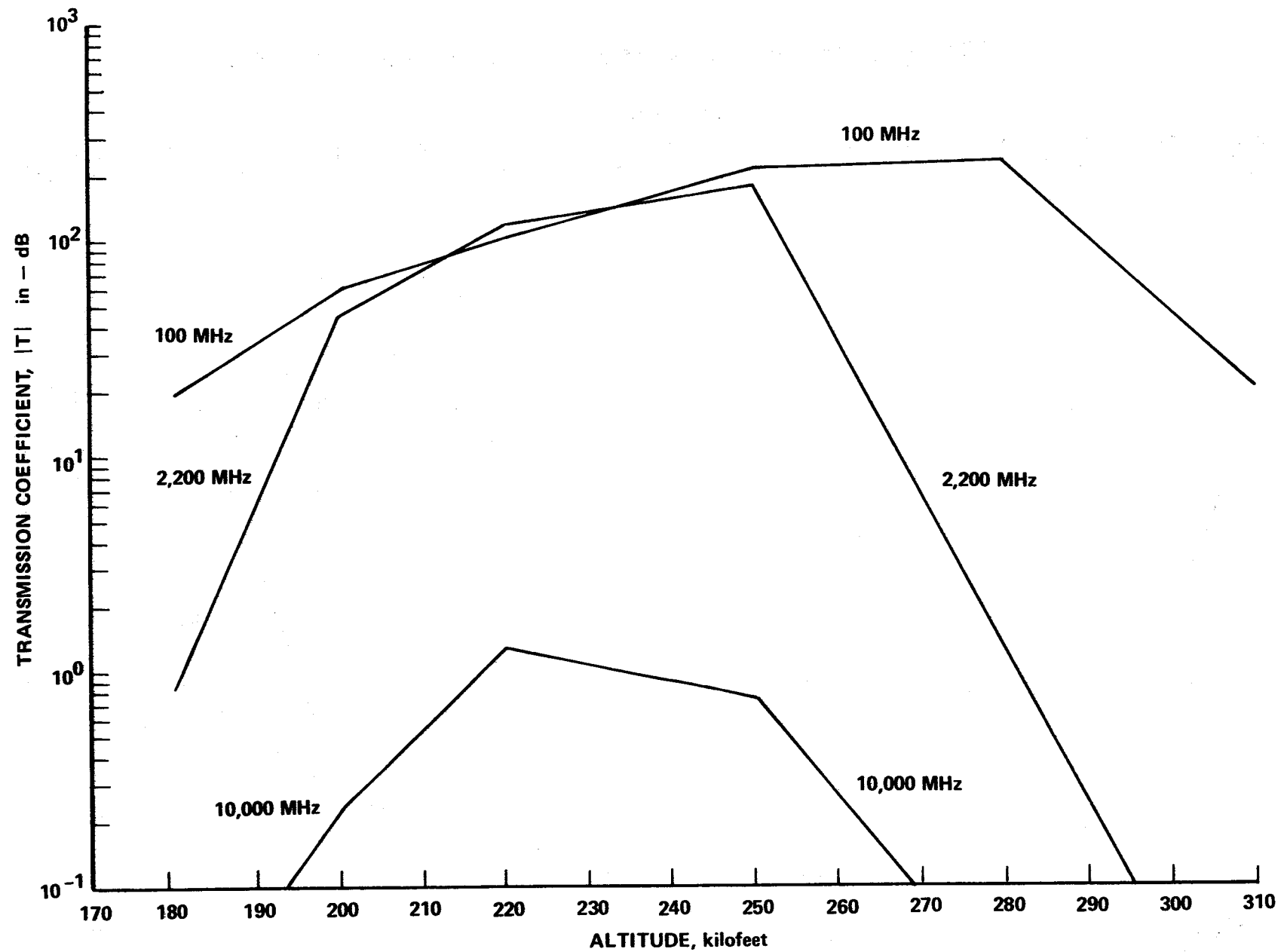


Figure 45 PLANE-WAVE TRANSMISSION COEFFICIENT AT  $\xi = 10$

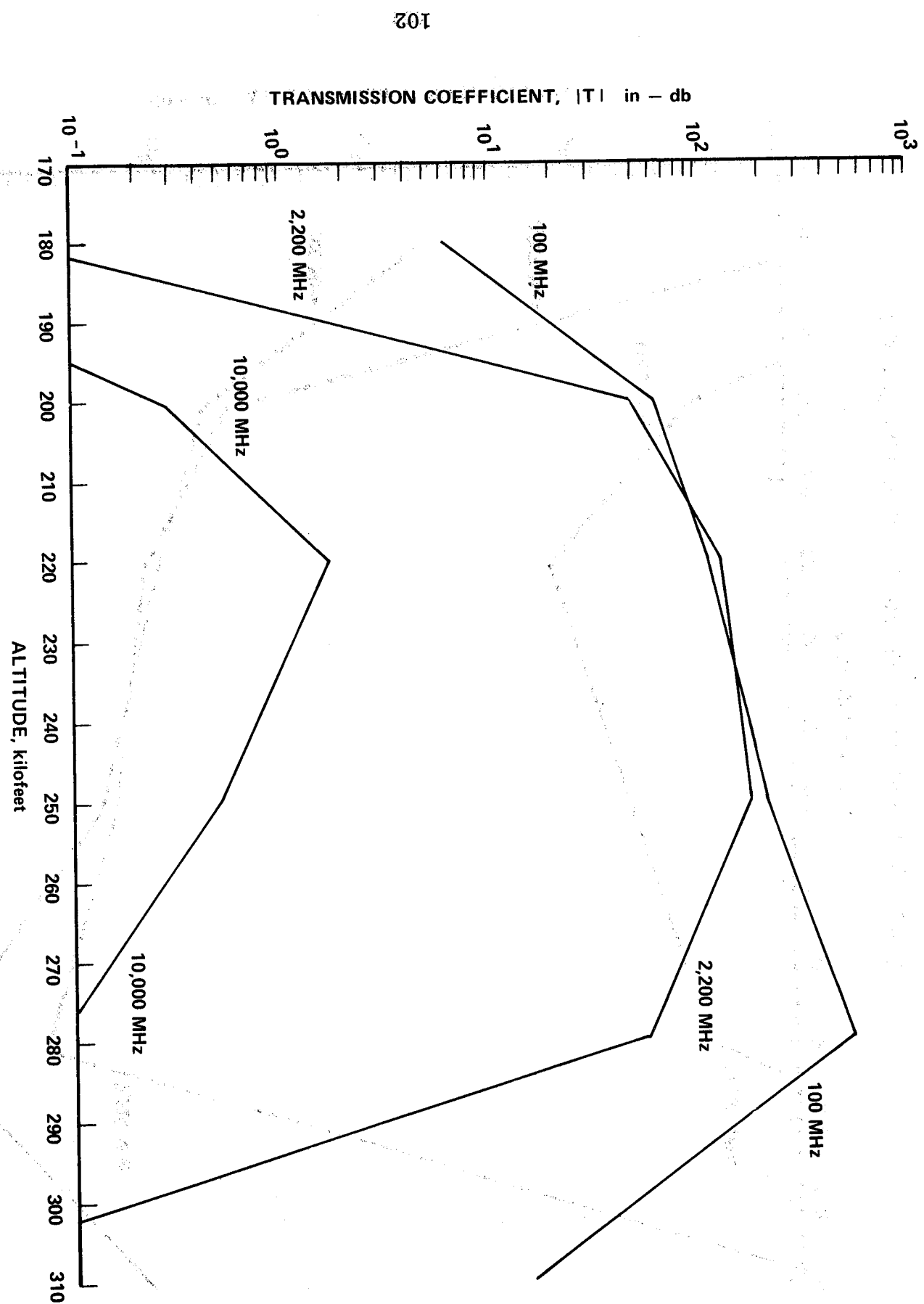


Figure 46 PLANE-WAVE TRANSMISSION COEFFICIENT AT  $\xi = 30^\circ$

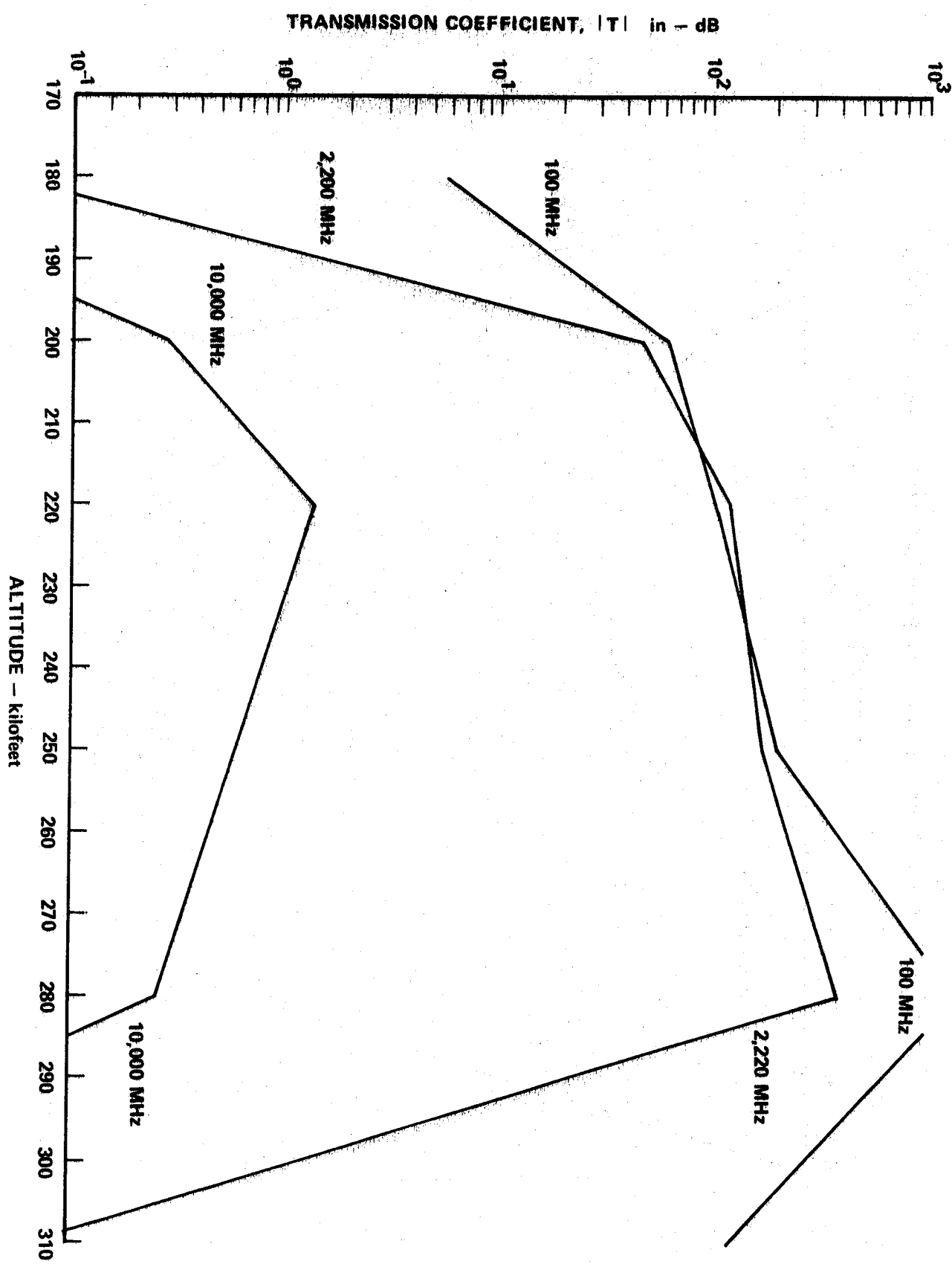


Figure 47 PLANE-WAVE TRANSMISSION COEFFICIENT AT  $\xi = 50$

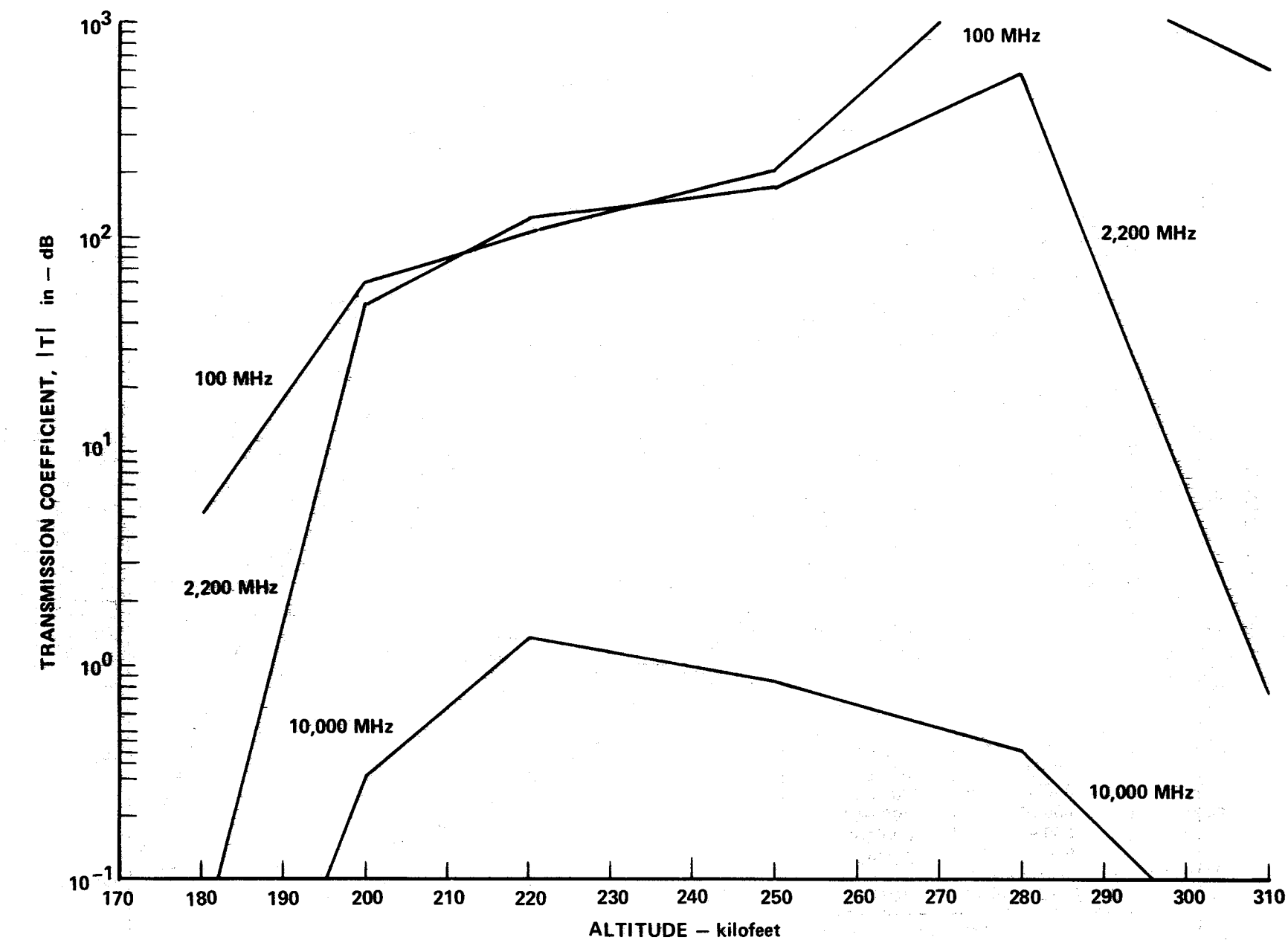


Figure 48 PLANE-WAVE TRANSMISSION COEFFICIENT AT  $\xi = 90$

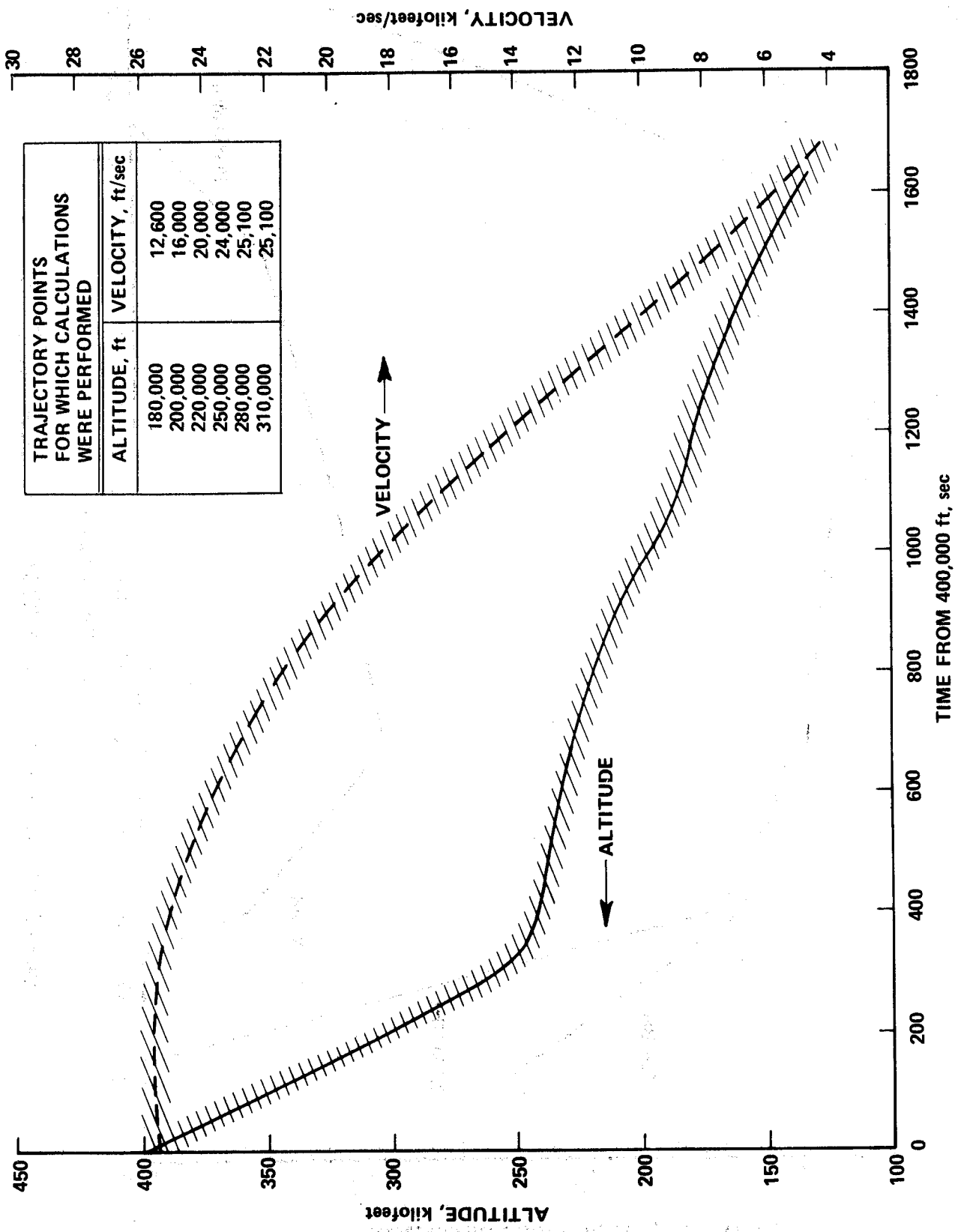
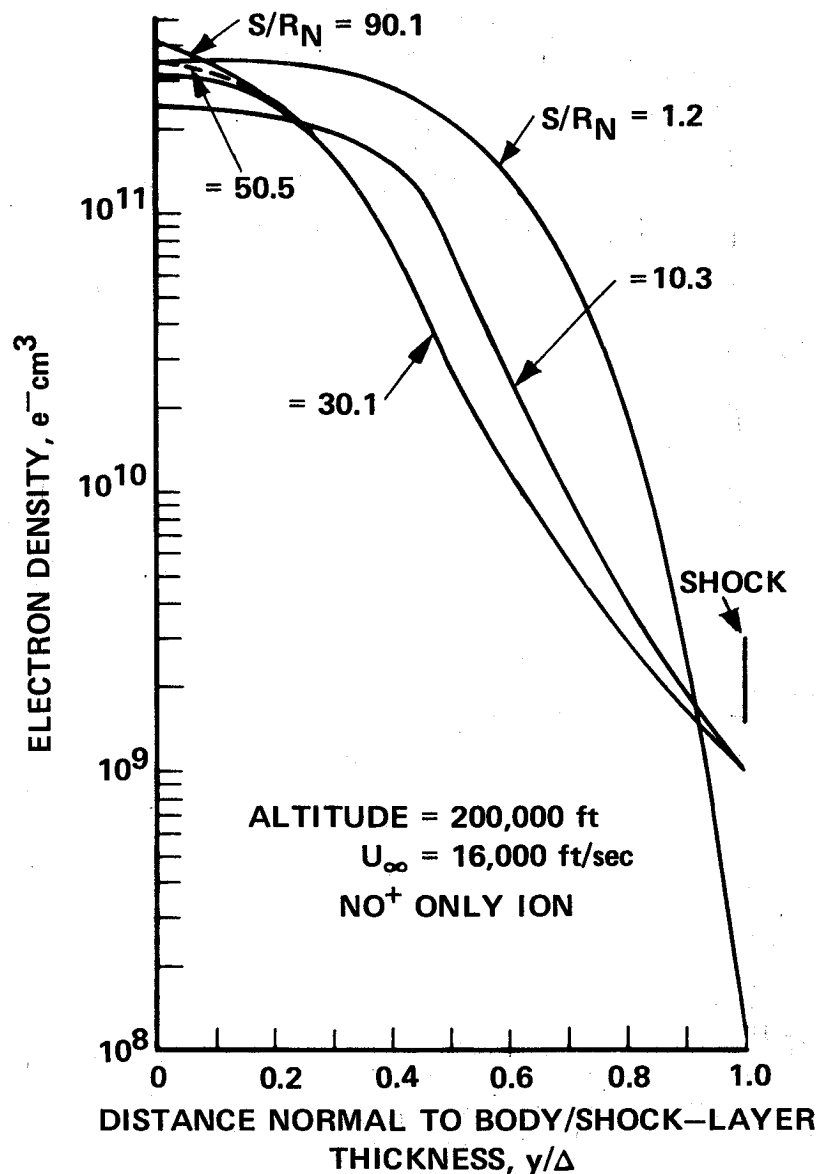
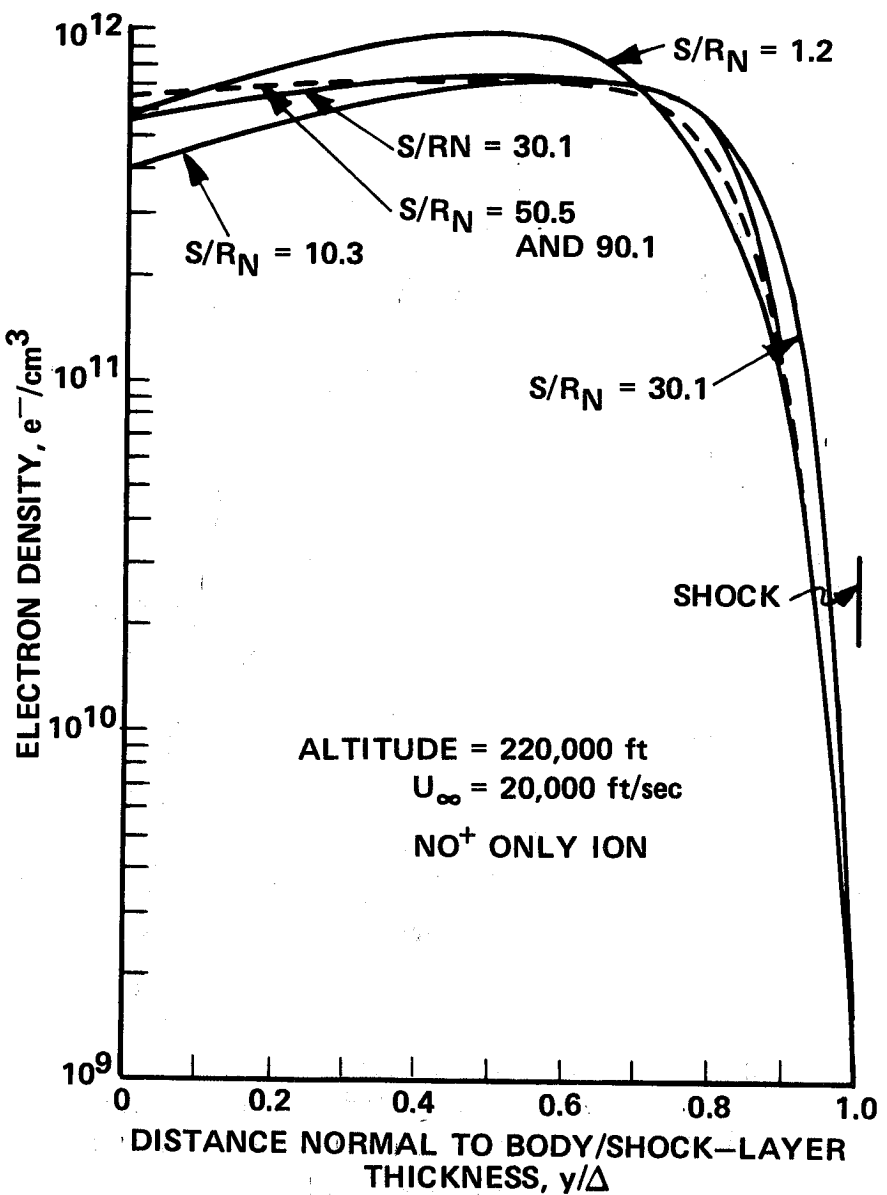


Figure 49 TYPICAL SHUTTLE ENTRY TRAJECTORY



**Figure 50 ELECTRON NUMBER-DENSITY  
DISTRIBUTION IN SHOCK-LAYER  
FOR BLUNTED DELTA AT  $\alpha = 20^\circ$**



**Figure 51. ELECTRON NUMBER-DENSITY  
 DISTRIBUTION IN SHOCK-LAYER  
 FOR BLUNTED DELTA AT  $\alpha = 20^\circ$**

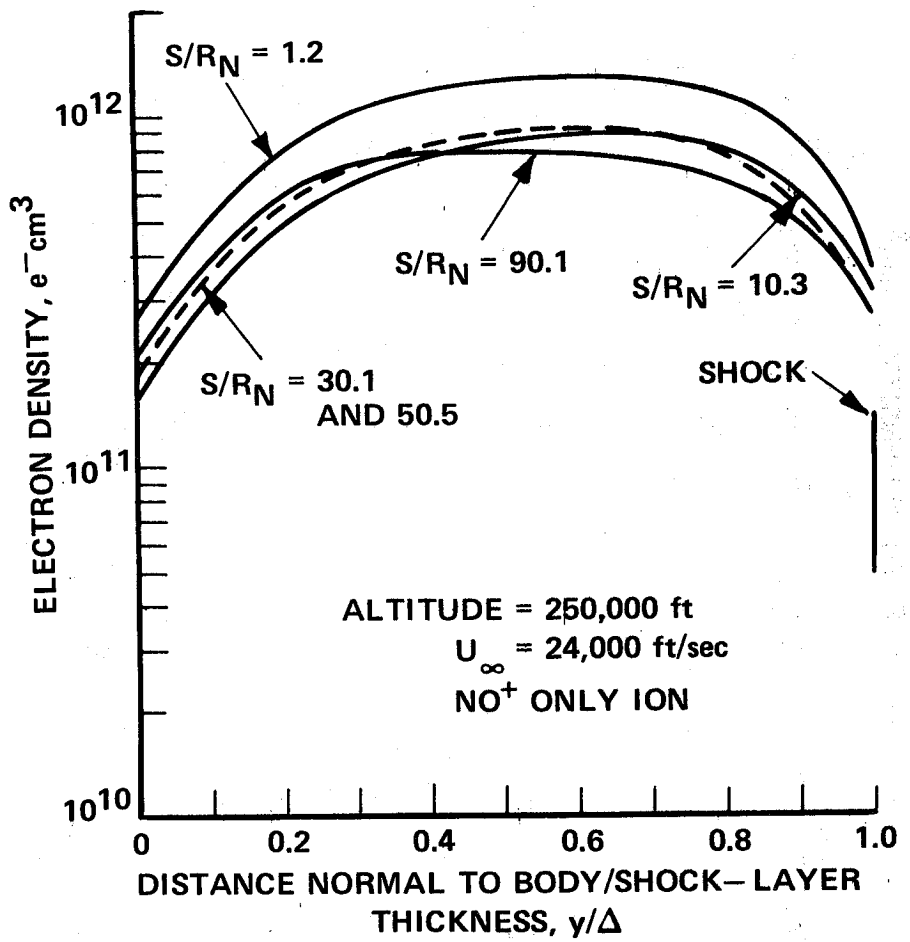
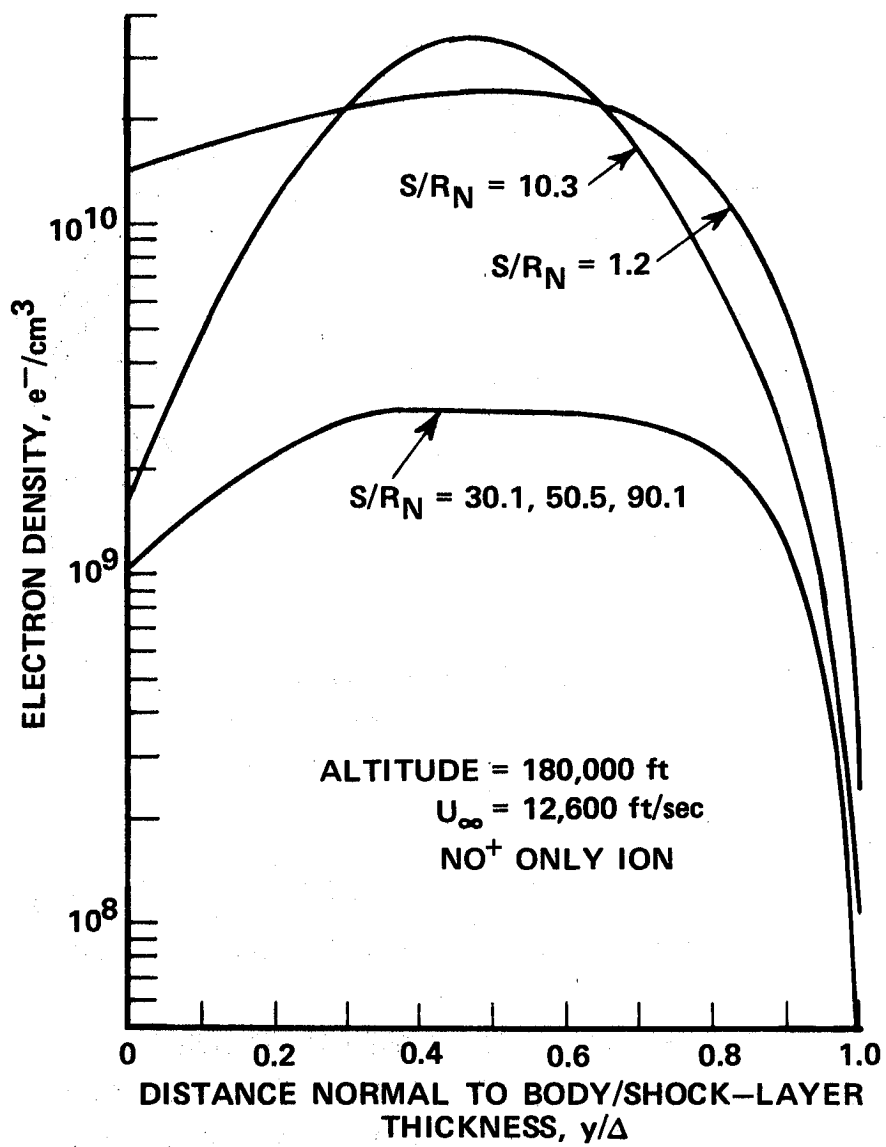


Figure 52 ELECTRON NUMBER-DENSITY DISTRIBUTION IN SHOCK-LAYER FOR BLUNTED DELTA AT  $\alpha = 20^\circ$



**Figure 53 ELECTRON NUMBER–DENSITY  
 DISTRIBUTION IN SHOCK–LAYER  
 FOR BLUNTED DELTA AT  $\alpha = 20^\circ$**

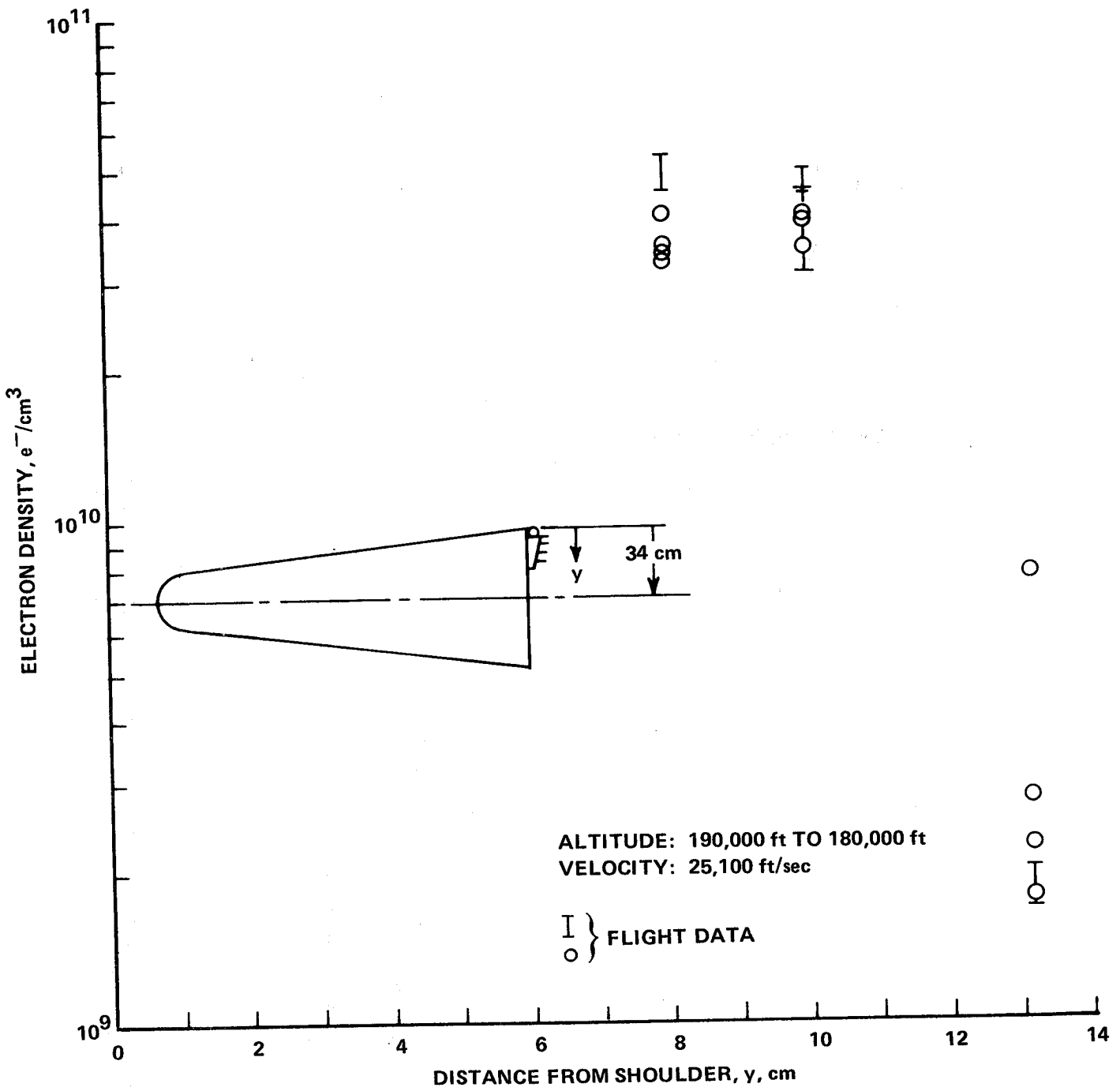


Figure 54 TEMPERATURE IN BASE REGION OF RAM C-III AS DETERMINED FROM SWEPT-VOLTAGE PROBE CHARACTERISTIC

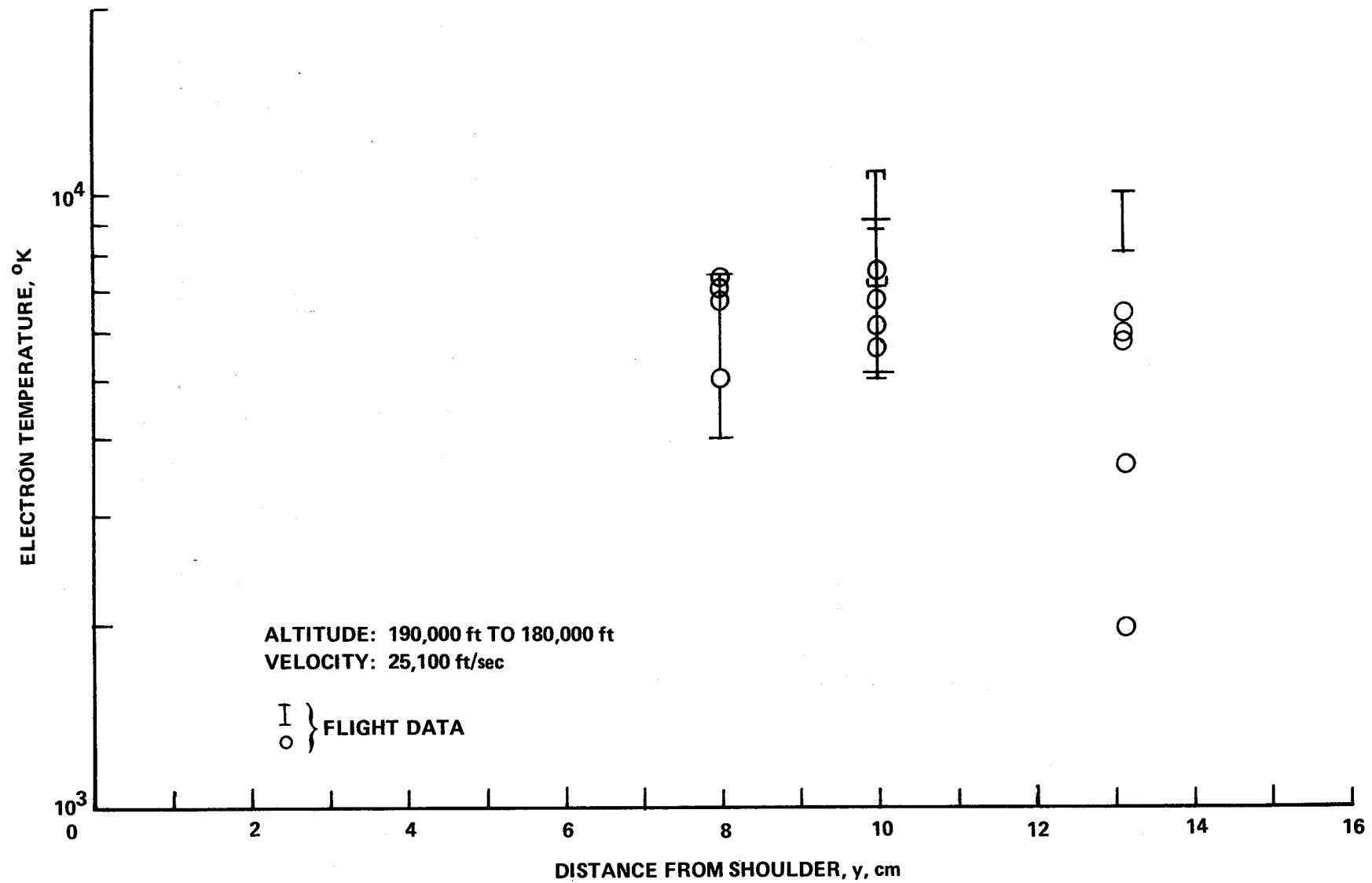


Figure 55 ELECTRON DENSITY IN BASE REGION OF RAM C-III AS DETERMINED FROM ELECTRON CURRENT REGION OF SWEEP-VOLTAGE PROBE CHARACTERISTIC

